Faculdade de Engenharia da Universidade do Porto

A new bone tissue remodeling algorithm combining mechanical stimuli with cellular dynamics

Madalena Macedo Alves Peyroteo Gomes

Dissertation carried out under the
Integrated Master in Bioengineering
Biomedical Engineering

Supervisor: Professor Jorge Américo Oliveira Pinto Belinha
Co-Supervisor: Professor Renato Manuel Natal Jorge

June 2016

Abstract

For decades, bone has been the subject of study of many researchers, due to its capacity to continually renew itself. Nowadays, understanding the basic biology of bone remodeling has become critical and very relevant. This because, having a very thorough knowledge about the normal functioning of the bone, allows more easily the construction of the bridge that permits to discover and describe the pathogenesis of various disorders of bone remodeling. For instance, these disorders can be renal osteodystrophy, Paget's disease, osteopetrosis, and osteoporosis that affects over 200 million people worldwide [1].

Therefore, this master thesis aims to create a new spatiotemporal model that can replicate the biomechanical and biochemical processes involved in bone remodeling in a healthy state. In order to accomplish it, the agenda was divided in three different stages. First, a mechanical model combining meshless methods with a bone tissue remodeling algorithm was built and tested, based on the model proposed by Belinha [2]. By seeking the minimization of the strain energy density (SED) variable with respect to the bone apparent density, results were able to reproduce the trabecular morphology of bone. The solutions were obtained using three different numerical methods, namely the Finite Element Method (FEM), the Radial Point Interpolation Method (RPIM) and the Natural Neighbor Radial Point Interpolation Method (NNRPIM), using for the first time the RPIM in bone remodeling simulations.

Then, based on the biological model proposed by Ayati [3], a new spatiotemporal model of the cellular response observed during a single cycle of bone remodeling was created. Through him, this phenomenon was simulated for the first time in 2D, obtaining accurate results capable to describe the dynamics of bone cells.

After the validation of these two models, the mechanobiological model was idealized and tested. Using an experimental law that relates the levels of effective stress and the cell density of osteoblasts, results show the growth of bone according to the applied loads. However, further improvements have to be done in this model.

To conclude, with this work, new analysis in 2D were performed, with interesting and encouraging outcomes. The results obtained support the data existent in the literature, validating the models created and the possibility to test them in disease states. Ultimately, these *in silico* models will allow the development of novel therapies for bone remodeling disorders.

Resumo

Ao longo de décadas, vários investigadores têm dedicado o seu trabalho a estudar o osso, devido à sua capacidade de renovação contínua. Atualmente, o estudo e compreensão do fenómeno de remodelação óssea é cada vez mais importante e relevante. Isto porque, o conhecimento aprofundado acerca do funcionamento normal do osso facilita a construção da ponte que permite a descoberta da patogénese de vários distúrbios relacionados com a remodelação óssea. De entre estes distúrbios, estão incluídos a osteodistrofia renal, a doença de Paget, a osteopetrose e a osteoporose, que afeta mais de 200 milhões de pessoas em todo o Mundo [1]

Assim, o objetivo desta tese de mestrado é a criação de um modelo espácio-temporal capaz de replicar os processos biomecânicos e bioquímicos que ocorrem durante a remodelação óssea numa situação saudável. Para isso, o plano de trabalhos foi dividido em três componentes diferentes. Inicialmente, foi criado e testado um modelo mecânico, que combina um algoritmo de remodelação de tecido ósseo e métodos sem malha, baseado no modelo proposto por Belinha [2]. O modelo consiste na minimização da densidade de energia de deformação em relação à densidade óssea aparente e os resultados foram capazes de reproduzir a morfologia trabecular existente no osso. As soluções foram obtidas usando três métodos numéricos diferentes, nomeadamente o Método dos Elementos Finitos, o Método da Interpolação Radial e o Método da Interpolação Radial dos Vizinhos Naturais, sendo que foi a primeira vez que o Método da Interpolação Radial foi testado em simulações de remodelação óssea.

De seguida, foi criado um novo modelo espácio-temporal da resposta celular observada durante um ciclo de remodelação óssea, a partir do modelo de Ayati [3]. Este fenómeno foi simulado pela primeira vez em 2D, tendo-se obtido resultados capazes de descrever com muita acurácia o comportamento das células ósseas.

Após a validação destes dois modelos, o modelo mecanobiológico foi idealizado e testado. Recorrendo a uma lei experimental que relaciona os níveis de tensão efetiva e a densidade celular de osteoblastos, os resultados mostraram o crescimento ósseo de acordo com o desenho das cargas. No entanto, existem vários aspetos a melhorar neste modelo.

Concluindo, através deste trabalho, novas análises em 2D foram executadas, produzindo resultados interessantes e promissores. Estes resultados estão de acordo com a informação existente na literatura, validando os modelos criados e a possibilidade de os testar em estados de doença. No futuro, o objetivo ideal seria usar estes modelos *in silico* no desenvolvimento de novas terapias para doenças relacionadas com desequilíbrios durante a remodelação óssea.

Acknowledgments

Estes últimos 5 meses foram repletos de novos desafios, que teriam sido impossíveis de ultrapassar sem a ajuda do meu orientador, o Professor Jorge Belinha. Por isso, queria começar por agradecer profundamente pelo acompanhamento e dedicação constantes. O projeto era ambicioso e trabalhoso, não fosse a sua visão pragmática e um entusiasmo que me contagiava à medida que cada objetivo era cumprido. Gostava também de agradecer ao meu co-orientador, o Professor Renato Natal, pela sua disponibilidade e acompanhamento.

Mas, como para chegar aqui passaram 5 anos, queria agradecer também à minha família e aos meus amigos. À minha mãe pelos beijos, à minha avó pelos abraços, ao meu pai pelo mimo e ao meu avô pelos sorrisos. Às minhas irmãs Mariana por enlouquecer quando eu preciso e Inês pela loucura constante.

Queria agradecer também ao meu eterno Bando, aqueles amigos para sempre e a todas as amizades que fiz durante a Faculdade. Em especial, à Ana/Minguante/Nobe/Mingas/Berlim. Tantos nomes e todos com o mesmo significado: companhia inseparável.

Por fim, queria agradecer à Tuna Feminina de Engenharia, por me ter embalado durante estes 5 anos e mostrado que quando bem aproveitado, temos tempo para tudo. É um orgulho pertencer a este grupo e passar por tantas aventuras sempre na melhor companhia.

Funding

The author truly acknowledge the logistic conditions provided by Ministério da Educação e Ciência– Fundação para a Ciência e a Tecnologia (Portugal), under project funding UID/EMS/50022/2013 (funding provided by the inter-institutional projects from LAETA) and project NORTE-01-0145-FEDER-000022 - SciTech - Science and Technology for Competitive and Sustainable Industries, cofinanced by Programa Operacional Regional do Norte (NORTE2020), through Fundo Europeu de Desenvolvimento Regional (FEDER).

Additionally, the author truly acknowledge the work conditions provided by the department of Mechanical Engineering from FEUP and INEGI.

“This is where it all begins. Everything starts here, today”

David Nicholls, “One Day”

Contents

Abstract iii

Resumo v

Acknowledgments vii

Funding ix

Contents xiii

List of Figures xv

List of Tables xvii

List of Abbreviations xix

Chapter 1 1

Introduction 1
1.1 - Motivation 1
1.2 - Objectives 2
1.3 - Document Structure 2

Chapter 2 3

Bone Tissue 3
2.1 - Bone Morphology 3
2.2 - Bone Remodeling 4

Chapter 3 9

Numerical Methods 9
3.1 - FEM 9
3.2 - Meshless Methods 10

Chapter 4 19

Solid Mechanics 19
4.1 - Fundamentals 19
4.2 - Weak Form 21
4.3 - Discrete Equation System 23

Chapter 5 27

Mechanical Model 27

5.1 - Bone Tissue Material Law 27
5.2 - Proposed Model 29
5.3 - 2D Bone Patch Analysis 35
5.4 - Femoral 2D Analysis 39

Chapter 6 ..... **45**

Biological Model 45
6.1 - Komarova's Model 45
6.2 - Ayati's Model 47
6.3 - Proposed Model 48
6.4 - 2D Bone Patch Analysis 51

Chapter 7 ..... **55**

Mechanobiological Model 55
7.1 - Proposed Model 55
7.2 - 2D Bone Patch Analysis 58

Chapter 8 ..... **61**

Conclusions and Future Work 61

References **63**

List of Figures

Figure 2.1 - Transversal cross-section of an osteon (a) and a trabecular branch (b) [12]. 4

Figure 2.2 – Bone remodeling process [12] 5

Figure 2.3 - Regulation of osteoclast formation and activity as a result of the OPG/RANKL/RANK system. Cells of the osteoblastic lineage initiate bone remodeling by contact with osteoclastic progenitors. M-CSF stimulates the colony-stimulating factor-1 (c-fms) receptor on osteoclasts. Osteoclast differentiation and activity are stimulated by RANK/RANKL interaction, and this interaction can be blocked by soluble OPG. Osteoclastogenesis is influenced by various systemic hormones and local factors such as cytokines, parathyroid hormone (PTH), vitamin D, calcitonin and prostaglandin E (PGE) [9], [15]. 6

Figure 3.1 - Example of a mesh discretized for the FEM..... 10

Figure 3.2 - (a) Solid domain. (b) Regular nodal discretization. (c) Irregular nodal discretization [12]..... 11

Figure 3.3 - Examples of different types of influence-domains: (a) fixed rectangular shaped influence-domain, (b) fixed circular shaped influence-domain and (c) flexible circular shaped influence-domain [12]. 12

Figure 3.4 - (a) Second degree influence cell of interest point $\mathbf{xI}$. (b) Representation of the sub-cells forming the Voronoï cell. (c) Schematic representation of 4 × 4 integration points inside a sub-cell [76]. 13

Figure 3.5 - (a) Gaussian integration mesh and (b) transformation of the initial quadrilateral into an isoparametric square shape and application of the 2 x 2 quadrature point rule [12]..... 14

Figure 5.1 – Proposed bone remodeling algorithm for the mechanical model 32

Figure 5.2 - (a) Voronoï cell with the quadrature points. (b) Theoretical trabecular architecture of the sub-cell and homogenized apparent density. (c) Voronoï cell with the integration points homogenized apparent densities [90]. 33

Figure 5.3 - Isomap representing the trabecular architecture of the femoral bone..... 34

Figure 5.4 – Some screenshots of the FEMAS graphical user interface. 35

Figure 5.5 – (a) Regular nodal distribution (2 481 nodes). (b) Plate model geometry and essential and natural boundary conditions. (c) Benchmark example [91]. 36

Figure 5.6 - Evolution of the trabecular architecture with different types of mesh obtained using the FEM and the RPIM. The bone law used was Lotz's Law with $\boldsymbol{\beta} = \mathbf{0.1}$. 37

Figure 5.7 - Evolution of the trabecular architecture with increasing mesh sizes obtained using the FEM and the RPIM. The bone law used was Lotz's Law with $\boldsymbol{\beta} = \mathbf{0.1}$. 37

Figure 5.8 – Evolution of the trabecular morphology using Lotz's law 38

Figure 5.9 - – Evolution of the trabecular morphology using Belinha's law 39

Figure 5.10 – (a) Femoral X-ray plate. (b) Internal principal trabecular structures found in the femur bone. (c) Loads and constrains of the first mechanical case of the femur bone [12]. 40

Figure 5.11 – (a) Nodal distribution (1 303 nodes). (b) Model geometry and essential and natural boundary conditions. (c) Example obtained by Belinha [12] with the NNRPIM, using a nodal mesh of 5 991 nodes 41

Figure 5.12 – FEM solution for the first mechanical case: (a) Initial von Mises effective stress isomap; (b) Final von Mises effective stress isomap; (c) Final obtained trabecular architecture; (d) Final maximum strain isomap; (e) Final minimum strain isomap. 42

Figure 5.13 - RPIM solution for the first mechanical case: (a) Initial von Mises effective stress isomap; (b) Final von Mises effective stress isomap; (c) Final obtained trabecular architecture; (d) Final maximum strain isomap; (e) Final minimum strain isomap. 42

Figure 5.14 - NNRPIM solution for the first mechanical case: (a) Initial von Mises effective stress isomap; (b) Final von Mises effective stress isomap; (c) Final obtained trabecular architecture; (d) Final maximum strain isomap; (e) Final minimum strain isomap. 43

Figure 6.1 – Schematic representation of interactions between osteoclasts and osteoblasts included in Komariva's model [96]. 46

Figure 6.2 - Proposed bone remodeling algorithm for the biological model. 51

Figure 6.3 - (a) Mesh (383 nodes) used for the analysis, in which points inside the darker area are considered bone. (b) Initial distribution of osteoclasts indicated in black. (c) Initial distribution of osteoblasts indicated in black. 52

Figure 6.4 - Simulation of a bone remodeling cycle: (a) Changes with time in the cell density of osteoclasts and (b) osteoblasts. The dashed line represents the steady-state solution. 53

Figure 6.5 - Simulation of a bone remodeling cycle: Changes with time in bone mass. 53

Figure 6.6 – Simulation of a bone remodeling cycle: spatial variation of bone mass along time (days). 54

Figure 7.1 – (a) Experimental law [101]. (b) Second order polynomial approximation. 56

Figure 7.2 - Proposed bone remodeling algorithm for the mechanobiological model. 58

Figure 7.3 - Plate model geometry and essential and natural boundary conditions 59

Figure 7.4 - Spatial variation of bone mass along time (days). 59

List of Tables

Table 2.1 - Autocrine and paracrine regulation during bone remodeling.....6

Table 2.2 - Some hormones and other local factors and their effect during bone remodeling. 8

Table 5.1 - Coefficients of Lotz's Law. 28

Table 5.2 - Coefficients of Belinha's law. 28

Table 5.4 – Parameters of the RPIM. 36

Table 5.5 - Parameters of the NNRPIM. 36

Table 6.1 – Description of the regulatory factors considered in Komarova's model and their respective effect on bone cell dynamics. Identification of the parameter in which each factor is considered in the model's equations. 46

Table 6.2 – Parameters of the biological model. 52

List of Abbreviations

BMU	Bone Multi-cellular Units
c-fms	Colony-stimulating Factor-1
DEM	Diffuse Element Method
EFGM	Element Free Galerkin Method
FEM	Finite Element Method
FEMAS	Finite Element and Meshless Method Analysis Software
GUI	Graphical User Interface
M-CSF	Macrophage Colony Stimulating Factor
NEM	Natural Element Method
NNFEM	Natural Neighbor Finite Element Method
NNRPIM	Natural Neighbor Radial Point Interpolation Method
OPG	Osteoprotegerin
PGE	Prostaglandin E
PIM	Point Interpolation Method
PTH	Parathyroid Hormone
RANK	Receptor Activator of NF-Kb
RANKL	Receptor Activator of NF-kB Ligand
RBF	Radial Basis Function
RPI	Radial Point Interpolators
RPIM	Radial Point Interpolation Method
SED	Strain Energy Density
SPH	Smooth Particle Hydrodynamics
TGF-β	Transforming Growth Factor-β

Chapter 1

Introduction

Biomedical research, including bone biology, is most commonly “hypothesis driven”, starting always with an assumption of how a biological system might behave [4]. Knowing *a priori* that the subject in study is complex, the real phenomenon has to be simplified giving rise to a conceptual model.

In bone biology, the most famous conceptual model was proposed by Frost, known as the mechanostat theory [5]. This theory, originated from Wolff's law, states that “in a healthy subject, bone will adapt to the loads it experiences”. In his study, Frost suggested that mechanical load can be sensed by bone tissue and proposed the existence of certain feedback controls that translate information of the mechanical environment to bone cells, causing changes in bone mass and strength.

However, bone plays both local and systemic functions that interconnect with each other. Because of this, the understanding of all the different mechanisms of regulation during the bone remodeling process turns out to be extremely challenging. Also, to understand biomechanical and hormonal regulation of bone composition and architecture, studies at different dimensional scales are required [4].

So, these studies can be performed using experimental or mathematical models. This chapter compares these two types of models, weighting its advantages and limitations. Through this discussion, the motivation of this work is presented. Then, the objectives of this dissertation are presented, as well as the organization of this document.

1.1 - Motivation

After the formulation of the hypothesis, the conceptual model is tested. In life science, the rooted path is validation through experimental studies. But, *in vitro* and *in vivo* models have their strength and potential weaknesses, since they frequently use supra-physiological extremes such as maximal inhibition of specific pathways [4]. Also, interpretation of experimental data depends heavily on assumptions. For instance, it has to be assumed that the modeled processes with *in vivo* tests are similar to those occurring in humans, since humans cannot be directly used as experimental objects

Conscious of the limitations of experimental studies, mathematical models appear to be a promising link between conceptual models and experimental testing. In fact, mathematical

modelling has proven to be a powerful tool to formalize the conceptual model and simulate proposed experiments *in silico*. Thus, mathematical modelling allows the validation of a conceptual model, the identification of the most influential parameters and ultimately the prediction of an experimental outcome consistent with the conceptual model. Additionally, these models have shown to be a valuable help when different events with different time scales are being simultaneously studied and when the system exhibits non-linear behavior, like the case of bone remodeling. Also, when exists a solid connection between mathematical and experimental models, the consequent flow of information between them lead to biological systems with highly enhanced accuracy. However, as the complexity of the question under investigation increases, the required mathematical model has to be more sophisticated and complex.

But, when weighting the advantages and the limitations of these models, the numerous possibilities that they can offer prevail. And, in fact, it was those promising and, in many cases, already proven results, that fed the motivation for this work.

1.2 - Objectives

The main objective of this project is to develop a new mechanobiological model to predict the bone tissue remodeling process, reproducing accurately the biological response in the presence of a mechanical stimulus.

Therefore, to accomplish this goal, several secondary objectives were stipulated, such as:

- Understand the influence of stress in bone tissue during a remodeling phenomenon;
- Develop a bone tissue remodeling algorithm only taking in consideration mechanical stimuli;
- Validate the mechanical model through a 2D analysis, using different numerical methods;
- Study the relevance of hormonal/chemical external effects;
- Develop a 2D diffusion model of bone remodeling considering the cellular behavior of bone cells;
- Validate the biological model through a 2D analysis, using different numerical methods.

1.3 - Document Structure

The thesis was organized in several chapters, starting with Chapter 1, in which the theme in study and the main objectives of the work are presented. Chapter 2 describes the biological process of bone remodeling and its mechanisms of regulation. Chapter 3 focus on the three numerical methods used in this work, describing briefly their formulation, followed by, in Chapter 4, an introduction of basic notions of solid mechanics. Then, in Chapters 5 and 6, respectively, the mechanical and the biological models created are presented, as well as the results obtained for each model. In Chapter 7, the focus is on a full description of the new mechanobiological model proposed in this work. To finish, in Chapter 8, the main achievements of the work are presented along with the suggestion of future work that could be implemented.

Chapter 2

Bone Tissue

Bone is a highly reactive tissue. The relationship between bone mechanical environment and bone internal and external structure was first described by J.Wolff, who suggested that bone grows wherever needed and decreases where is not needed [6].

Thus, the subject of this chapter is bone and its remodeling process. Additionally, both biological and mechanical regulation will be described.

2.1 - Bone Morphology

The skeletal system is constituted by bone and cartilage and has two main functions in the organism - mechanical and metabolic. Regarding the first one, skeletal system allows support and protection of vital internal organs, as well as muscle attachment for locomotion [7]. The skeleton is also considered a mineral repository, especially of calcium and phosphate, having an important metabolic action for the maintenance of serum homeostasis. Additionally, in the red marrow of the bone, blood cells, such as erythrocytes, leucocytes and platelets, are produced [8].

Bone is a porous mineralized structure made up of cells, vessels, collagen and crystals of calcium compounds (hydroxyapatite) [7]. The variation of their proportion originates two different types of bone – cortical and trabecular. Thus, although having identical chemical composition, this variation causes different structural macroscopically and microscopically organizations.

Cortical bone comprises 80% of the skeleton and can be found in the outer part of all skeletal structures. The basic functional unit of cortical bone is the osteon, which consists of concentric layers of bony lamellae surrounding a central Haversian canal, which contains the blood capillaries that supply the bone tissue. It has a slow turnover rate and is a compact material, as represented in Figure 2.1a. Its high density leads to a high resistance to bending and torsion. On the other hand, trabecular bone represents 20% of the skeletal mass and is a complex network of intersecting curved plates and tubes in the inner part of the skeletal structures (Figure 2.1b). When compared to cortical bone, it is less dense and more elastic. Also, while cortical bone has an important mechanical function, trabecular bone exhibits a major metabolic function, having a higher turnover rate. Lastly, regardless of its relatively small volume and high apparent porosity, trabecular bone is well adapted to resist and

conduct compressive loads. In long bones, trabecular bone is typically located at the proximal ends, having an arrangement relatively regular that reflects the direction of the principal mechanical stresses to which this kind of bone is being subjected [8].

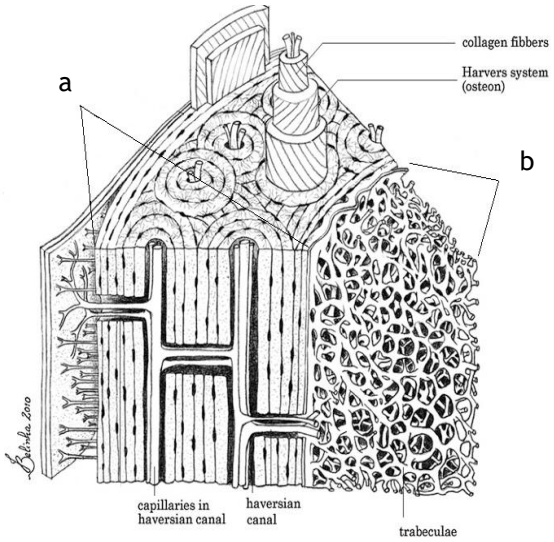

Figure 2.1 - Transversal cross-section of an osteon (a) and a trabecular branch (b) [12].

Lastly, bone is a living tissue experimenting a continuous reconstruction and reformulation along its life span [9]. Therefore, to maintain the shape, quality and size of the skeleton bone is constantly remodeling.

2.2 - Bone Remodeling

Bone remodeling is a complex process by which old bone is continuously replaced by new tissue, repairing micro fractures and modifying its structure in response to stress and other biomechanical forces. The process is sequential, as can be depicted in Figure 2.2, starting by an activation phase followed by resorption, reversal and formation phases. The bone cells active in the process are the osteoclasts and the osteoblasts, which are temporally and spatially coupled, closely collaborating within bone multi-cellular units (BMUs). The organization of the BMUs in cortical and trabecular bone is morphologically different, since trabecular bone is more actively remodeled than cortical bone. Nevertheless, there are no differences between the two types of bone when it comes to the biological events during bone remodeling [7].

The remodeling cycle begins with the resorption phase, in which osteoclasts have the leading role. Osteoclasts are giant multinucleated cells, derived from hematopoietic cells of the mononuclear lineage [10] and are the bone lining cells responsible for bone resorption. Thus, the resorption phase starts with the activation of a quiescent bone surface through a cascade of signals to osteoclastic precursors, causing their migration to the bone surface, where they form multinucleated osteoclasts [11] (Figure 2.2a). Simultaneously, bone-lining cells disappear from the bone surface, allowing osteoclasts to adhere to the bone matrix and resorb bone [7] (Figure 2.2b).

After the completion of the resorption, mononuclear cells appear on the bone surface releasing signals for osteoblast differentiation and migration (Figure 2.2c). This phase is

known as the reversal phase, since it prepares the bone surface for the arrival of new osteoblasts and consequently the formation of new bone [7].

Osteoblasts are the cells responsible for the production of bone matrix constituents and are originated from multipotent mesenchymal stem cells. During the formation phase, osteoblasts lay down bone until the resorbed bone is completely replaced by new one (Figure 2.2d). In this phase, osteoblasts start by synthesizing and depositing collagen. Then, the production of collagen decreases, and a secondary full mineralization of the matrix takes place. In this step, the collagen matrix built previously acts as the scaffold in which minerals such as phosphate and calcium begin to crystalize to form bone [7], [11]. Toward the end of the matrix-secreting period (Figure 2.2e), 15% of mature osteoblasts are entrapped in the new bone matrix and differentiate into osteocytes, while some cells remain on the bone surface, becoming flat lining cells [7].

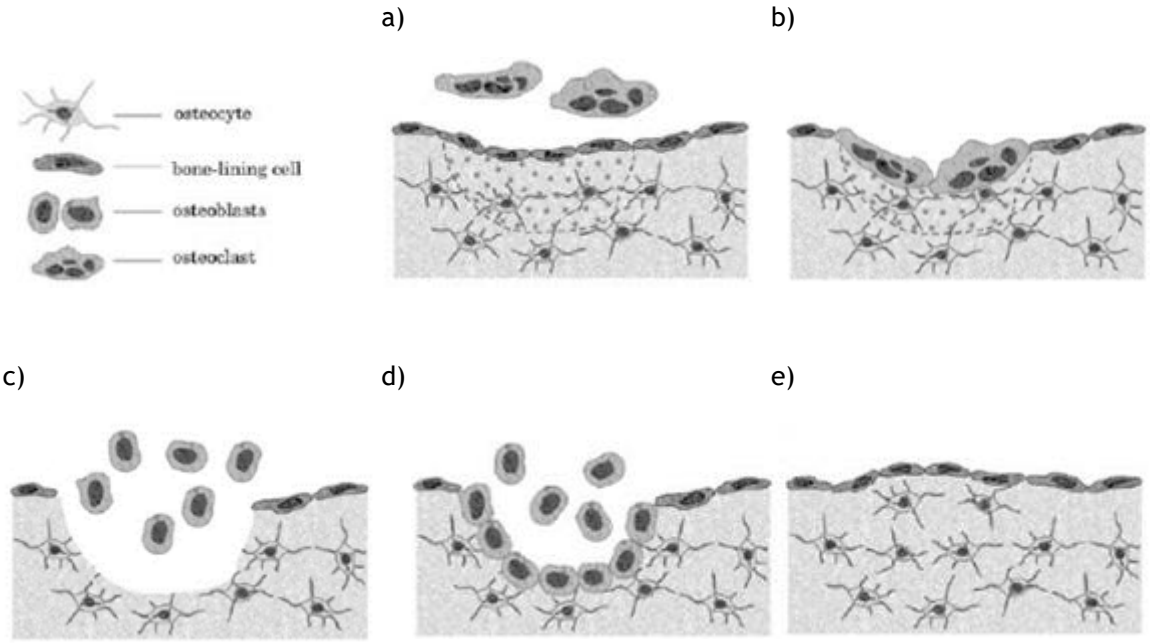

Figure 2.2 – Bone remodeling process [12]

2.2.1 - Regulation Mechanisms

So, during a remodeling cycle, the turnover of bone is managed by a sequential process performed by the bone cells within a BMU, in which the activities of bone-forming osteoblasts and bone-resorbing osteoclasts have to be coordinated. These activities of osteoblasts and osteoclasts are controlled by a variety of hormones and cytokines, as well as by mechanical loading [13].

For instance, during the resorption phase, protein and mineral components of bone and various local paracrine and autocrine regulatory factors are released, such as the receptor activator of NF-kB ligand (RANKL), the receptor activator of NF-Kb (RANK) or the osteoprotegerin (OPG) [11].

The RANKL/RANK interaction is, in fact, critical for this resorption phase. Protein RANKL is a ligand for RANK on hematopoietic cells, and it is the primary driver of formation, activation and survival of osteoclasts [14]–[19]. So, the major biological action of RANKL,

together with the protein ligand macrophage colony stimulating factor (M-CSF) is to induce osteoclast activation and in this way promote bone resorption [16], [20], [21]. RANK receptor is found on the surface of osteoclastic progenitors and osteoclasts, while the major source of RANKL in physiologic bone remodelling are cells of the stromal/osteoblastic lineage. However, other cells may act as a source of RANKL in pathologic states.

To counteract the differentiation and activation of osteoclasts, osteoblasts produce and secrete OPG, a decoy receptor that can block RANKL/RANK interactions [11], [14]. The critical biological role of OPG is then the inhibition of osteoclast function and the acceleration of osteoclast apoptosis [22]. Therefore, the OPG/ RANKL/ RANK system is considered the major regulatory system in which the coordination of osteoclastogenesis and bone remodelling converges [23]–[25], as can be depicted in Figure 2.3

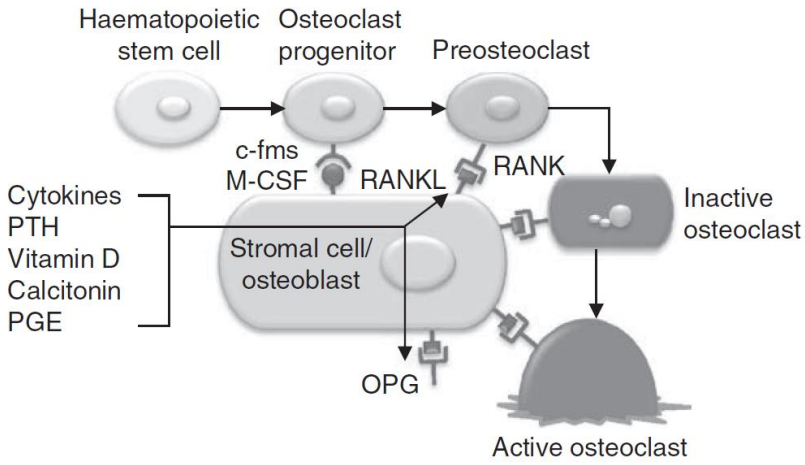

Figure 2.3 - Regulation of osteoclast formation and activity as a result of the OPG/RANKL/RANK system. Cells of the osteoblastic lineage initiate bone remodeling by contact with osteoclastic progenitors. M-CSF stimulates the colony-stimulating factor-1 (c-fms) receptor on osteoclasts. Osteoclast differentiation and activity are stimulated by RANK/RANKL interaction, and this interaction can be blocked by soluble OPG. Osteoclastogenesis is influenced by various systemic hormones and local factors such as cytokines, parathyroid hormone (PTH), vitamin D, calcitonin and prostaglandin E (PGE) [9], [15].

Despite this, there are limitations regarding this system since it is difficult, if not impossible, to assess the RANKL and OPG status in patients without invasive procedures such as bone biopsies. In Table 2.1, the OPG/RANKL/RANK is resumed, defining the principal action of each regulatory factor and its origin.

Table 2.1 - Autocrine and paracrine regulation during bone remodeling.

Factor	Origin	Action
RANKL	Surface of stromal/osteoblastic lineage	Activation of osteoclasts
RANK	Surface of osteoclastic lineage	
OPG	Secreted by osteoblasts	Inhibition of osteoclasts

Besides these local paracrine and autocrine effectors, local cytokines and growth factors have also an important role in bone remodelling, acting either as stimulators or as inhibitors of bone resorption or bone formation. Some of these factors act independently of the cytokines RANKL and OPG, and are necessary factors in the recruitment and differentiation of osteoblastic and osteoclastic cells. A subset of examples include members of the transforming

growth factor-β (TGF-β) family, tumour necrosis factor-α, various interleukins, insulin-like growth factors I and II, prostaglandin E2 and M-CSF [14], [23]–[31]. For instance, TGF- β belongs to a family of closely related polypeptides, in which TGF- β 1, 2, and 3 have similar effects on bone cell function [32]. TGF-β is released by osteoclasts during bone resorption [33] making bone matrix the largest source of TGF-β in the body [34]. Its effect on osteoblasts is bi-directional depending upon the state of maturation of osteoblasts [35]. In vivo studies have confirmed a stimulatory effect of TGF-β on bone formation [36]–[38], suggesting a potential to stimulate osteoblast recruitment, migration and proliferation of osteoblast precursors [33], [39]. On the other hand, it was also found that TGF-β inhibits terminal osteoblastic differentiation [40], by inhibiting alkaline phosphatase activity and osteocalcin synthesis [32]. The actions of TGF-β on bone resorption has a biphasic effect on osteoclastogenesis [32]. At low concentrations it enhances osteoclast formation, whereas at high concentrations induces osteoclast apoptosis [34], [41].

Along with this local regulation, bone remodelling involves also a systemic regulation controlled by hormones, such as estrogen and calcium-regulating hormones. It is known that activation of estrogen receptors in osteoclast progenitor cells decreases osteoclast formation and enhances apoptosis. Also, activation of estrogen receptors in terminally differentiated osteoclasts inhibits their bone-resorbing activity [13], [42]–[45]. But, although the loss in bone mass caused by estrogen deficiency is primarily due to enhanced bone resorption, decreased bone formation is also a contributing factor [46], [47]. It has been shown that stimulation of estrogen receptors in osteoblasts activates their anabolic activities and decreases the pathway by which osteoblasts can activate osteoclasts [13]. Estrogen also stimulates the expression of type I collagen, and decreased levels of estrogen would result in osteoblasts less active in producing an extracellular matrix [48]. Activation of the estrogen receptors in osteoblasts/stromal cells may also play a role in the regulation of osteoclastogenesis, by decreasing the expression of M-CSF [49]–[51]. This way, accordingly to this data, it is possible to conclude that estrogen is crucial for keeping bone mass in balance.

But, there are other systemic hormones that affect bone turnover. The mineral homeostatic mechanisms in the skeleton are controlled by the calcium-regulating hormones, which are PTH, calcitriol, that is the active hormonal form of 25-OH-vitamin D, and calcitonin, the active metabolite of 25-OH-vitamin D [24].

PTH is an important regulator of calcium homeostasis and rapidly influences its concentrations since stimulates bone resorption by increasing renal calcium reabsorption [11]. However, the study of the actions of PTH when administered in the organism is more complex due to its multiple effects. When given continuously, PTH induces bone loss, whereas in intermittent applications it stimulates bone gain. On the other hand, calcitriol exerts a tonic inhibitory effect on PTH synthesis and is necessary for optimal intestinal absorption of calcium and phosphorus [52]. Ultimately, calcitonin increases the transformation of 25-OH-vitamin D to its active metabolite, leading indirectly to an increase in calcium concentrations [7], [25], [26], [53], [54].

In Table 2.2, it is resumed the main actions of some of the hormones and cytokines talked above and their influence on the activities of osteoblasts and osteoclasts

Table 2.2 - Some hormones and other local factors and their effect during bone remodeling.

Factor	Action
Estrogen	Increase rate of bone remodeling
PTH	Continuous administration - induces bone loss
	Intermittent applications - stimulates bone gain
TGF-β	Low concentration – enhances osteoclast formation
	High concentration – osteoclast apoptosis

Lastly, mechanical loading is also a very important factor to take into account, since osteocytes respond to bone tissue strain and enhance bone remodelling activity [7]. Therefore, osteocytes convert mechanical stimuli into metabolic responses, organizing bone turnover under mechanical strain and immobilization [53], [55], [56]. Being descended from osteoblasts, they have similar paracrine capabilities, influencing the balance between RANKL and OPG regarding bone turnover mechanism. Increased mechanical strain inhibits RANKL and upregulates OPG, which decreases osteoclastic activity and therefore increases bone mass indirectly through the osteocytes [7]. Loading plays then an important role. A low amount of loading leads to bone loss, due to decreased anabolic activity of osteoblasts and increased osteoclastic resorption, and high loading causes increased bone mineral density, due to the anabolic activation of osteoblasts [13].

In conclusion, remodeling is a lifelong coordinated and dominant process in the adult skeleton, initiated by resorption and followed by new bone formation at the same site where the resorption process occurred [24]. Bone remodeling is important for the maintenance of bone mass, to repair micro damage of the skeleton, to prevent accumulation of too much old bone and for mineral homeostasis [24].

Chapter 3

Numerical Methods

Many phenomena in nature such as heat conduction, stress in mechanical structures, electromagnetic fields or fluid mechanics involve either domains of two or more dimensions or nonlinear effects [57]. Thus, to simulate these processes it is required to use partial differential equations or nonlinear differential equations, and the bone remodelling process is no exception. But, in general, none of these equations can be solved symbolically or analytically, so researchers need to use numerical methods [57]. Thanks to the advancement of high-speed digital computers, the cost-effectiveness of numerical procedures has been greatly enhanced, and these methods have become very accurate and reliable [58].

In the work developed, the numerical methods used were determinant to the success of the simulation models created. So, this chapter begins with a very brief introduction about the FEM, followed by a more detailed analysis of two meshless methods, namely the RPIM and the (NNRPIM), reporting some of the most important concepts of these two numerical methods.

3.1 - FEM

As previously mentioned, with the increase in complexity of the problems studied, the need of a method of approximation to solve these continuum problems was urgent. This led to the first definition of a unified treatment of "standard discrete problems", known as FEM.

FEM approach breaks the domain into a finite number of pieces called elements, and uses basis functions, usually piecewise polynomials that are local to each element [59], [60]. FEM is then characterized by the discretization of the domain into several subdomains called finite elements [58], that construct a mesh, as illustrated in Figure 3.1. These elements can be irregular and possess different properties enabling the discretization of structures with mixed properties [58].

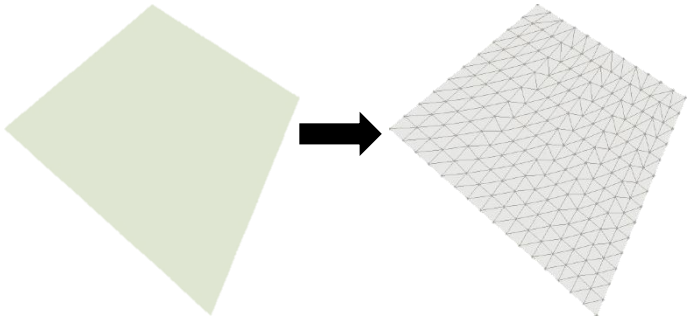

Figure 3.1 - Example of a mesh discretized for the FEM

FEM has been used with great success on many fields of engineering. However, this method is not free of limitations. The main one is related with the mesh based-interpolation [61]. Special attention has to be given to the quality of the mesh, because low quality meshes lead to high values of error. Being a classical mesh-based method, FEM is not suitable to treat problems with discontinuities that don't align with element edges [61].

3.2 - Meshless Methods

Since FEM's performance relies greatly on the quality of the mesh, other numerical methods were created and offered as solid options. Meshless methods were one of the options created, in which the problem physical domain is discretized in an unstructured nodal distribution and the field functions are approximated within an influence-domain rather than an element [12], [62], [63].

Regarding the formulation, meshless methods can be classified in two categories. The first one is the strong formulation in which the partial differential equations describing the phenomenon are used directly to obtain the solution [12]. One of the first meshless methods created in this category was the smooth particle hydrodynamics (SPH) method. A parallel path on the development of meshless methods was initiated in the 1990's using this time a weak form solution. In weak formulation, each differential equation has a residual weight to be minimized. The residual is not given by the exact solution of the differential but by an approximated function affected by a test function [12]. The first meshless method using this formulation was the Diffuse Element Method (DEM) proposed by Nayroles [64]. Belytschko extended this method and proposed one of the most well-known methods, the Element Free Galerkin Method (EFGM) [65].

Meshless methods described above are approximants, and in spite of the successful applications of these type of meshless methods in computational mechanics, some problems remained unsolved, being the lack of the Kronecker delta property on the approximation functions the most important one [12].

Due to this fact, several interpolant meshless methods were developed, such as Point Interpolation Method (PIM) [66], the RPIM [67], [68], Natural Neighbour Finite Element Method (NNFEM) [69], [70] and the Natural Element Method (NEM) [71], [72]. The combination between the NEM and the RPIM originated the NNRPIM [12], [73].

3.2.1 - Meshless Generic Procedure

To initialize the process, the only information required is the spatial location of each node discretizing the problem domain. It is important to notice that this nodal distribution do not form a mesh, since it is not required any kind of previous information about the relation between each node in order to construct the approximation or interpolation functions of the unknown variable field functions [12]. In Figure 3.2, it is possible to observe an illustration of this process.

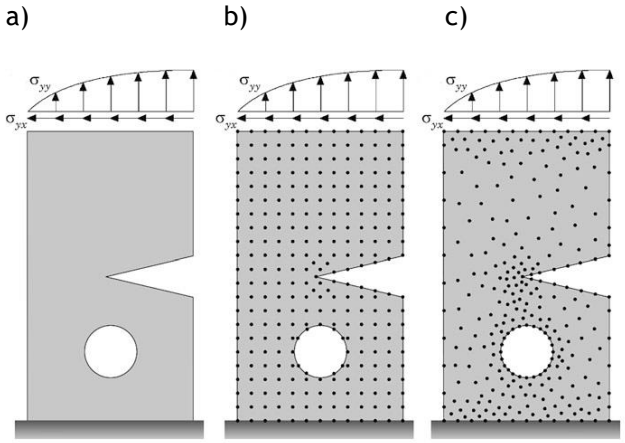

Figure 3.2 - (a) Solid domain. (b) Regular nodal discretization. (c) Irregular nodal discretization [12].

After the discretization, nodal connectivity can be imposed using either influence-domains or Voronoï diagrams. Then, the construction of a background integration mesh is needed. As in FEM, it is common to use Gaussian integration meshes fitted to the problem domain. But there are other techniques, such as the use of the nodal integration, resorting to the Voronoï diagrams in order to obtain the integration weight on each node [12]. The following step is the establishment of the equation system, that can be can be formulated using approximation or interpolation functions. The interpolation functions possess an important property, namely Kronecker delta property, meaning that the function obtained passes through all scattered points in an influence domain. This property is an important advantage, since it allows the use of the same simple techniques used in FEM to impose the essential boundary conditions.

Thus, after a brief analysis of the generic procedure of meshless methods, it is possible to conclude that a meshless method requires the presence and combination of three basic parts: nodal connectivity, numerical integration scheme and shape functions. These three concepts will be analyzed and, since RPIM and NNRPIM differ in respect to both nodal connectivity and numerical integration scheme, the following sections will explain with detail these differences.

3.2.2 - Nodal Connectivity

3.2.2.1 - RPIM

The RPIM is based on the Galerkin weak form formulation using meshfree shape functions constructed using radial basis functions (RBF).

In RPIM, the nodal connectivity is obtained by the overlap of the influence-domain of each node. Influence-domains are found by searching enough nodes inside a certain area or volume, and can have a fixed or a variable size. Many meshless methods [67], [74], [75] use fixed size influence-domains, but RPIM uses a fixed number of neighbor nodes instead.

Regarding fixed size influence-domains, in Figure 3.3, it is presented an example of two types of fixed size domains, a rectangular (Figure 3.3a) and a circular (Figure 3.3). By analyzing these figures, it is possible to note that influence-domains with different shapes and sizes originate different nodal connectivities. Also, depending on the initial nodal spatial distribution, influence-domains obtained can be unbalanced, not containing an approximately constant number of nodes. All of these factors can affect the final solution of the problem and cause loss of accuracy in the numerical analysis.

Therefore, to overcome these limitations, RPIM uses variable size influence-domains, with constant number of nodes inside the domain. Thus, performing a radial search and using the interest point $\boldsymbol{x}_I$ as center, the *n* closest nodes are found. In Figure 3.3c, this process is illustrated, culminating in a constant nodal connectivity that avoids the numerical problems identified previously.

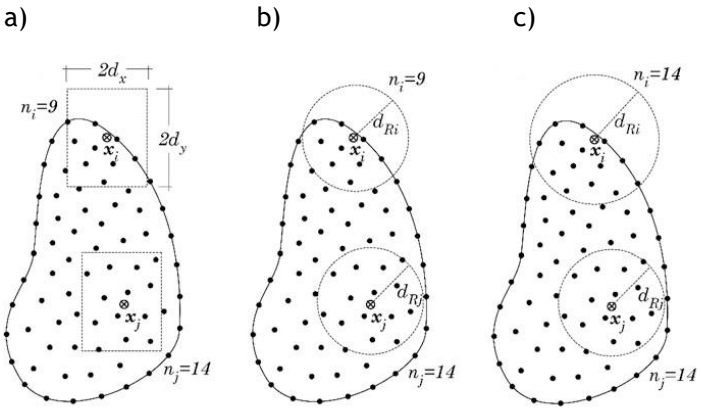

Figure 3.3 - Examples of different types of influence-domains: (a) fixed rectangular shaped influence-domain, (b) fixed circular shaped influence-domain and (c) flexible circular shaped influence-domain [12].

3.2.2.2 - NNRPIM

The NNRPIM is an advanced discretization meshless technique combining the natural neighbor geometric concept with the radial point interpolators (RPI) [76].

Nodal connectivity is obtained using the natural neighbor concept with the partition of the discretized domain into a set of Voronoï cells [77]. To each one of these cells is associated one and only one node [76]. Considering a problem domain $\Omega \subset \mathbb{R}^2$, bounded by a physical boundary $\Gamma \in \Omega$, discretized in several randomly distributed nodes $N = \{n_0, n_1, \dots, n_N\} \in \mathbb{R}^2$ with the following coordinates: $X = \{x_0, x_1, \dots, x_N\}$ with $x_i \in \mathbb{R}^2$, the Voronoï cell is defined by

$$V_i := \{x_I \in \Omega \subset \mathbb{R}^d : \|x_I - x_i\| < \|x_J - x_j\|, \quad \forall\ i \neq j\} \tag{3.1}$$

being x_I an interest point of the domain and ‖ · ‖ the Euclidian metric norm [12]. Thus, the Voronoï cell V_i is the geometric place where all points in the interior V_i are closer to the node n_i than to any other node [12]. The assemblage of the Voronoï cells define the Voronoï diagram. Thus, the Voronoï diagram of *N* is the partition of the domain defined by Ω into sub regions V_i , closed and convex, as can be seen in Figure 3.4a.

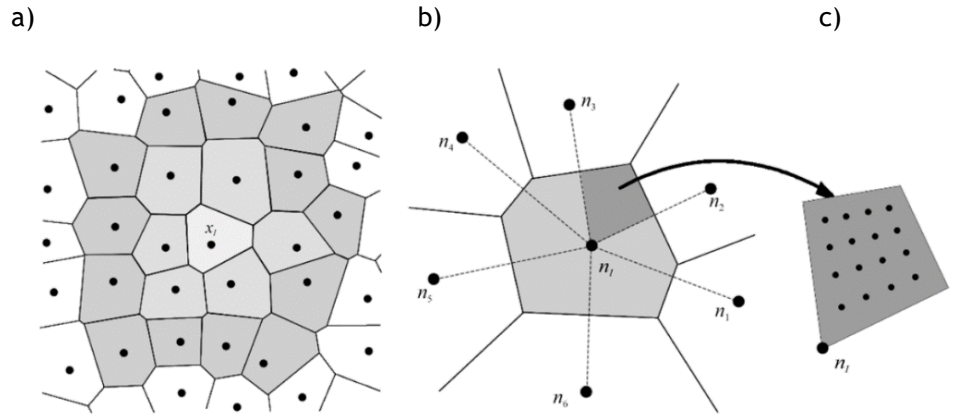

Figure 3.4 - (a) Second degree influence cell of interest point $\mathbf{x_I}$. (b) Representation of the sub-cells forming the Voronoï cell. (c) Schematic representation of 4 × 4 integration points inside a sub-cell [76].

In the NNRPIM, influence cells are organic influence-domains that are built using the information from the Voronoï diagram, making them dependent on the nodal mesh arrangement.

In this work, it was determined the "second degree influence-cell". To establish them, a point of interest, x_I, starts by searching for its neighbour nodes following the Natural Neighbor Voronoï construction, considering only its first natural neighbors. Then, based again on the Voronoï diagram, the natural neighbors of the first natural neighbors of x_I are added to the influence-cell, as it is represented in grey in Figure 3.4a.

3.2.3 - Numerical Integration

3.2.3.1 - RPIM

For the numerical integration, RPIM uses the Gauss-Legendre quadrature scheme. Initially, the solid domain is divided in a regular grid as Figure 3.5a indicates. Then, each grid-cell is filled with integration points, respecting the Gauss-Legendre quadrature rule, as illustrated in Figure 3.5b.

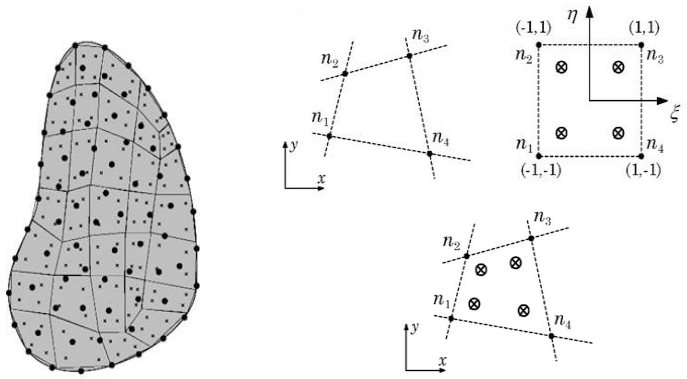

Figure 3.5 - (a) Gaussian integration mesh and (b) transformation of the initial quadrilateral into an isoparametric square shape and application of the 2 x 2 quadrature point rule [12].

The Cartesian coordinates of the quadrature points are obtained using isoparametric interpolation functions, N_i, present in Equations (3.2) and (3.3).

$$\begin{aligned} N_1(\xi,\eta) &= \frac{1}{4}(1-\xi)(1-\eta) \\ N_2(\xi,\eta) &= \frac{1}{4}(1-\xi)(1+\eta) \\ N_3(\xi,\eta) &= \frac{1}{4}(1+\xi)(1+\eta) \\ N_4(\xi,\eta) &= \frac{1}{4}(1+\xi)(1-\eta) \end{aligned} \tag{3.2}$$

$$\begin{aligned} N_1(\xi,\eta) &= 1-\xi-\eta) \\ N_2(\xi,\eta) &= \eta \\ N_3(\xi,\eta) &= \xi \end{aligned} \tag{3.3}$$

The Cartesian coordinates are given by

$$\begin{aligned} x &= \sum_{i=1}^{m} N_i(\xi,\eta)\cdot x_i \\ y &= \sum_{i=1}^{m} N_i(\xi,\eta)\cdot y_i \end{aligned} \tag{3.4}$$

in which m is the number of nodes inside the grid-cell and x_i and y_i are the Cartesian coordinates of the cells nodes.

The integration weight of the quadrature point is obtained by multiplying the isoparametric weight of the quadrature point with the inverse of the Jacobian matrix determinant of the respective grid-cell, as described in the Equation (3.5).

$$[J] = \begin{pmatrix} \frac{\partial x}{\partial \xi} & \frac{\partial x}{\partial \eta} \\ \frac{\partial y}{\partial \xi} & \frac{\partial y}{\partial \eta} \end{pmatrix} \tag{3.5}$$

3.2.3.2 - NNRPIM

Since the NNRPIM uses the Galerkin weak form, a background integration mesh is necessary. In this method, the integration mesh is obtained using directly and exclusively the nodal distribution, namely the previously constructed Voronoï diagram [78]. Using the Delaunay triangulation, the area of each Voronoï cell is subdivided in several sub-areas. Thus, each area of the Voronoï cell of node $\boldsymbol{x}_j$, A^{V_j}, is divided into *k* sub-areas $\mathrm{A}_{\mathrm{i}}^{\mathrm{V_j}}$, in which $A^{V_j} = \sum_{i=1}^{k} \mathrm{A}_{\mathrm{i}}^{\mathrm{V_j}}$, as can be seen in Figure 3.4b. Then, following the Gauss–Legendre quadrature rule, it is possible to distribute integration points inside each subarea $\mathrm{A}_{\mathrm{i}}^{\mathrm{V_j}}$. In Figure 3.4c, it is exemplified a 4x4 distribution. By repeating the mentioned procedure for the *N* Voronoï cells from the Voronoï diagram, the background integration mesh discretizing the problem domain is obtained.

In this work, the integration mesh is constructed considering just one integration point per sub-area $\mathrm{A}_{\mathrm{i}}^{\mathrm{V_j}}$, since previous research works on the NNRPIM show that this simple integration scheme is sufficient to integrate accurately the integro-differential equations [73], [76].

3.2.4 - Interpolation Functions

Considering the RPIM and the NNRPIM, the interpolation functions for both methods possess the Kronecker delta property, satisfying the following condition,

$$\varphi_i(\boldsymbol{x}_j) = \delta_{ij} \tag{3.6}$$

where δ_{ij} is the Kronecker delta, $\delta_{ij} = 1$ if $i = j$ and $\delta_{ij} = 0$ if $i \neq j$. This property simplifies greatly the process of imposition of the essential boundary conditions, because it allows to apply them directly in the stiffness matrix.

The interpolation functions for both methods are determined using the RPI technique [67], which requires the combination of a polynomial basis with a RBF. So, considering the function $u(\boldsymbol{x}_I)$ defined in the domain $\Omega \subset \mathbb{R}^2$, the value of function $u(\boldsymbol{x}_I)$ at the point of interest $\boldsymbol{x}_I$ is defined by

$$u(\boldsymbol{x}_I) = \sum_{i=1}^{n} R_i(\boldsymbol{x}_I) \cdot a_i(\boldsymbol{x}_I) + \sum_{j=1}^{m} p_j(\boldsymbol{x}_I) \cdot b_j(\boldsymbol{x}_I) = \boldsymbol{R}^T(\boldsymbol{x}_I) \cdot \boldsymbol{a}(\boldsymbol{x}_I) + \boldsymbol{p}^T \cdot \boldsymbol{b}(\boldsymbol{x}_I) \tag{3.7}$$

where $R_i(\boldsymbol{x}_I)$ is the RBF, $p_j(\boldsymbol{x}_I)$ is the polynomial basis function and $a_i(x_I)$ and $b_j(\boldsymbol{x}_I)$ are non-constant coefficients of $R_i(x_I)$ and $p_j(\boldsymbol{x}_I)$, respectively [76]. The variable defined on the RBF is the distance $\mathbf{r_{Ii}}$ between the relevant node $\boldsymbol{x_I}$ and the neighbour node x_i, given by $\mathrm{r_{Ii}} = |\boldsymbol{x}_i - \boldsymbol{x}_I|$. The RBF used in this work is the Multiquadric RBF [79], $R_i(x_I) = R(\mathrm{r_{Ii}}) = (r_{Ii}^2 + c^2)^p$, in which shape parameter c takes a value close to zero, $c \cong 0$, and p close to one, $p \cong 1$ [73], [80]. Regarding the Equation (3.7), it is still needed to obtain the non-constant coefficients $\boldsymbol{a}$ and $\boldsymbol{b}$. The polynomial basis functions used have the following monomial term as

$$\boldsymbol{p}^T(\boldsymbol{x}_I) = [1, x, y, x^2, xy\,, y^2, \dots] \tag{3.8}$$

Considering Equation (3.7) for each node inside the influence-cell domain and including an extra equation, $\sum_{i=1}^{n} p_j(\boldsymbol{x}_I)a_i = 0$, in order to guarantee a unique solution [81], a system of equations defined in Equation (3.9) is obtained.

$$\begin{bmatrix} \boldsymbol{R} & \boldsymbol{p} \\ \boldsymbol{p}^T & 0 \end{bmatrix} \begin{Bmatrix} \boldsymbol{a} \\ \boldsymbol{b} \end{Bmatrix} = \begin{Bmatrix} \boldsymbol{u_S} \\ 0 \end{Bmatrix} \tag{3.9}$$

Through this system of equations, and being the vector of the nodal function values for the nodes on the influence-cell defined by: $\boldsymbol{u}_S = \{u_1, u_2 \dots u_n\}^T$ these coefficients are determined (Equation (3.10).

$$\begin{Bmatrix} \boldsymbol{a} \\ \boldsymbol{b} \end{Bmatrix} = \begin{bmatrix} \boldsymbol{R} & \boldsymbol{p} \\ \boldsymbol{p}^T & 0 \end{bmatrix}^{-1} \begin{Bmatrix} \boldsymbol{u_S} \\ 0 \end{Bmatrix} \Longrightarrow \begin{Bmatrix} \boldsymbol{a} \\ \boldsymbol{b} \end{Bmatrix} = \boldsymbol{M}^{-1} \begin{Bmatrix} \boldsymbol{u_S} \\ 0 \end{Bmatrix} \tag{3.10}$$

Recalling that a certain field variable value for an interest point $\boldsymbol{x}_I$ is interpolated using the shape function values obtained at the nodes inside the support domain of $\boldsymbol{x}_I$, it is now possible to define the interpolation function, by substituting in Equation (3.7) the result from Equation (3.10). The interpolation function $\boldsymbol{\Phi}(\boldsymbol{x}_I) = \{\varphi_1(\boldsymbol{x}_I), \varphi_2(\boldsymbol{x}_I), \dots, \varphi_n(\boldsymbol{x}_I)\}$ for an interest point $\boldsymbol{x}_I$ is then defined by

$$u(\boldsymbol{x}_I) = \{\boldsymbol{R}^T(\boldsymbol{x}_I), \boldsymbol{p}^T(\boldsymbol{x}_I)\}\, \boldsymbol{M}^{-1} \begin{Bmatrix} \boldsymbol{u_S} \\ 0 \end{Bmatrix} = \boldsymbol{\Phi}(\boldsymbol{x}_I) \begin{Bmatrix} \boldsymbol{u_S} \\ 0 \end{Bmatrix} \tag{3.11}$$

In order to compute the partial derivatives of the interpolated field function, it is necessary to obtain the respective RPI shape functions partial derivatives. So, using for the problem 2D that is being studied, the partial derivative of $\boldsymbol{\Phi}(\boldsymbol{x}_I)$ is defined as

$$\boldsymbol{\Phi}_{,x}(\boldsymbol{x}_I) = \{\boldsymbol{R}^T(\boldsymbol{x}_I) \;\; \boldsymbol{p}^T(\boldsymbol{x}_I)\}_{,x}\, \boldsymbol{M}^{-1} \tag{3.12}$$

$$\boldsymbol{\Phi}_{,y}(\boldsymbol{x}_I) = \{\boldsymbol{R}^T(\boldsymbol{x}_I) \;\; \boldsymbol{p}^T(\boldsymbol{x}_I)\}_{,y}\, \boldsymbol{M}^{-1} \tag{3.13}$$

The first order partial derivative of the RBF vector with respect to the same 2D problem is defined as

$$\boldsymbol{R}(\boldsymbol{x}_I)_{,x} = \left\{\boldsymbol{R}_1(\boldsymbol{x}_I)_{,x} \;\; \boldsymbol{R}_2(\boldsymbol{x}_I)_{,x} \;\; \cdots \;\; \boldsymbol{R}_n(\boldsymbol{x}_I)_{,x}\right\}^T = \left\{\frac{\partial \boldsymbol{R}_1(\boldsymbol{x}_I)}{\partial x} \;\; \frac{\partial \boldsymbol{R}_2(\boldsymbol{x}_I)}{\partial x} \;\; \cdots \;\; \frac{\partial \boldsymbol{R}_n(\boldsymbol{x}_I)}{\partial x}\right\}^T \tag{3.14}$$

$$\boldsymbol{R}(\boldsymbol{x}_I)_{,y} = \left\{\boldsymbol{R}_1(\boldsymbol{x}_I)_{,y} \;\; \boldsymbol{R}_2(\boldsymbol{x}_I)_{,y} \;\; \cdots \;\; \boldsymbol{R}_n(\boldsymbol{x}_I)_{,y}\right\}^T = \left\{\frac{\partial \boldsymbol{R}_1(\boldsymbol{x}_I)}{\partial y} \;\; \frac{\partial \boldsymbol{R}_2(\boldsymbol{x}_I)}{\partial y} \;\; \cdots \;\; \frac{\partial \boldsymbol{R}_n(\boldsymbol{x}_I)}{\partial y}\right\}^T \tag{3.15}$$

being the partial derivatives of the MQ-RBF obtained with

$$\frac{\partial R_i(\boldsymbol{x}_I)}{\partial x} = -2p(r_{iI}^2 + c^2)^{p-1}(x_i - x_I) \tag{3.16}$$

$$\frac{\partial R_i(\boldsymbol{x}_I)}{\partial y} = -2p(r_{iI}^2 + c^2)^{p-1}(y_i - y_I) \tag{3.17}$$

Chapter 4

Solid Mechanics

The continuum mechanics is the foundation of the nonlinear numerical analysis. It is known that solids and structures subjected to loads or forces become stressed. These stresses lead to strains, which can be interpreted as deformations or relative displacements [12].

Since load plays an important role in bone remodeling, in this chapter, the concepts of strain and stress are introduced, followed by an explanation of the equilibrium and the constitutive equations used.

4.1 - Fundamentals

The study of Solid Mechanics is mainly devoted on the relationships between stress and strain and strain and displacements, for a given solid and boundary conditions (external forces and displacements constrains) [82], [83]. So, when analyzing a deformation, the consequent change in the body configuration is defined by the stress and the strain terms. This way, the virtual work can be expressed as an integral over the known body volume. It is important to guarantee that both strain tensor and stress tensor are referred to the same deformed state. To represent the stresses of the current configuration, the symmetric Cauchy stress tensor, $\boldsymbol{\Lambda}$, can be defined

$$\boldsymbol{\Lambda} = \begin{bmatrix} \sigma_{xx} & \sigma_{xy} \\ \sigma_{yx} & \sigma_{yy} \end{bmatrix} \tag{4.1}$$

This work, uses the Voigt notation, expressing tensors in column vectors. Therefore, stress tensor $\boldsymbol{\Lambda}$ is reduced to the stress vector $\boldsymbol{\sigma}$,

$$\boldsymbol{\sigma} = \left\{ \sigma_{xx}\ \sigma_{yy}\ \sigma_{xy} \right\}^T \tag{4.2}$$

and the strain tensor $\boldsymbol{E}$ to the strain vector $\boldsymbol{\varepsilon}$,

$$\boldsymbol{\varepsilon} = \left\{ \varepsilon_{xx}\ \varepsilon_{yy}\ \varepsilon_{xy} \right\}^T \tag{4.3}$$

Solids can show different behaviors, depending on the solid material. In this work only linear elastic isotropic materials are considered. Isotropic materials can be fully described by only two independent material properties, the Young modulus, E, and the Poisson ratio, ν. Thus, the relation between stress and strain in the solid domain is given by the constitutive equation, known as Hooke's Law

$$\boldsymbol{\sigma} = \boldsymbol{c}\boldsymbol{\varepsilon} \tag{4.4}$$

in which, $\boldsymbol{c}$ is the constitutive matrix, given by $\boldsymbol{c} = \boldsymbol{s}^{-1}$, being the matrix $\boldsymbol{s}$ the compliance elasticity matrix. For a general anisotropic material case and considering a plane stress formulation, matrix $\boldsymbol{s}$ is given by

$$\boldsymbol{s}_{\substack{plane\\stress}} = \begin{bmatrix} \frac{1}{E_{11}} & -\frac{\upsilon_{21}}{E_{22}} & 0 \\ -\frac{\upsilon_{12}}{E_{11}} & \frac{1}{E_{22}} & 0 \\ 0 & 0 & \frac{1}{G_{12}} \end{bmatrix} \tag{4.5}$$

while, when considering a plane strain formulation, matrix $\boldsymbol{s}$ is given by

$$\boldsymbol{s}_{\substack{plane\\strain}} = \begin{bmatrix} \frac{1-\nu_{31}\nu_{13}}{E_{11}} & -\frac{\upsilon_{12}+\nu_{31}\nu_{23}}{E_{22}} & 0 \\ -\frac{\upsilon_{12}+\nu_{32}\nu_{13}}{E_{11}} & \frac{1-\nu_{32}\nu_{23}}{E_{22}} & 0 \\ 0 & 0 & \frac{1}{G_{12}} \end{bmatrix} \tag{4.6}$$

being E_{ij} the elasticity modulus, ν_{ij} the material Poisson coefficient and G_{ij} the distortion modulus in material direction i and j.

Obtaining the constitutive matrix $\boldsymbol{c}$, it is possible to align it with a new material referential $Ox'y'$ defined by the versors $\boldsymbol{i} = \{i'_x, i'_y\}$ and $\boldsymbol{j} = \{j'_x, j'_y\}$, using the following expression

$$\boldsymbol{c}' = \boldsymbol{T}^T \boldsymbol{c}\, \boldsymbol{T} \tag{4.7}$$

being $\boldsymbol{T}$ the transformation matrix given by

$$\boldsymbol{T} = \begin{bmatrix} \cos^2\alpha & \operatorname{sen}^2\alpha & -\sin 2\alpha \\ \operatorname{sen}^2\alpha & \cos^2\alpha & \sin 2\alpha \\ \sin\alpha\cdot\cos\alpha & -\sin\alpha\cdot\cos\alpha & \cos^2\alpha\cdot\operatorname{sen}^2\alpha \end{bmatrix} \tag{4.8}$$

where the angle α is the angle between the original material axis Ox and the new material axis Ox':$\alpha = \cos^{-1}(\boldsymbol{i}, \boldsymbol{i}')$.

Now, considering the displacement field given by $\boldsymbol{u} = \{u, v, w\}$, strain components are expressed as

$$\varepsilon_{xx} = \frac{\partial u}{\partial x} \tag{4.9}$$

$$\varepsilon_{yy} = \frac{\partial v}{\partial y}$$

$$\varepsilon_{xy} = \frac{\partial u}{\partial y} + \frac{\partial v}{\partial x}$$

Thus, the strain vector can be defined by the combination of a differential operator and the displacement field, $\boldsymbol{u}$,

$$\boldsymbol{\varepsilon} = \boldsymbol{L}\boldsymbol{u} \tag{4.10}$$

where $\boldsymbol{L}$ is given by

$$\boldsymbol{L} = \begin{bmatrix} \frac{\partial}{\partial x} & 0 & \frac{\partial}{\partial y} \\ 0 & \frac{\partial}{\partial y} & \frac{\partial}{\partial x} \end{bmatrix}^T \tag{4.11}$$

4.2 - Weak Form

The strong form system equations are the partial differential system equations governing the studied physic phenomenon. Using this formulation, the exact solution is always obtained. However this is usually an extremely difficult task in complex practical engineering problems.

On the other hand, formulations based on weak forms give a discretized system of equations but with a weaker consistency on the adopted approximation (or interpolation) functions. This formulation is able to produce stable algebraic system equations and more accurate results [12].

4.2.1 - Galerkin Weak Form

In this work, the discrete equation system is obtained using the Galerkin weak form, which is a variational method based on energy minimization.

So, considering a body described by the domain $\Omega \in \mathbb{R}^2$ and bounded by Γ, where $\Gamma \in \Omega: \Gamma_u \cup \Gamma_t = \Gamma \wedge \Gamma_u \cap \Gamma_t = \emptyset$, being Γ_u the essential boundary and Γ_t the natural boundary, the equilibrium equations governing the linear elastostatic problem are defined as

$$\nabla \boldsymbol{\Lambda} + \boldsymbol{b} = 0 \tag{4.12}$$

in which ∇ is the divergence operator, $\boldsymbol{b}$ the body force per unit volume and $\boldsymbol{\Lambda}$ the Cauchy stress tensor, as defined previously. The natural boundary respect the condition $\boldsymbol{\Lambda}\,\boldsymbol{n} = \bar{\boldsymbol{t}}$ on Γ_t, being $\boldsymbol{n}$ the unit outward normal to the boundary of domain Ω and $\bar{\boldsymbol{t}}$ the traction on the natural boundary Γ_t. The essential boundary condition is $\boldsymbol{u} = \bar{\boldsymbol{u}}$ on Γ_u, in which $\bar{\boldsymbol{u}}$ is the prescribed displacement on the essential boundary Γ_u.

According to the Galerkin Weak form, the real solution is the one that minimizes the Lagrangian functional, L, given by

$$L = T - U + W_f \tag{4.13}$$

being T the kinetic energy, U is the strain energy and W_f is the work produced by the external forces.

The kinetic energy is defined by

$$T = \frac{1}{2}\int_{\Omega} \rho \dot{\boldsymbol{u}}^T \dot{\boldsymbol{u}} \; d\Omega \tag{4.14}$$

where the solid volume is defined by Ω, $\dot{\boldsymbol{u}}$ is the displacement first derivative with respect to time and $\boldsymbol{\rho}$ is the solid mass density.

The strain energy, for elastic materials, is defined as

$$U = \frac{1}{2}\int_{\Omega} \boldsymbol{\varepsilon}^T \boldsymbol{\sigma} \; d\Omega \tag{4.15}$$

being $\boldsymbol{\varepsilon}$ the strain vector and $\boldsymbol{\sigma}$ the stress vector.

The work produced by the external forces can be expressed as

$$W_f = \int_{\Omega} \boldsymbol{u}^T \boldsymbol{b} \; d\Omega + \int_{\Gamma_t} \boldsymbol{u}^T \bar{\boldsymbol{t}} \; d\Gamma_t \tag{4.16}$$

in which $\boldsymbol{u}$ represents the displacement, $\boldsymbol{b}$ the body forces and Γ_t the traction boundary where the external forces $\bar{t}$ are applied.

Therefore the Galerkin weak form can be represented as

$$L = \frac{1}{2}\int_{\Omega} \rho \dot{\boldsymbol{u}}^T \dot{\boldsymbol{u}} \; d\Omega - \frac{1}{2}\int_{\Omega} \boldsymbol{\varepsilon}^T \boldsymbol{\sigma} \; d\Omega + \int_{\Omega} \boldsymbol{u}^T \boldsymbol{b} \; d\Omega + \int_{\Gamma_t} \boldsymbol{u}^T \bar{\boldsymbol{t}} \; d\Gamma_t \tag{4.17}$$

Minimizing the functional and neglecting the dynamic part (kinetic energy variation),since only static problems were considered, the following can be obtained:

$$\delta \int_{t_1}^{t_2} \left[-\frac{1}{2}\int_{\Omega} \boldsymbol{\varepsilon}^T \boldsymbol{\sigma} \; d\Omega + \int_{\Omega} \boldsymbol{u}^T \boldsymbol{b} \; d\Omega + \int_{\Gamma_t} \boldsymbol{u}^T \bar{\boldsymbol{t}} \; d\Gamma_t \right] dt = 0 \tag{4.18}$$

Moving the variation operator δ inside the integrals,

$$\int_{t_1}^{t_2} \left[-\frac{1}{2}\int_{\Omega} \delta(\boldsymbol{\varepsilon}^T \boldsymbol{\sigma}) \; d\Omega + \int_{\Omega} \delta \boldsymbol{u}^T \boldsymbol{b} \; d\Omega + \int_{\Gamma_t} \delta \boldsymbol{u}^T \bar{\boldsymbol{t}} \; d\Gamma_t \right] dt = 0 \tag{4.19}$$

The integrand function in the first integral term can be written as

$$\delta(\boldsymbol{\varepsilon}^T \boldsymbol{\sigma}) = \delta \boldsymbol{\varepsilon}^T \boldsymbol{\sigma} + \boldsymbol{\varepsilon}^T \delta \boldsymbol{\sigma} \tag{4.20}$$

in which $\boldsymbol{\varepsilon}^T \delta \boldsymbol{\sigma} = (\boldsymbol{\varepsilon}^T \delta \boldsymbol{\sigma})^T = \delta \boldsymbol{\sigma}^T \boldsymbol{\varepsilon}$. Using the constitutive equation $\boldsymbol{\sigma} = \boldsymbol{c}\boldsymbol{\varepsilon}$ and the symmetric property of the material matrix, $\boldsymbol{c}^T = \boldsymbol{c}$, it is possible to write

$$\delta\boldsymbol{\sigma}^T\boldsymbol{\varepsilon} = \delta(\boldsymbol{c\varepsilon})^T\boldsymbol{\varepsilon} = \delta\boldsymbol{\varepsilon}^T\boldsymbol{c}^T\boldsymbol{\varepsilon} = \delta\boldsymbol{\varepsilon}^T\boldsymbol{c\varepsilon} = \delta\boldsymbol{\varepsilon}^T\boldsymbol{\sigma} \tag{4.21}$$

Consequently, Equation (4.20) becomes

$$\delta(\boldsymbol{\varepsilon}^T\boldsymbol{\sigma}) = 2\delta\boldsymbol{\varepsilon}^T\boldsymbol{\sigma} \tag{4.22}$$

Retaking Equation (4.19), it can be expressed as

$$-\int_\Omega \delta\boldsymbol{\varepsilon}^T\boldsymbol{\sigma}\ d\Omega + \int_\Omega \delta\boldsymbol{u}^T\boldsymbol{b}\ d\Omega + \int_{\Gamma_t} \delta\boldsymbol{u}^T\bar{\boldsymbol{t}}\ d\Gamma_t = 0 \tag{4.23}$$

Considering the stress-strain relation, $\boldsymbol{\sigma} = \boldsymbol{c\varepsilon}$, and the strain-displacement relation, $\boldsymbol{\varepsilon} = \boldsymbol{Lu}$, Equation (4.23) can be rearranged into the following expression:

$$\int_\Omega (\delta\boldsymbol{Lu})^T\boldsymbol{c}(\boldsymbol{Lu})\ d\Omega - \int_\Omega \delta\boldsymbol{u}^T\boldsymbol{b}\ d\Omega - \int_{\Gamma_t} \delta\boldsymbol{u}^T\bar{\boldsymbol{t}}\ d\Gamma_t \tag{4.24}$$

4.3 - Discrete Equation System

According to the principle of virtual work used in meshless methods, the discrete equations are obtained using meshless shape functions as trial and test functions. Thus, recalling Equation (3.11), the virtual displacements, or the test functions, can be defined as

$$\delta\boldsymbol{u}(\boldsymbol{x}_I) = \delta\boldsymbol{u}_I = \boldsymbol{I}\begin{Bmatrix}\boldsymbol{\Phi}_I\\ \boldsymbol{\Phi}_I\end{Bmatrix}\boldsymbol{u}_s = \begin{bmatrix}\varphi_1(\boldsymbol{x}_I) & 0 & \cdots & \varphi_n(\boldsymbol{x}_I) & 0\\ 0 & \varphi_1(\boldsymbol{x}_I) & \cdots & 0 & \varphi_n(\boldsymbol{x}_I)\end{bmatrix}\begin{Bmatrix}\delta u_1\\ \delta v_1\\ \vdots\\ \delta u_n\\ \delta v_n\end{Bmatrix} = \boldsymbol{H}_I\delta\boldsymbol{u}_s \tag{4.25}$$

being $\boldsymbol{I}$ a 2x2 identity matrix and $\boldsymbol{u}_i = \{u_i, v_i\}$, having two degrees of freedom, since it is being a considered a 2D problem.

So, simplifying the first term of Equation (4.24),

$$\int_\Omega (\delta\boldsymbol{Lu})^T\boldsymbol{c}(\boldsymbol{Lu})\ d\Omega = \int_\Omega (\boldsymbol{LH}_I\delta\boldsymbol{u}_s)^T\boldsymbol{c}(\boldsymbol{LH}_I\boldsymbol{u}_s)\ d\Omega = \int_\Omega \delta\boldsymbol{u}_s\boldsymbol{B}_I{}^T\boldsymbol{c}\boldsymbol{B}_I\boldsymbol{u}_s\ d\Omega = \delta\boldsymbol{u}^T\int_\Omega \boldsymbol{B}_I{}^T\boldsymbol{c}\boldsymbol{B}_I\ d\Omega\boldsymbol{u} \tag{4.26}$$

in which the deformability matrix $\boldsymbol{B}_I$ for the n nodes constituting the influence-cell of interest point $\boldsymbol{x}_I$, can be defined as

$$B_i = \left[\begin{array}{cc:cc:c:cc}\frac{\partial\varphi_1(\boldsymbol{x}_I)}{\partial x} & 0 & \frac{\partial\varphi_2(\boldsymbol{x}_I)}{\partial x} & 0 & \cdots & \frac{\partial\varphi_n(\boldsymbol{x}_I)}{\partial x} & 0\\ 0 & \frac{\partial\varphi_1(\boldsymbol{x}_I)}{\partial y} & 0 & \frac{\partial\varphi_2(\boldsymbol{x}_I)}{\partial y} & \cdots & 0 & \frac{\partial\varphi_n(\boldsymbol{x}_I)}{\partial y}\\ \frac{\partial\varphi_1(\boldsymbol{x}_I)}{\partial y} & \frac{\partial\varphi_1(\boldsymbol{x}_I)}{\partial x} & \frac{\partial\varphi_2(\boldsymbol{x}_I)}{\partial y} & \frac{\partial\varphi_2(\boldsymbol{x}_I)}{\partial x} & \cdots & \frac{\partial\varphi_n(\boldsymbol{x}_I)}{\partial y} & \frac{\partial\varphi_n(\boldsymbol{x}_I)}{\partial x}\end{array}\right] \tag{4.27}$$

In an analogous way, the second and third terms of Equation (4.24) can be also simplified, obtaining the following

$$\int_{\Omega} \delta \boldsymbol{u}^T \boldsymbol{b} \; d\Omega = \int_{\Omega} (\boldsymbol{H}_I \delta \boldsymbol{u}_s)^T \boldsymbol{b} \; d\Omega = \delta \boldsymbol{u}_s{}^T \int_{\Omega} \boldsymbol{H}_I{}^T \boldsymbol{b} \, d\Omega \tag{4.28}$$

$$\int_{\boldsymbol{\Gamma_t}} \boldsymbol{\delta u^T \bar{t}} \; \boldsymbol{d\Gamma_t} = \int_{\boldsymbol{\Gamma_t}} (\boldsymbol{H_I \delta u_S})^T \, \bar{\boldsymbol{t}} \, \boldsymbol{d\Gamma_t} = \boldsymbol{\delta u_S}^T \int_{\boldsymbol{\Gamma_t}} \boldsymbol{H_I}^T \, \bar{\boldsymbol{t}} \, \boldsymbol{d\Gamma_t} \tag{4.29}$$

Thus, Equation (4.24) can become the following

$$\delta L = \delta \boldsymbol{u}^T \underbrace{\int_{\Omega} \boldsymbol{B_I}^T \boldsymbol{c} \boldsymbol{B_I} \, d\Omega \boldsymbol{u}}_{\boldsymbol{K}} - \delta \boldsymbol{u}_s{}^T \underbrace{\int_{\Omega} \boldsymbol{H_I}^T \boldsymbol{b} \, d\Omega}_{\boldsymbol{f_b}} - \boldsymbol{\delta} u_{\boldsymbol{S}}{}^T \underbrace{\int_{\boldsymbol{\Gamma_t}} H_I{}^T \, \bar{t} \, d\Gamma_t}_{\boldsymbol{f_t}} = 0 \tag{4.30}$$

The equilibrium equation is then obtained and defined as

$$\boldsymbol{K} \, \boldsymbol{u} = \boldsymbol{f}_b + \boldsymbol{f}_t \tag{4.31}$$

being $\boldsymbol{K}$, the stiffness matrix, $\boldsymbol{u}$, the displacement field, $\boldsymbol{f}_b$, the body weight vector and $\boldsymbol{f}_t$, the external forces vector. So, considering the vector $\boldsymbol{f} = \boldsymbol{f}_b + \boldsymbol{f}_t$ as the sum vector of the forces applied, it is possible to, using Equation (4.31), solve the linear equation system $\boldsymbol{u} = \boldsymbol{K}^{-1} \boldsymbol{f}$ and obtain the displacement field.

Thenceforward, it is possible to determine numerous variable fields. The strain $\boldsymbol{\varepsilon}(\boldsymbol{x}_I)$, in an interest point $\boldsymbol{x}_I \in \Omega$ can be obtained using Equation (4.10).Then, using the Hooke's Law present in Equation (4.4), the stress field, $\boldsymbol{\sigma}(\boldsymbol{x}_I)$ can be also obtained.

Considering both the strain and the stress fields, the SED field for an interest point $\boldsymbol{x}_I$ and a specific load case can be determined as

$$U(\boldsymbol{x}_I) = \frac{1}{2} \int_{\Omega_I} \boldsymbol{\sigma}(\boldsymbol{x}_I)^T \boldsymbol{\varepsilon}(\boldsymbol{x}_I) \, d\Omega_I \tag{4.32}$$

The principal stresses $\sigma(\boldsymbol{x}_I)$ for the interest point $\boldsymbol{x}_I$ are obtained from the Cauchy stress tensor $\Lambda(\boldsymbol{x}_I)$ using the expression

$$det\left(\begin{bmatrix} \sigma_{xx}(\boldsymbol{x}_I) & \sigma_{xy}(\boldsymbol{x}_I) \\ \sigma_{xy}(\boldsymbol{x}_I) & \sigma_{yy}(\boldsymbol{x}_I) \end{bmatrix} - \sigma(\boldsymbol{x}_I)_i \begin{bmatrix} 1 & 0 \\ 0 & 1 \end{bmatrix} \right) = 0 \tag{4.33}$$

and the principal directions $\boldsymbol{n}((\boldsymbol{x}_I)_i) = \left\{ n_x((\boldsymbol{x}_I)_i), n_y((\boldsymbol{x}_I)_i) \right\}^T$ are obtained with

$$\left(\begin{bmatrix} \sigma_{xx}(\boldsymbol{x}_I) & \sigma_{xy}(\boldsymbol{x}_I) \\ \sigma_{xy}(\boldsymbol{x}_I) & \sigma_{yy}(\boldsymbol{x}_I) \end{bmatrix} - \sigma(\boldsymbol{x}_I)_i \begin{bmatrix} 1 & 0 \\ 0 & 1 \end{bmatrix} \right) \begin{Bmatrix} n_x(\boldsymbol{x}_I)_i \\ n_y(\boldsymbol{x}_I)_i \end{Bmatrix} = 0 \tag{4.34}$$

The three principal stresses obtained can be used to determine the von Mises effective stress for each interest point $\boldsymbol{x}_I$ with the following expression

$$\bar{\sigma}(\boldsymbol{x}_I) = \sqrt{\frac{1}{2}((\sigma(\boldsymbol{x}_I)_1 - \sigma(\boldsymbol{x}_I)_2)^2 + (\sigma(\boldsymbol{x}_I)_2 - \sigma(\boldsymbol{x}_I)_3)^2 + (\sigma(\boldsymbol{x}_I)_3 - \sigma(\boldsymbol{x}_I)_1)^2)} \tag{4.35}$$

Chapter 5

Mechanical Model

Bone remodeling is a complex phenomenon that implies bone resorption followed by bone formation and many bone disorders, such as osteoporosis, can be ascribed to imbalances during this process [84]. Since the understanding of bone remodeling is continuously developing, a number of researchers have worked on the creation of semi empirical mathematical descriptions of this process to gain a better insight into the nature of bone remodeling [85]. This way, mathematical modelling provides a powerful tool to simulate in silico and predict experimental results.

In this chapter, the bone remodeling algorithm proposed in this work, considering only the mechanical stimulus, is described in detail. To validate the algorithm, a 2D benchmark example is used. In this example, a first phase of tests study the influence of the model nodal discretization and the size of the mesh. Then, using FEMAS, different values of decay rate β and two distinct material laws are tested. Thus, this chapter starts with a brief description of these bone tissue material laws. Afterwards, a numerical simulation of the bone tissue remodeling occurring in the femoral bone is performed, obtaining results in good agreement with the literature.

5.1 - Bone Tissue Material Law

During the years, a spectrum of mathematical models were developed describing bone remodeling caused by mechanical stimuli, known as the Wolff's Law. It is stated that bone tissue progressively modifies its morphology adapting to any new external mechanical stimulus, such as the strain level or the stress level [6], [63]. Several mathematical models of bone remodeling were created along the time and evolved with the development of numerical methods and the increasing knowledge about mechanical properties of the bone tissue [63]. For this reason, early models assumed isotropic bone behavior [86]. Later, based in experimental studies, researchers were able to consider bone orthotropic behavior.

5.1.1 - Lotz's Material Law

One of the first models considering the bone orthotropic behavior was presented by Lotz [87]. Lotz material law not only has distinct formulations for the cortical and trabecular

bone, but also different elasticity modulus and ultimate compressive stress values for the axial and transversal directions [12], [87]. Thus, the bone mechanical properties are approximated with the expressions given by the Table 5.1 and the Equations (5.1) and (5.2), being the only variable the apparent density.

Table 5.1 - Coefficients of Lotz's Law.

Bone	Direction	a_1	a_2	a_3	a_4
Cortical	Axial	2.065E+03	3.090E+00	7.240E+01	1.880E+00
	Transversal	2.314E+03	1.570E+00	3.700E+01	1.510E+00
Trabecular	Axial	1.904E+03	1.640E+00	4.080E+01	1.890E+00
	Transversal	1.157E+03	1.780E+00	2.140E+01	1.370E+00

$$E_i = a_1 \cdot \rho^{a_2} \tag{5.1}$$

$$\sigma_i^c = a_3 \cdot \rho^{a_4} \tag{5.2}$$

being E_i the elasticity modulus and the σ_i^c ultimate compressive stress in direction i, both are expressed in MPa while the apparent density ρ in g/cm^3.

5.1.2 - Belinha's Material Law

Belinha's [12] proposed also a law governing the mechanical behavior of the bone tissue based on Zioupo's work [88]. The experimental work of Zioupos [88] showed that, instead of the two distinct material laws proposed by Lotz [87], the law governing the mechanical behavior of the bone tissue is the same for cortical and trabecular bone. Also, the relation between the elasticity modulus and the medium apparent density is no longer the increasing monotonic function of Lotz but a function with a 'boomerang'-like pattern. With this work, the idea that density is a salient property of bone and plays a crucial role in determining the mechanical properties is reinforced [89].

However, Zioupo only analyzed the bone elasticity modulus in the axial direction [89]. Thus, following Zioupo's work, Belinha [12] proposed the mathematical curves for the elasticity modulus in the transversal direction and the ultimate compression stress in the axial and transversal directions, based on the values suggested by Lotz [87]. This way, it was obtained a bone anisotropic material law that correlates accurately the bone density with the obtained level of stress by means of a mechanical stimulus [89].

The elasticity modulus, E, and the ultimate compressive stress, σ_i^c, approximated by the curves proposed by this law are presented in Equations (5.3), (5.4), (5.5), (5.6) and (5.7), while the coefficients are presented in Table 5.2.

Table 5.2 - Coefficients of Belinha's law.

Coefficient	j = 0	j = 1	j = 2	j =3
a_j	0.000E+00	7.216E+02	8.059E+02	0.000E+00
b_j	-1.770E+05	3.861E+05	-2.798E+05	6.836E+04
c_j	0.000E+00	0.000E+00	2.004E+03	-1.442E+02
d_j	0.000E+00	0.000E+00	2.680E+01	2.035E+01
e_j	0.000E+00	0.000E+00	2.501E+01	1.247E+00

$$E_{axial} = \begin{cases} \sum_{j=0}^{3} a_j \cdot \rho^j & if \quad \rho \leq 1.3\ g/cm^3 \\ \sum_{j=0}^{3} b_j \cdot \rho^j & if \quad \rho > 1.3\ g/cm^3 \end{cases} \tag{5.3}$$

$$E_{trans} = \sum_{j=0}^{3} c_j \cdot \rho^j \tag{5.4}$$

$$\sigma_{axial}^{c} = \sum_{j=0}^{3} d_j \cdot \rho^j \tag{5.5}$$

$$\sigma_{trans}^{c} = \sum_{j=0}^{3} e_j \cdot \rho^j \tag{5.6}$$

being E_i the elasticity modulus and the σ_i^c ultimate compressive stress in direction i, both are expressed in MPa while the apparent density ρ in g/cm^3.

5.2 - Proposed Model

Along the years, several mathematical models describing the process of bone remodeling caused by mechanical stimulus have been proposed. These mathematical formulations present a strong correlation between the bone functional adaptation and the induced stress (or strain), considering bone tissue a local adaptive material [12]. But, experimental research has shown that bone remodelling and functional adaptation are quite complex, making the task of describing in detail these processes very ambitious. However, several researchers have dedicated their studies to this subject, proposing models with the aim of numerically predict the local remodelling reactions observed in experiments through appropriate bone growth laws, such as the ones presented in section 5.1 - .

In the present work, it is considered the remodelling algorithm presented by Belinha and co-workers [12], that consists in an adaptation for meshless methods of Carter's model. Therefore, in this section, this iterative remodelling algorithm is presented. In this work, the bone tissue is assumed as an isotropic material, but this algorithm supports also orthotropic materials.

5.2.1 - Model Description

In this work, the remodeling model proposed uses a bone remodeling nonlinear equation, adapted to work with the three numerical methods studied, namely the FEM, the RPIM and the NNRPIM. This equation is a temporal-spatial functional, $\rho(x,t)\colon \mathbb{R}^{d+1} \mapsto \mathbb{R}$, discretized along the one-dimensional temporal line and the d-dimensional space. Presenting it as a differential equation and minimizing it with respect to time, this equation's expression is given by

$$\frac{\partial \rho(\boldsymbol{x},t)}{\partial t} \cong \frac{\Delta \rho(\boldsymbol{x},t)}{\Delta t} = \frac{(\rho_{model})_{t_{j+1}} - (\rho_{model})_{t_j}}{t_{j+1} - t_j} = 0 \tag{5.8}$$

Any problem being analyzed is discretized in space and time. So, the d-dimensional spatial domain is assumed to be discretized in N nodes:$\boldsymbol{X} = \{\boldsymbol{x}_1, \boldsymbol{x}_2, \dots, \boldsymbol{x}_n\} \in \boldsymbol{\Omega}$, leading to Q interest points: $\boldsymbol{Q} = \{\boldsymbol{x}_1, \boldsymbol{x}_2, \dots, \boldsymbol{x}_Q\} \in \boldsymbol{\Omega}$, being $\boldsymbol{x}_i \in \mathbb{R}^d$ and $\boldsymbol{Q} \cap \boldsymbol{X} = \emptyset$. The temporal domain is discretized in iterative fictitious time steps $t_j \in \mathbb{R}$, with $j \in \mathbb{N}$.

Thus, the medium apparent density for the complete model domain is defined by $(\rho_{model})_{t_j}$ at a fictitious time t_j. Consequently, considering the same iterative step, the apparent density for the complete model domain, ρ_{model}, can be determined with,

$$\rho_{model} = Q^{-1} \sum_{i=1}^{Q} \rho_i \tag{5.9}$$

being ρ_i the infinitesimal apparent density on interest point $\boldsymbol{x}_I$ defined by $\rho_I = g(\sigma_I)$. According to the algorithm proposed by Belinha and co-workers [12], since in this work the behavior's material was assumed isotropic, the value of ρ_I is given according to the ultimate compressive stress in the axial direction, σ^c_{axial}. In this work, instead of considering the σ^c_{axial}, the apparent density is determined according to the von Mises effective stress, $\bar{\sigma}(\boldsymbol{x}_I)$, for each interest point $\boldsymbol{x}_I$. Thus, for Lotz's material law, Equation (5.2) can be re-written as

$$\bar{\sigma}_i = a_3 \cdot \rho^{a_4} \tag{5.10}$$

being the values of coefficients a_3 and a_4 present in Table 5.1 depending on the type of bone i being analyzed. In an analogous way, but this time for Belinha's material law, Equation (5.6) is re-defined as

$$\bar{\sigma} = \sum_{j=0}^{3} d_j \cdot \rho^j \tag{5.11}$$

in which the values of coefficient d_j are present in Table 5.1.

So, according to the material law that is being studied, the infinitesimal apparent density on interest point $\boldsymbol{x}_I$, ρ_I, is obtained by solving the Equations (5.10) and (5.11), in respect to the density ρ_I.

However, the remodeling process does not occur for all interest points, $\boldsymbol{x}_I$. In fact, only the interest points presenting the SED values belonging to the interval indicated in Equation (5.12) are identified and subjected to a density remodelling process, while all the other interest points maintain the previous density.

$$U(\boldsymbol{x}_I) \in [U_m, U_m + \alpha \cdot \Delta U [\cup] U_M - \beta \cdot \Delta U, U_M], \quad \forall\, U(\boldsymbol{x}_I) \in \mathbb{R} \tag{5.12}$$

being $U_m = \min(U)$, $U_M = \max(U)$ and $\Delta U = \mathrm{U}_M - U_m$. The parameters α and β define the growth rate and the decay rate of the apparent density, respectively, and vary according to the problem being analysed. Recalling Equation (5.11), since it is an equation of third order, it returns three different solutions, ρ_1, ρ_2 and ρ_3. Thus, if the interest points belong to the decay apparent density interval, the apparent density on interest point $\boldsymbol{x}_I$ is given by

$\rho_I = \min(\rho_1, \rho_2, \rho_3)$. When the interest points belong to the increase apparent density interval, the apparent density on interest point $\boldsymbol{x}_I$ is given by $\rho_I = \max(\rho_1, \rho_2, \rho_3)$

Lastly, the remodelling equilibrium is achieved when the following condition is achieved

$$\frac{\Delta\rho}{\Delta t} = 0 \vee (\rho_{model})_{t_j} = \rho_{control} \tag{5.13}$$

5.2.2 - Remodeling Procedure

The algorithm implemented in this work is schematized in Figure 5.1. This algorithm is initialized with the pre-processing of the available medical images. Thus, the problem domain is discretized with an unstructured nodal mesh $\boldsymbol{X} \in \boldsymbol{\Omega}$, and a background integration mesh is constructed, according to the numerical method chosen by the user (the FEM, the RPIM or the NNRPIM). Afterwards, the initial material properties are allocated to the respective domain areas and the shape functions for each integration point $\boldsymbol{x}_I$ are constructed, $\varphi(\boldsymbol{x}_I)$, as previously explained in Chapter 3. Also, the essential and natural boundary conditions are imposed.

After this, and in order to initiate the remodelling process, a preliminary elasto-static analysis of the problem is performed to determine the material orientation. This is possible to determine with the use of the principal direction information on each integration point $\boldsymbol{x}_I$, by aligning the material constitutive matrix $\boldsymbol{c}$ with the principal direction $\boldsymbol{n}((\boldsymbol{x}_I)_1)$ of the respective maximum principal stress $\sigma(\boldsymbol{x}_I)_1$.

Only then the iterative algorithm actually begins. Along the iterative process, a mechanical analysis is always performed for each time instant t_j. The local stiffness matrix, $\boldsymbol{K}_I$, for each integration point $\boldsymbol{x}_I$ is defined using the deformation matrix $\boldsymbol{B}_I$ and the constitutive material matrix $\boldsymbol{c}_I$. In the end of this process, all the local stiffness matrices $\boldsymbol{K}_I$ obtained are assembled, obtaining a global stiffness matrix, $\boldsymbol{K}$. Afterwards, since the RPIM and the NNRPIM use the Galerkin weak form, the following equation system is possible to obtain for the three numerical methods: $\boldsymbol{K}\boldsymbol{u} = \boldsymbol{f}$, being the unknown displacement field defined as $\boldsymbol{u}$ and the applied forces vector represented by $\boldsymbol{f}$. Having defined the displacement field, the strain, $\boldsymbol{\varepsilon}$, and the stress, $\boldsymbol{\sigma}$, fields can be also obtained, as described in section 4.3 - . Then, the stress and the strain fields can be used to determine the SED and the von Mises effective stress fields as well as the principal stresses and directions. Since this algorithm permits to consider simultaneously various load cases $\boldsymbol{f}_j^k$, the described process until now is repeated for each load case. In the end, the variable fields obtained for each load case are weighted using the following expression

$$\{\boldsymbol{u}_j, \boldsymbol{\varepsilon}_j, \boldsymbol{\sigma}_j, \boldsymbol{\sigma}(\boldsymbol{n})_j, \boldsymbol{n}_j, \bar{\boldsymbol{\sigma}}_j, \boldsymbol{U}_j\} \sum_{k=1}^{l} \frac{m^{(k)}\{\boldsymbol{u}_j, \boldsymbol{\varepsilon}_j, \boldsymbol{\sigma}_j, \boldsymbol{\sigma}(\boldsymbol{n})_j, \boldsymbol{n}_j, \bar{\boldsymbol{\sigma}}_j, \boldsymbol{U}_j\}}{\sum_{s=1}^{l} m^{(s)}} \tag{5.14}$$

The variables field weighted with Equation (5.14) are: the displacement field, $\boldsymbol{u}_j^k$; the strain field, $\boldsymbol{\varepsilon}_j^k$; the stress field, $\boldsymbol{\sigma}_j^k$; the principal stresses field, $\boldsymbol{\sigma}(\boldsymbol{n})_j^k$; the principal directions field, $\boldsymbol{n}_j^k$; the von Mises effective stress field, $\bar{\boldsymbol{\sigma}}_j$ and the SED field, $\boldsymbol{U}_j^k$. As the expression indicates, the final weighted variable field of step j is obtained with the superposition of the number of relevant discrete load cases, l, weighted according to the corresponding number of load cycles, m.

Each mechanical analysis is followed by the bone tissue remodelling. Thus, the interest points belonging to the interval indicated in Equation (5.12) are identified and subjected to a density remodelling process, while all the other interest points maintain the previous density.

Then, considering the weighted effective stress field, the interest points selected will update their apparent density using the material law chosen by the user (Lotz or Belinha's laws). After establishing the new apparent density, the algorithm moves forward to the next iteration step.

Then, using the new apparent density field, in each interest point, the material properties are updated, using again the equations in section 5.1 - . After, the constitutive elasticity matrix, defined for each interest point, is rotated considering the principal directions obtained in the previous iteration step. This procedure permits to align iteratively the material properties with the actualized load path.

The process stops when the condition present in Equation (5.13) is achieved.

In conclusion, the presented remodelling algorithm is a topology optimization based model for bone adaptation, since only a small fraction of bone material have its density actualized each time. With this approach, the material properties' orientation is continuously optimized. Also, in this algorithm, it is given to the user an important role when choosing the numerical method, since the accuracy of the remodelling algorithm is intimately dependent on the accuracy of the used numerical method [89].

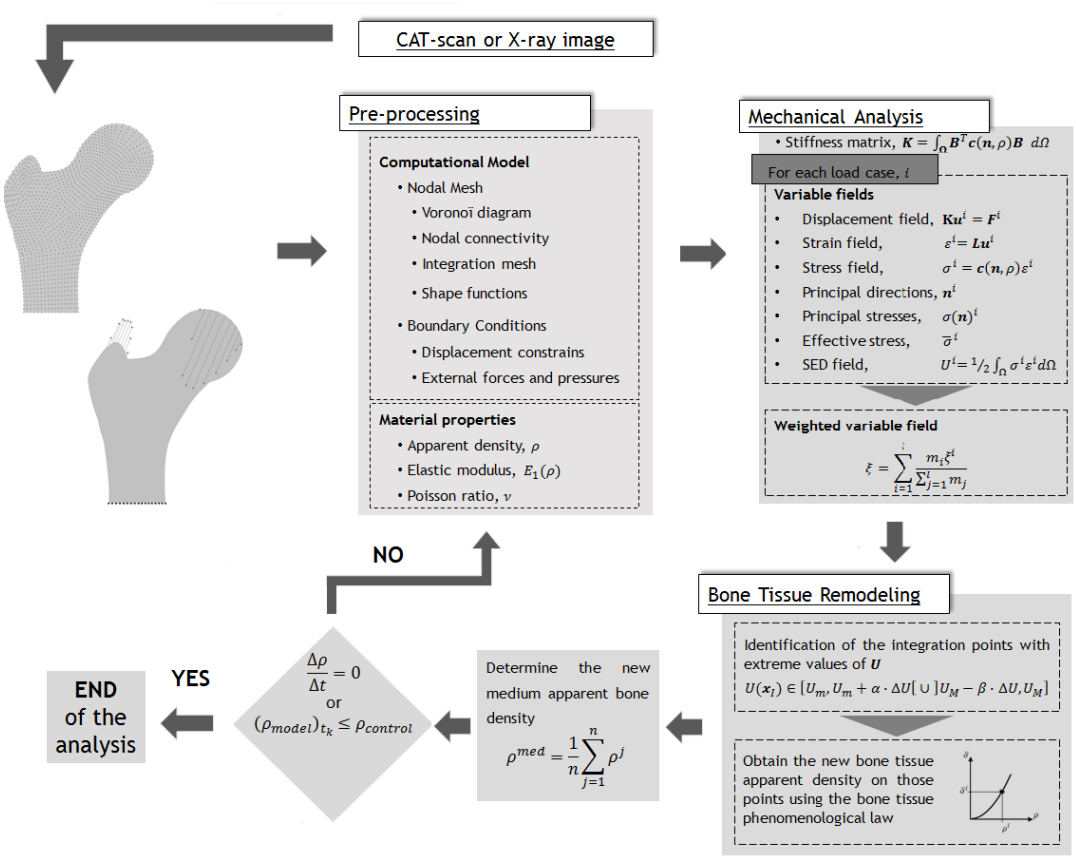

Figure 5.1 - Proposed bone remodeling algorithm for the mechanical model

5.2.3 - Interpretation of the Results

As previously mentioned, the bone tissue remodeling analyses performed in this work use three different numerical methods – the FEM, the RPIM and the NNRPIM.

Considering first the bone tissue analyses performed using the NNRPIM, it is known that the problem domain, $\boldsymbol{\Omega} \in \mathbb{R}^d$, is discretized by a nodal distribution, $\boldsymbol{X} = \{\boldsymbol{x}_1, \boldsymbol{x}_2, \dots, \boldsymbol{x}_n\} \in \boldsymbol{\Omega}$, with $\boldsymbol{x_i} \in \mathbb{R}^{\boldsymbol{d}}$, followed by the construction of the Voronoï diagram, $\boldsymbol{V} = \{\boldsymbol{V}_1, \boldsymbol{V}_2, \dots, \boldsymbol{V}_n\}$, being $\boldsymbol{\Omega} = \cup_{i=1}^{N} \boldsymbol{V}_i$. Then, using the Voronoï diagram, the integration points are determined, $\boldsymbol{Q} = \{\boldsymbol{x}_1, \boldsymbol{x}_2, \dots, \boldsymbol{x}_Q\} \in \boldsymbol{\Omega}$, with $\boldsymbol{q}_j \in \mathbb{R}^d$, as previously described. These integration points are sequentially obtained for each Voronoï cell V_i, leading to the production of k integration points for each Voronoï cell V_i, being $\boldsymbol{Q}_{Vi} = \{\boldsymbol{x}_1, \boldsymbol{x}_2, \dots, \boldsymbol{x}_Q\} \in \mathbf{Q}$ and $\boldsymbol{Q}_{Vi} \subset V_i$, as can be depicted by Figure 5.2a. Each Voronoï cell, V_i, can be divided in infinitesimal subdivisions $\mathrm{A}_{\mathrm{J}}^{\mathrm{V_j}}$, consisting on the smallest dimensional partition of the domain. But, each one of these sub-cells, $\mathrm{A}_{\mathrm{J}}^{\mathrm{V_j}}$, is numerically represented by only the respective integration point, $\boldsymbol{x}_I$. Therefore, it is not possible to obtain the ideal detailed microscale trabecular arrangement represented in Figure 5.2b, in which the bone volume, A_b, and the void volume, A_v, are clearly defined. In fact, it is only possible to obtain the volume porosity,$p(\boldsymbol{x}_J)$, and then the local apparent density, $\rho(\boldsymbol{x}_J) = \rho_0 \left(1 - p(\boldsymbol{x}_J)\right)$, being $\rho_0 = 2.1 g/cm^3$ the compact bone density, Figure 5.2b. To overcome this, the size of the infinitesimal subdivisions could be decreased, increasing the detail of the analysis. However, it would increase also the computational cost of the analysis.

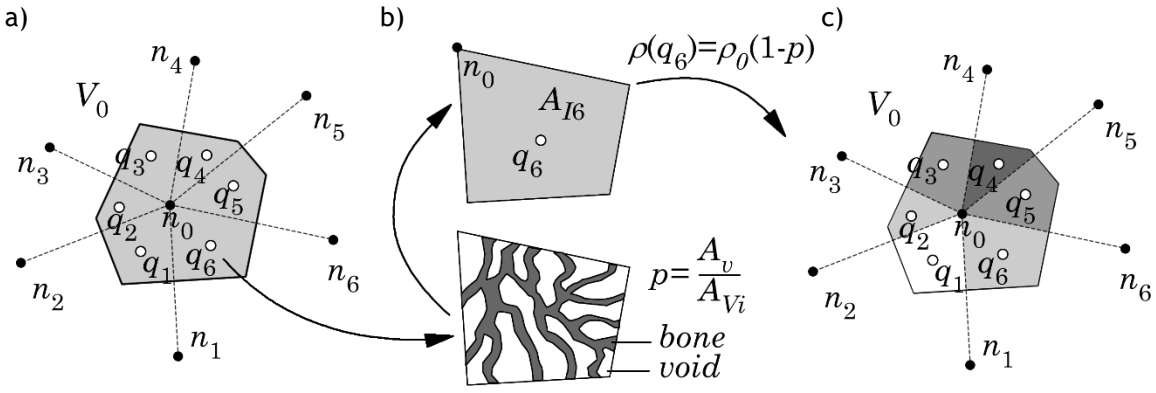

Figure 5.2 - (a) Voronoï cell with the quadrature points. (b) Theoretical trabecular architecture of the sub-cell and homogenized apparent density. (c) Voronoï cell with the integration points homogenized apparent densities [90].

So, instead, it is possible to obtain a local medium apparent density for each Voronoï cell V_i. As represented in Figure 5.2c, each integration point can present a distinct local apparent density, making possible to obtain the local apparent density of each field node $\boldsymbol{x}_i$, using the following expression,

$$\rho(\boldsymbol{x}_i) = \frac{\sum_{J=1}^{k} \widehat{w}_J \cdot \rho(\boldsymbol{x}_J)}{\sum_{J=1}^{k} \widehat{w}_J} \tag{5.15}$$

where $\widehat{w}_J$ is the integration weight of an integration point $\boldsymbol{x}_J$ belonging to the Voronoï cell V_i of the field node $\boldsymbol{x}_i$.

An analogous procedure occurs on the FEM and the RPIM. The difference is that both use the Gauss-Legendre quadrature scheme, instead of the Voronoï diagram. However, in the

end, all methods allow the definition of the local apparent density field, with Equation (5.15), and its representation in isomaps.

Therefore, all the results presented in this work, in all numerical examples, are presented as grey tone isomaps. In those grey tone isomaps, the white color represents the considered maximum apparent density $\rho_0 = 2.1 g/cm^3$ and the dark-grey color represents the minimum apparent density $\rho_0 = 0.1 g/cm^3$ admitted in the analysis. All the other gray tones in the middle represent transitional apparent densities, following a linear color grey-scale gradient. In Figure 5.3, it is presented an isomap example, obtained with the proposed remodeling algorithm combined with the RPIM. The result shows a well-defined trabecular arrangement. However, the presented trabecular arrangement is dependent on the domain discretization. So, if more nodes were used in the analysis, more accurate trabecular architecture would be possible to obtain.

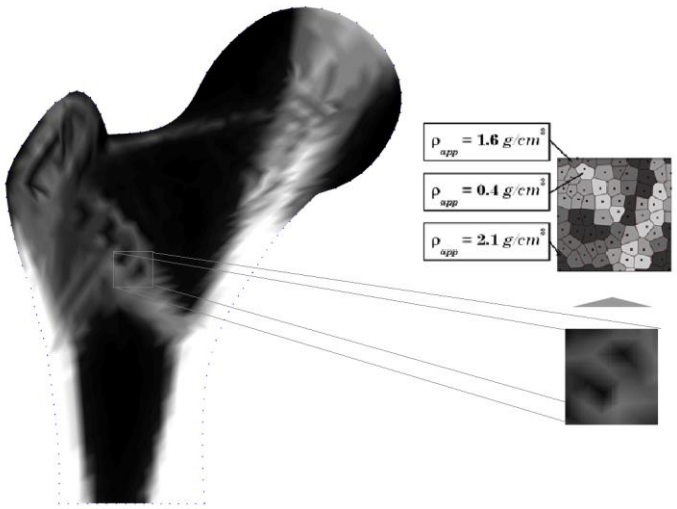

Figure 5.3 - Isomap representing the trabecular architecture of the femoral bone.

5.2.4 - FEMAS

The algorithm described in the previous section is included in the software Finite Element and Meshless Method Analysis Software (FEMAS). FEMAS is a structural analysis software that permits to perform linear and non-linear analysis using the FEM or several meshless methods. FEMAS is implemented in MATLAB and has a graphical user interface (GUI), as can be depicted in Figure 5.4. The software allows a lot of control by permitting the autonomously design of the 2D or 3D numerical model, as well as the location of the essential and natural boundary conditions. The computational framework uses the plane stress and plane strain two-dimensional deformation theory and the three-dimensional deformation theory. Additionally, it allows also the use of both isotropic and anisotropic materials.

The workflow of the bone remodeling analysis performed by FEMAS can be divided in three phases, pre-process, process and post-process. Additionally, FEMAS allows the incorporation of new algorithms and consequent analysis with the numerical methods already integrated in the program. Thus, the new bone remodeling algorithm proposed in this work was first tested using only MATLAB and then added to the routine of bone remodeling already

present in FEMAS. In the end of all processes, the user has easy access to all the data, allowing further data analyses.

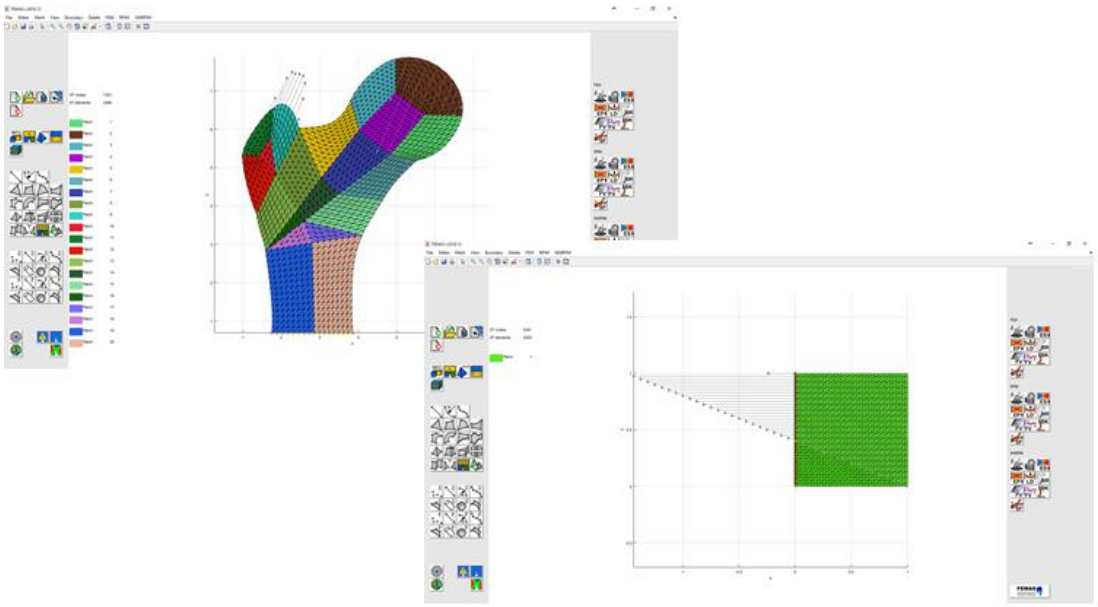

Figure 5.4 - Some screenshots of the FEMAS graphical user interface.

5.3 - 2D Bone Patch Analysis

5.3.1 - Initial Conditions

In the first series of tests, the bone remodeling algorithm was applied to 2D bone micro-patches. The examples ran in FEMAS used the unit square 2D patch present in Figure 5.5a. To validate the bone trabecular remodeling algorithm, it was applied a compressive stress decreasing linearly from the top. The node displacement was constrained in the x direction along the line x = 0 and on the axis' origin in both x and y directions. These natural and essential boundary conditions, as well as the the benchmark model [91] used to compare the results, are present in Figure 5.5b and Figure 5.5c. This benchmark example presents a very specific trabecular morphology existent in long bones. Thus, trabecular bone is typically located at the proximal ends of these types of bones, having an arrangement relatively regular that reflects the direction of the principal mechanical stresses to which this kind of bone is being subjected.

Lastly, in all examples, a uniform apparent density distribution $\rho_{max} = 2.1 g/cm^3$ and Poisson ratio $\upsilon = 0.3$ are assumed, regardless of the material direction. The bone tissue was assumed to be isotropic.

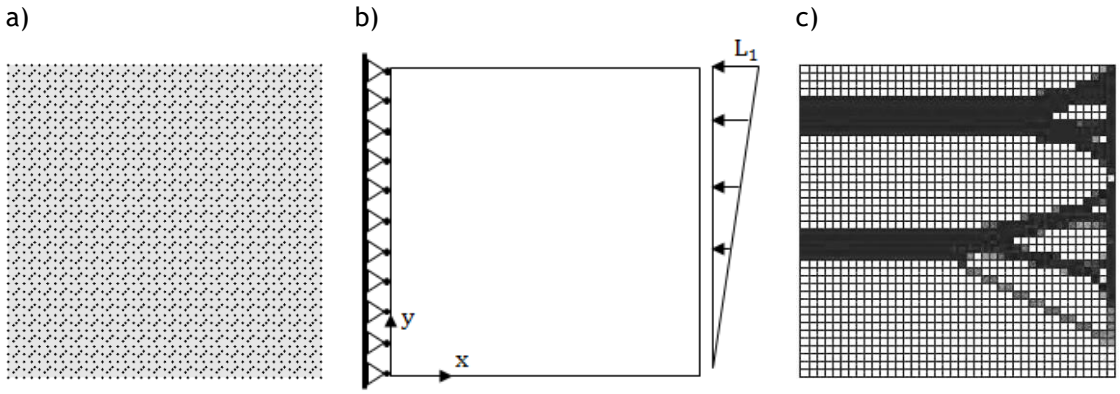

Figure 5.5 - (a) Regular nodal distribution (2 481 nodes). (b) Plate model geometry and essential and natural boundary conditions. (c) Benchmark example [91].

In a first phase, the proposed algorithm was tested using only MATLAB. Using FEM and RPIM, it was studied the influence of the type of mesh used (regular or irregular) and its size, in which the mesh sizes tested were 10x10, 20x20, 30x30 and 40x40 nodes.

After validating the algorithm, the bone remodelling routine integrated in FEMAS was updated. Using now FEMAS, FEM, RPIM and NNRPIM were studied and their results compared. The square patch was analysed considering four distinct β parameters: $\beta = \{0.1, 0.05, 0.02, 0.01\}$, while the parameter α was assumed as $\alpha = 0$.

In Table 5.3Table 5.4, the parameters used in FEMAS are listed.

Table 5.3 - Parameters of the RPIM.

Number of nodes inside the influence domain	16
c	0.0001
p	0.9999
Polynomial Basis	Constant
Gauss Quadrature	2

Table 5.4 - Parameters of the NNRPIM.

Order of the influence-cell	16
c	0.0001
p	0.9999
Polynomial Basis	Constant
Gauss Quadrature	1

5.3.2 - Results and Discussion

The results obtained during the first phase of tests are present in Figure 5.6 andFigure 5.7. Considering the regular and the irregular nodal distributions (Figure 5.6), it is possible to detect a distinct difference between the results. Using a regular mesh, solutions obtained with the FEM and the RPIM are different, but both are capable to reproduce the expected trabecular morphology present in the benchmark example. In respect to results obtained using an irregular mesh, solution obtained with the FEM has lower quality when compared with the RPIM's solution. While the RPIM's solution presents a trabecula individualized in branches, the FEM's solution is not that refined, deviating more from the desired solution. This is due probably to the nodal connectivity imposed on the FEM that led

to a mesh with lower quality, causing a decrease of the accuracy of the numerical method and, consequently, of the final solution.

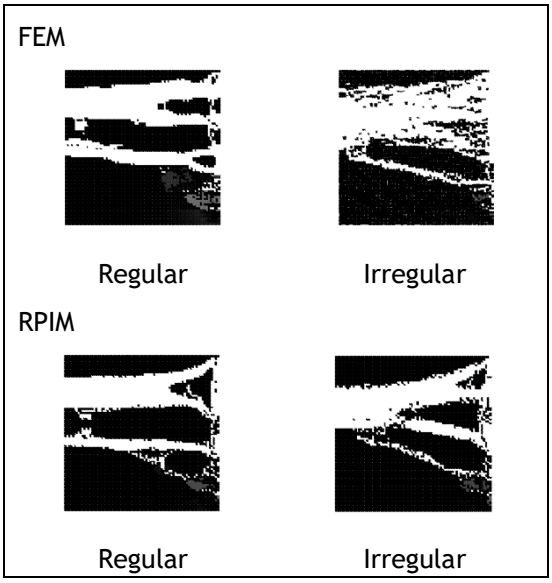

Figure 5.6 - Evolution of the trabecular architecture with different types of mesh obtained using the FEM and the RPIM. The bone law used was Lotz's Law with $\beta = 0.1$.

In respect to Figure 5.7, solutions obtained, using either the FEM or the RPIM, show to be dependent of the mesh refinement. Both the FEM and the RPIM shown to able to produce similar solutions using 40x40 nodes.

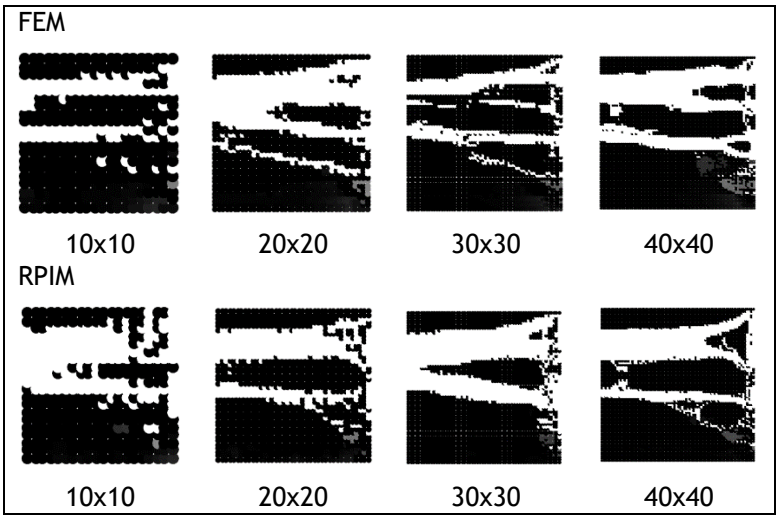

Figure 5.7 - Evolution of the trabecular architecture with increasing mesh sizes obtained using the FEM and the RPIM. The bone law used was Lotz's Law with $\beta = 0.1$.

Thus, based on these results, the algorithm was validated and, consequently, integrated in FEMAS. The following tests were then performed with this software, using the regular mesh present in Figure 5.5.

In Figure 5.8 and Figure 5.9, it is possible to see the results obtained for different values of decay rate β. Although results obtained using Lotz's law and Belinha's law are different,

both were able to reproduce the trabecular morphology. Focusing on the influence of β, as this parameter decreased, more and thinner brunches were formed. This is probably due to the fact that lower values of β, give bone more time to adapt to the loads it is being subjected, leading to a more precise solution. However, this behaviour was only observed on solutions obtained with the FEM for both bone laws and with the RPIM using Belinha's bone law. It is not possible to assign an optimal value for parameter β, since it is dependent on the refinement of the mesh. For coarser meshes, small values of β have to be considered, but if the meshes have nodal distributions very dense, higher values of β might be considered.

When comparing the solutions obtained with the three numerical methods tested, meshless methods, both the RPIM and the NNRPIM, were shown to be capable to originate solutions as good as the ones obtained with the FEM. Additionally, in respect to bone remodelling simulation, it was the first time that the RPIM was tested.

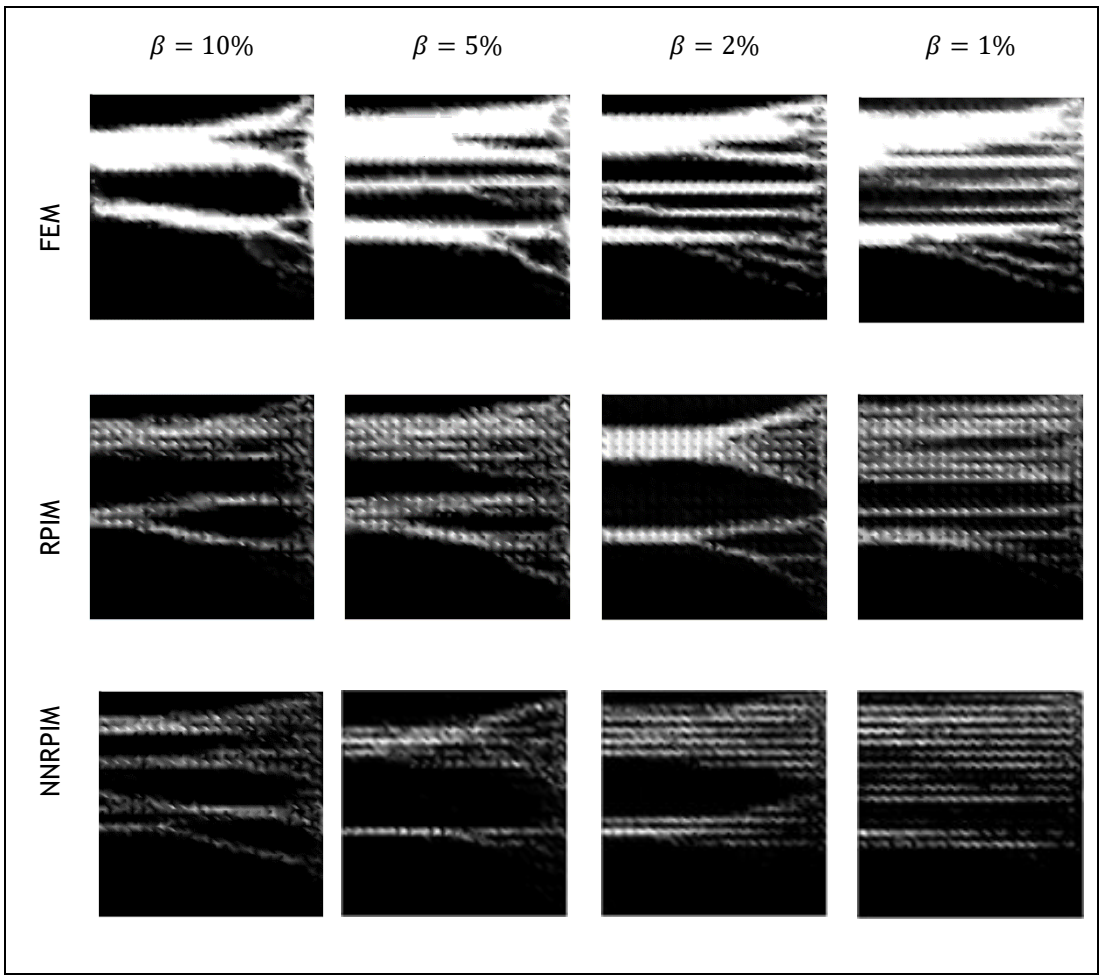

Figure 5.8 – Evolution of the trabecular morphology using Lotz's law

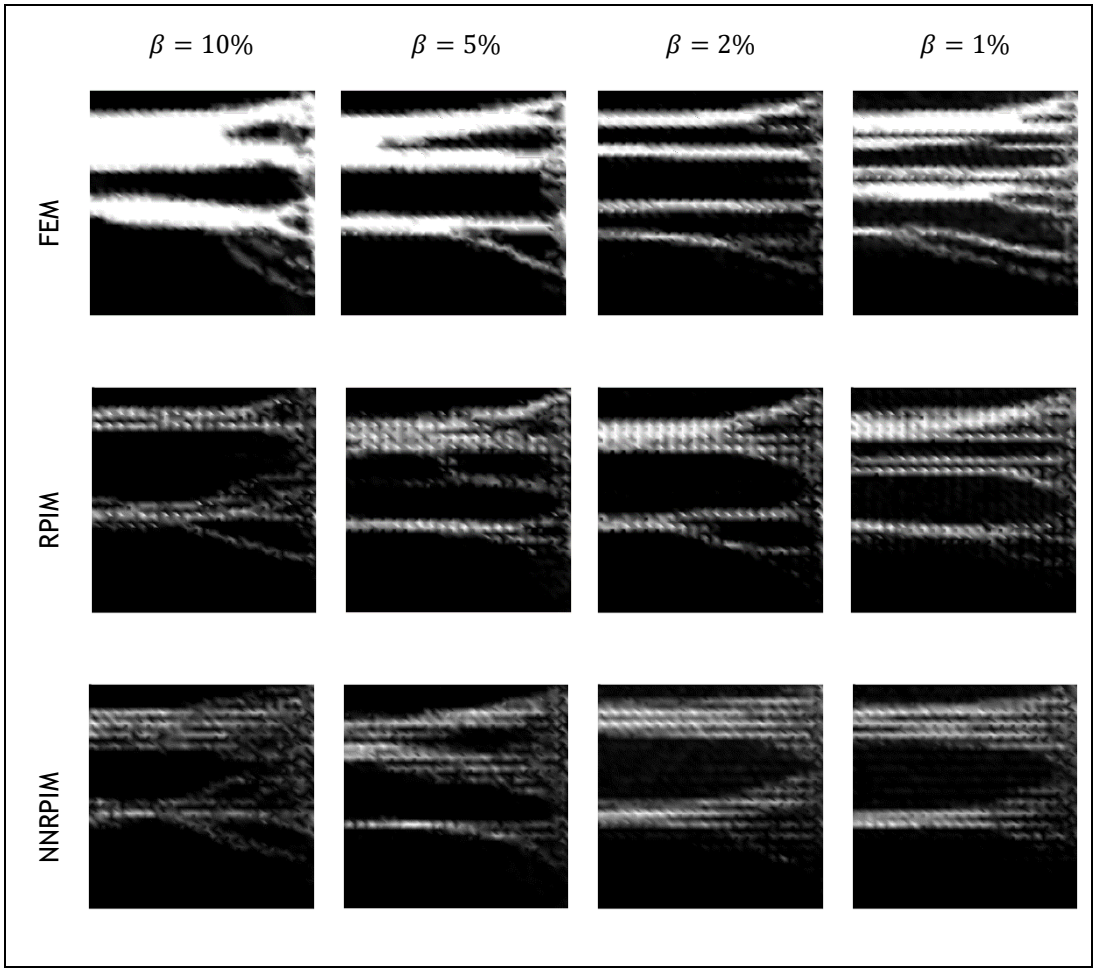

Figure 5.9 - - Evolution of the trabecular morphology using Belinha's law

5.4 - Femoral 2D Analysis

After validating the proposed algorithm using small bone patches, the work moved forward and used this time natural bones. The bone chosen was the femur, since it is a very well-studied bone in biomechanics [92]–[95] and, since it is a long bone, the trabecular structure in the proximal femur is relatively well oriented. Thus, using the femur bone, the objective was to numerically obtain trabecular distributions that were able to resemble the real trabecular architecture. So, the proposed bone remodeling algorithm was combined with the FEM, the RPIM and the NNRPIM, using a 2D approach.

But, to obtain accurate trabecular distributions, important attention has to be given to the geometry of the model and to the essential and natural boundary conditions. The femur is a long bone articulated in the hip-bone, where the body weight is directly applied in the head of this bone, the femur head. Using X-ray images, such as the one presented in Figure 5.10a, it is possible to empirically obtain the principal compressive and tensile lines, as indicated in Figure 5.10b.

Based on these images, Beaupré [92], [93]proposed three-load cases for the femur loading that have been used by several authors. Each one of these loads consist on one parabolic distributed load over the joint surface, nbc_1 and another parabolic distributed load on the

trochanter, nbc_2, representing the abductor muscle attachment. Also, all degrees of freedom are constrained in the basis of the model, ebc_1. In this work, it was only used the first mechanical case, as represented in Figure 5.10c, where it is possible to observe the resultant of each applied parabolic distributed load and the correspondent direction.

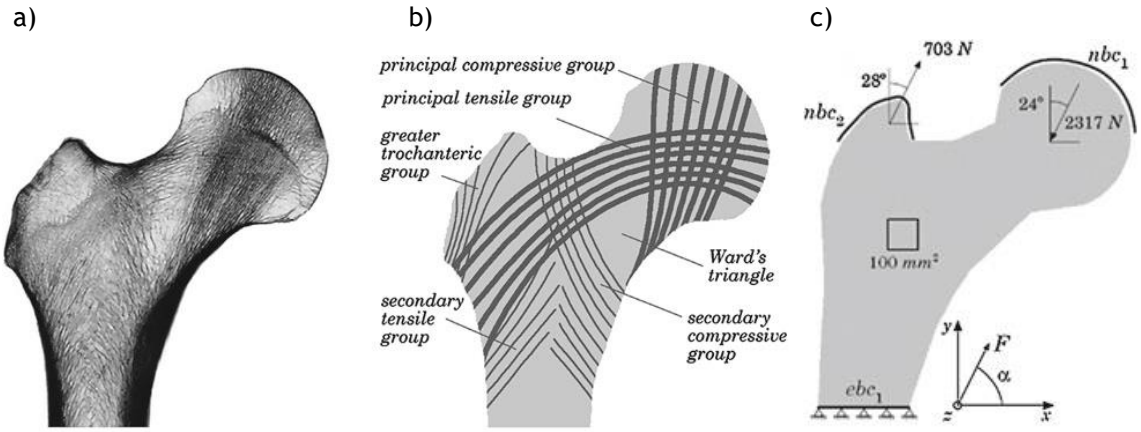

Figure 5.10 – (a) Femoral X-ray plate. (b) Internal principal trabecular structures found in the femur bone. (c) Loads and constrains of the first mechanical case of the femur bone [12].

5.4.1 - Initial Conditions

In order to test if the proposed model was able to reproduce the trabecular distributions existent in the femur bone, the geometry of a 2D proximal femur model was used, discretizing the domain with a nodal distribution, as represented in Figure 5.11a. Considering the first mechanical case proposed by Beaupré, the natural boundary condition applied was two parabolic distributed loads, nbc_1 and nbc_2, and the essential boundary condition imposed was the nodal constraint in the basis of the model, ebc_1 (Figure 5.11b). In Figure 5.11c, it is represented the solution for the first mechanical case obtained by Belinha using the NNRPIM [12]

In all examples, a uniform apparent density distribution $\rho_{max} = 2.1 g/cm^3$ and Poisson ratio $\upsilon = 0.3$ were assumed, regardless of the material direction. The bone tissue was assumed to be isotropic, and the growth and decay rate of bone tissue were assumed as $\alpha = 0.0$ and $\beta = 0.01$. The algorithm was combined with the FEM, the RPIM and the NNRPIM.

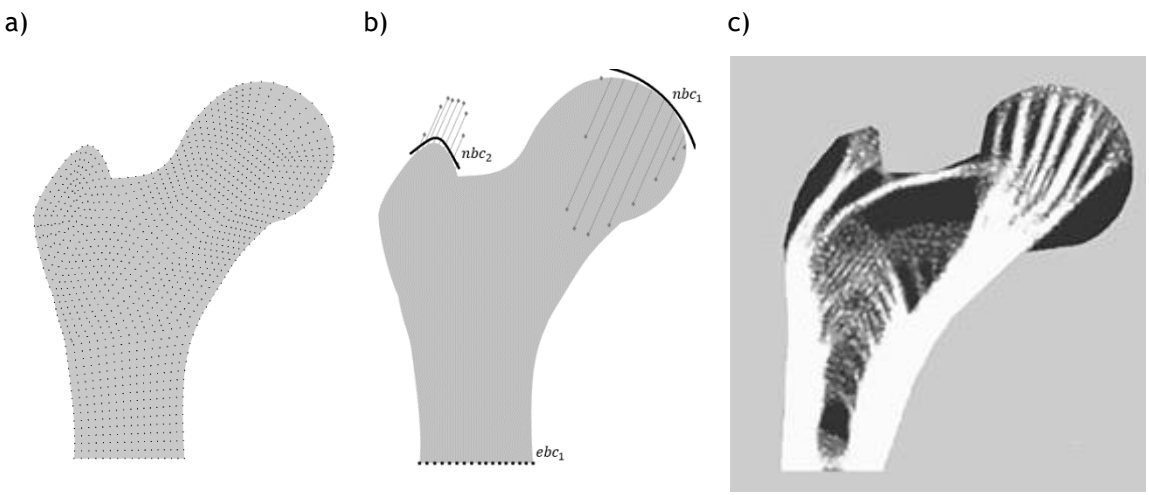

Figure 5.11 – (a) Nodal distribution (1 303 nodes). (b) Model geometry and essential and natural boundary conditions. (c) Example obtained by Belinha [12] with the NNRPIM, using a nodal mesh of 5 991 nodes

5.4.2 - Results and Discussion

The results obtained regarding the first mechanical case proposed by Beaupré are presented in Figures Figure 5.12, **Erro! A origem da referência não foi encontrada.** and **Erro! A origem da referência não foi encontrada.**, in respect to the numerical method used.

In each of these figures, it is presented the von Mises effective stress isomap obtained for the first step of the iterative remodeling analysis, the final von Mises effective stress distribution obtained in the analysis and the final trabecular architecture obtained in the analysis. Also, it is presented the final maximum and minimum principal strains obtained in each analysis.

By analyzing both the final von Mises effective stress isomap and the obtained trabecular architecture, and comparing the results obtained with the FEM, the RPIM and the NNRPIM, it is possible to depict that the solutions differ between them, but all of them were able to form the principal compressive group, indicated in Figure 5.10b. Although in the FEM solution, the principal tensile group was not formed, in the meshless solutions this structure is present, allowing to detect also the Ward's triangle. This suggests that the FEM needed more refined meshes in order to reproduce these structures. However, in all solutions it is possible to detect the presence of the greater trochanteric group. Thus, it is possible to conclude that the remodeling algorithm proposed in this work is capable to reproduce the trabecular distribution observed in the femur bone, producing results coherent with the ones found in the literature. However, the model used for these simulations had a very dispersed nodal distribution, making it impossible to obtain results as precise as the one represented in Figure 5.11c.

So, this work showed that, in order to numerically obtain an accurate trabecular distribution, four components are required: a suitable bone tissue phenomenological law; an efficient iterative remodeling algorithm, an accurate numerical method and a correct numerical model.

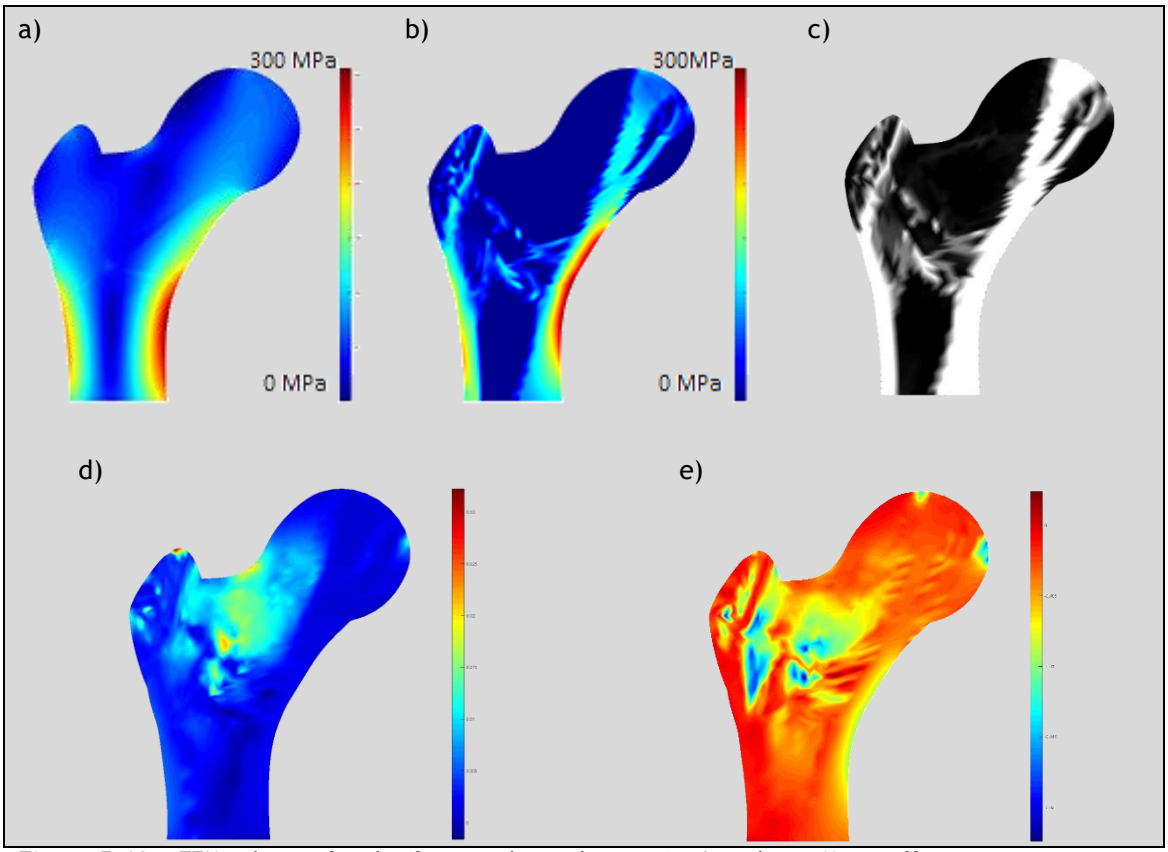

Figure 5.12 - FEM solution for the first mechanical case: (a) Initial von Mises effective stress isomap; (b) Final von Mises effective stress isomap; (c) Final obtained trabecular architecture; (d) Final maximum strain isomap; (e) Final minimum strain isomap.

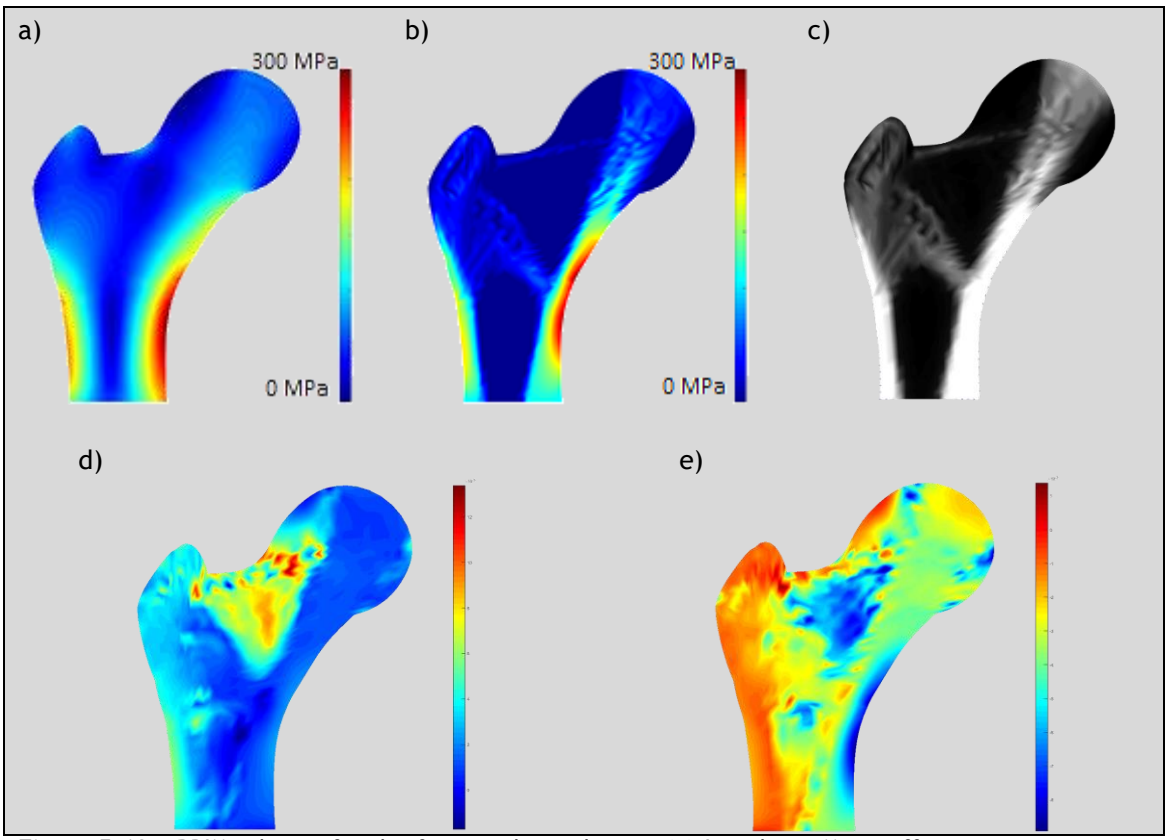

Figure 5.13 - RPIM solution for the first mechanical case: (a) Initial von Mises effective stress isomap; (b) Final von Mises effective stress isomap; (c) Final obtained trabecular architecture; (d) Final maximum strain isomap; (e) Final minimum strain isomap.

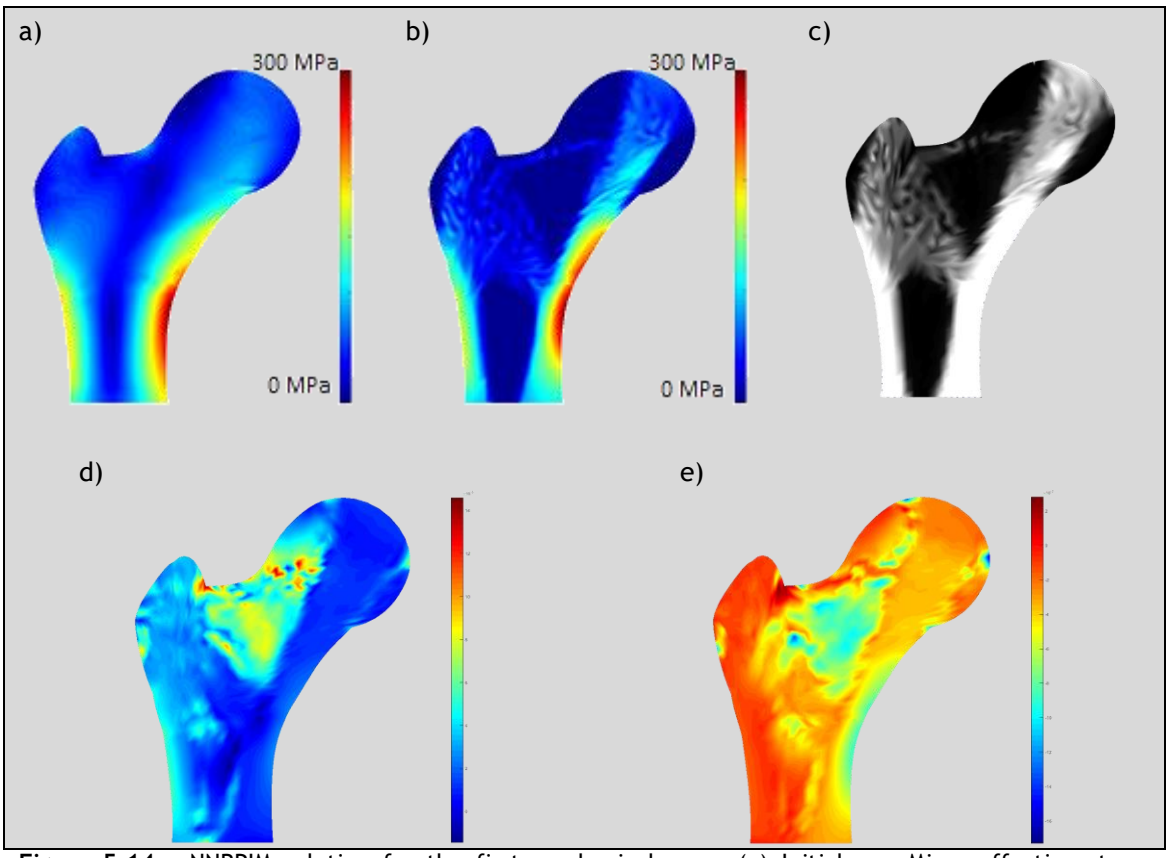

Figure 5.14 - NNRPIM solution for the first mechanical case: (a) Initial von Mises effective stress isomap; (b) Final von Mises effective stress isomap; (c) Final obtained trabecular architecture; (d) Final maximum strain isomap; (e) Final minimum strain isomap.

Chapter 6

Biological Model

Along the years, many mathematical models have been proposed with respect to bone remodelling induced by mechanical stimulus. However, fewer attempts have been made to mathematically reconstruct the process of bone remodelling at the cellular level [96]. By including the current knowledge about bone cell activity, these mathematical models aim to study the cell dynamics and its effects [97].

In this work, a new biological model is proposed, based on the models proposed first by Komarova [96] and later complemented by Ayati [3]. Thus, this chapter starts with a description of these three models. Then, to validate the proposed biological model, a single cycle of bone remodelling was simulated using a 2D bone patch.

6.1 - Komarova's Model

Komarova's approach was to model bone cell population dynamics, examining the osteoclast/osteoblast interactions in BMU's and the microenvironment during bone remodelling [96]. Thus, this model considers some of the various paracrine and autocrine regulatory factors released by bone cells that were already described in Chapter 2. But, instead of including the activities of specific factors, the authors used the power-law formalism developed by M. A. Savageau [98]. So, in this approach, all factors leading to a cell response, such as RANKL, RANK or OPG, are lumped together in a single exponential parameter [96].

It is known that osteoclasts and osteoblasts have the ability to interact with each other via effectors, released or activated by these bone cells. This can be done in an autocrine manner, when it locally affects its cell type of origin, or in a paracrine manner, when it affects the other cell type [96]. Therefore, this model assumes that the concentration of a particular local effector depends on the number of donor cells at any given time. The regulatory factors considered in Komarova's model are listed in Table 6.1 as well as their effect on the dynamics of bone cells populations.

Table 6.1 - Description of the regulatory factors considered in Komarova's model and their respective effect on bone cell dynamics. Identification of the parameter in which each factor is considered in the model's equations.

	Type of Signalling	Factor	Effect	Parameter
OSTEOCLASTS	Autocrine	TGF-β	Stimulation of osteoclasts formation	g_{CC}
	Paracrine	RANKL	Stimulation of osteoclasts formation	g_{BC}
		OPG	Inhibition of osteoclasts formation	g_{BC}
OSTEOBLASTS	Autocrine	IGF	Stimulation of osteoblasts formation	g_{BB}
	Paracrine	TGF-β	Stimulation of osteoblasts formation	g_{CB}
		IGF	Stimulation of osteoblasts formation	g_{CB}

The Figure 6.1 is a schematic representation of the interactions considered in the model.

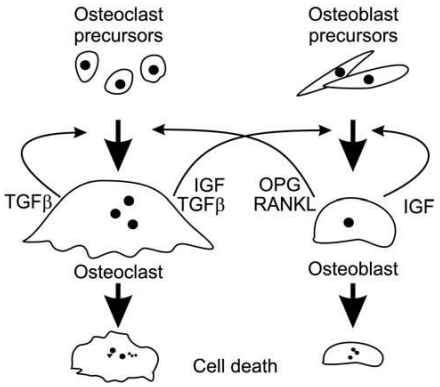

Figure 6.1 - Schematic representation of interactions between osteoclasts and osteoblasts included in Komariva's model [96].

Then, Komarova constructed the following system of differential equations to describe the dynamics of cell populations at a bone remodelling site:

$$\frac{\partial C}{dt} = \alpha_C C^{gCC} B^{gBC} - \beta_C C \tag{6.1}$$

$$\frac{\partial B}{dt} = \alpha_B C^{gCB} B^{gBB} - \beta_B B \tag{6.2}$$

where C and B are the number of osteoclasts and osteoblasts, respectively. Parameter α_i is the rate of overall production of each cell population, i, reflecting the net effect of recruitment of precursors and the formation of mature cells. Parameter β_i defines the rates of cell removal, reflecting cell death, as well as differentiation of osteoblasts into osteocytes and bone lining cells. Finally, parameters g_{ij} represent the net effectiveness of osteoclast- or

osteoblast-derived autocrine or paracrine factors. Therefore, parameter g_{CC} describes the combined effects of all factors produced by osteoclasts that regulate osteoclast formation. Parameter g_{CB} includes the combined effects of all factors produced by osteoclasts that regulate osteoblast formation. Parameter g_{BB} defines the combined effects of all factors produced by osteoblasts that regulate osteoblast formation, while parameter g_{BC} includes the combined effects of all factors produced by osteoblasts that regulate osteoclast formation.

Regarding variation of bone mass, Komarova assumed cell numbers above steady-state levels indicate proliferation and differentiation of precursors into mature cells able to remove or build bone. Therefore, populations of osteoclasts and osteoblasts under steady-state conditions were assumed to consist of differentiated cells that were unable to resorb or build bone, but able to participate in autocrine and paracrine signalling [96]. Thus, the number of cells exceeding steady-state levels is given by $\max[0, C - \bar{C}]$ for osteoclasts and $max[0, B - \bar{B}]$ for osteoblasts. Considering that rates of bone resorption and formation are proportional to the numbers of osteoclasts and osteoblasts, the following Equation (6.3) describes the changes in bone mass,

$$\frac{\partial \rho}{\partial t} = -k_C \max[0, C - \bar{C}] + k_B max[0, B - \bar{B}] \tag{6.3}$$

in which ρ is total bone mass and k_i is normalized activity of bone resorption and formation. The number of cells exceeding steady-state are the number of cells actively resorbing or forming bone.

This model was used to successfully predict different modes of dynamic behavior: a single remodeling cycle in response to an external stimulus, a series of internally regulated cycles of bone remodeling and unstable behavior similar to pathological bone remodeling in Paget's disease [96].

6.2 - Ayati's Model

Few years later, Ayati and co-workers [3] reinterpreted Komarova's model, creating a new diffusion model of bone remodeling. Since Komarova's model was a dynamical system with zero explicit space dimensions, Ayati's presented an updated version of that model and proposed a one-dimensional spatial model. So, in this model, bone mass is given for localized trabecular mass, underneath a point on the surface of the bone.

Thus, it is assumed that both osteoclasts and osteoblasts are diffusing in the spatial domain Ω, according to the following equations

$$\frac{\partial}{\partial t} C(t,x) = \sigma_C \frac{\partial^2}{\partial x^2} C(t,x) + \alpha_C C(t,x)^{\,gCC} B(t,x)^{\,gBC} - \beta_C C(t,x) \tag{6.4}$$

$$\frac{\partial}{\partial t} B(t,x) = \sigma_B \frac{\partial^2}{\partial x^2} B(t,x) + \alpha_B C(t,x)^{\,gCB} B(t,x)^{\,gBB} - \beta_B B(t,x) \tag{6.5}$$

$$\frac{\partial}{\partial t} \rho(t,x) = \sigma_\rho \frac{\partial^2}{\partial x^2} \rho(t,x) - k_C max[0, C(t,x) - \bar{C}(x)] + k_B max[0, B(t,x) - \bar{B}(x)] \tag{6.6}$$

The variables of the model are $C(t,x)$ and $B(t,x)$ that define the density of osteoclasts and osteoblasts, respectively, at time t with respect to $x \in \Omega$. Also, $\rho(t,x)$ reflects the change in bone mass, as a function of x as well as t. Parameters σ_C and σ_B represent the migration of bone stromal cells and σ_ρ represents stochasticity in the bone dynamics.

This mathematical model was applied on normal bone remodeling and dysregulated bone remodeling that occurs in myeloma bone disease.

6.3 - Proposed Model

6.3.1 - Model Description

One of the aims of this work is to simulate, in 2D, the bone remodeling process, regarding the biological response. Thus, the proposed model is based on both Komarova's and Ayati's models, but incorporates an additional spatial variable. This way, changes in osteoblasts and osteoclasts population, as well as in bone mass, are functions of a time variable t and spatial variables x and y.

As in the mechanical model already described, in this model, the bone tissue remodeling is also numerically described by the nonlinear differential equation present in Equation (5.8). Also, the medium apparent density for the complete model domain can be again defined by $(\rho_{model})_{t_j}$ at a fictitious time t_j, and determined with the Equation (5.9), previously presented.

But, in this model, the determination of the apparent density on interest point $\boldsymbol{x}_I$, ρ_I, is performed in a very distinct way. Thus, based on the biological models presented previously, the apparent density is dependent on the dynamic behavior of the bone cells. So, for this model, the equations proposed are the following:

$$\begin{aligned} C(t_k,x_I,y_I) = C(t_{k-1},x_I,y_I) + \Delta t \Big[& \sigma_{Cx}\frac{\partial^2}{\partial x^2}C(t_{k-1},x_I,y_I) + \sigma_{Cy}\frac{\partial^2}{\partial y^2}C(t_{k-1},x_I,y_I) \\ & +\alpha_C C(t_{k-1},x_I,y_I)^{gCC} B(t_{k-1},x_I,y_I)^{gBC} \\ & -\beta_C C(t_{k-1},x_I,y_I) \Big] \end{aligned} \tag{6.7}$$

$$\begin{aligned} B(t_k,x_I,y_I) = B(t_{k-1},x_I,y_I) + \Delta t \Big[& \sigma_{Bx}\frac{\partial^2}{\partial x^2}B(t_{k-1},x_I,y_I) + \sigma_{By}\frac{\partial^2}{\partial y^2}B(t_{k-1},x_I,y_I) \\ & +\alpha_B C(t_{k-1},x_I,y_I)^{gCB} B(t_{k-1},x_I,y_I)^{gBB} \\ & -\beta_B B(t_{k-1},x_I,y_I) \Big] \end{aligned} \tag{6.8}$$

$$\begin{aligned} \rho(t_k,x_I,y_I) = \rho(t_{k-1},x_I,y_I) + \Delta t \Big[& \sigma_{\rho x}\frac{\partial^2}{\partial x^2}\rho(t_{k-1},x_I,y_I) + \sigma_{\rho y}\frac{\partial^2}{\partial y^2}\rho(t_{k-1},x_I,y_I) \\ & -k_C \max[0, C(t_{k-1},x_I,y_I) - \bar{C}(x_I,y_I)] \\ & +k_B max[0, B(t_{k-1},x_I,y_I) - \bar{B}(x_I,y_I)] \Big] \end{aligned} \tag{6.9}$$

The variables of the model are the density of osteoclasts, $C(t_k,x_I,y_I)$, the density of osteoblasts, $B(t_k,x_I,y_I)$ and the bone mass, $\rho(t_k,x_I,y_I)$. All variables are calculated in respect of a time t, at each instant k, and for each integration point I, with spatial coordinates x_I and y_I. In Equations (6.7) and (6.8), the diffusion coefficients σ_{ij} represent the migration of

the bone cell type i in the direction j. In Equation (6.9), $\sigma_{\rho x}$ and $\sigma_{\rho y}$ represents the stochasticity in the bone dynamics, as proposed by Ayati [3].

However, as depicted in the equations of the model being analyzed, the second order spatial partial derivates of $C(t_k, x_I, y_I)$, $B(t_k, x_I, y_I)$ and $\rho(t_k, x_I, y_I)$ have to be determined. But, since in this work, discrete numerical methods are being considered, the spatial partial derivate can be obtained using the data. Thus, consider a nodal set $= \{n_1, n_2, \dots, n_N\}$, with the following spatial coordinated $\boldsymbol{X} = \{\boldsymbol{x}_1, \boldsymbol{x}_2, \dots, \boldsymbol{x}_N\}$, discretizing the two-dimensional problem domain $\Omega \in \mathbb{R}^2$. Then, consider an interest point $\boldsymbol{x}_I \in \Omega$ and $\boldsymbol{x}_I \notin \boldsymbol{X}$. For the interest point $\boldsymbol{x}_I$, the influence domain (or the element) is defined. Then, the shape function is obtained, $\boldsymbol{\varphi}(\boldsymbol{x}_I)$. If the nodal data is known, $\boldsymbol{U} = \{u_1, u_2, \dots, u_N\}$,it is possible to interpolate the data to the interest point $\boldsymbol{x}_I$ with,

$$u(\boldsymbol{x}_I) = \boldsymbol{\varphi}(\boldsymbol{x}_I)\boldsymbol{U} \tag{6.10}$$

Thus, if the first and second partial derivatives are known, it is possible to obtain directly the first and second partial derivatives of the data field,

$$\frac{\partial u(\boldsymbol{x}_I)}{\partial x} = \frac{\partial \boldsymbol{\varphi}(\boldsymbol{x}_I)}{\partial x}\boldsymbol{U} \tag{6.11}$$

$$\frac{\partial u(\boldsymbol{x}_I)}{\partial y} = \frac{\partial \boldsymbol{\varphi}(\boldsymbol{x}_I)}{\partial y}\boldsymbol{U} \tag{6.12}$$

$$\frac{\partial^2 u(\boldsymbol{x}_I)}{\partial x^2} = \frac{\partial^2 \boldsymbol{\varphi}(\boldsymbol{x}_I)}{\partial x^2}\boldsymbol{U} \tag{6.13}$$

$$\frac{\partial^2 u(\boldsymbol{x}_I)}{\partial y^2} = \frac{\partial^2 \boldsymbol{\varphi}(\boldsymbol{x}_I)}{\partial y^2}\boldsymbol{U} \tag{6.14}$$

However, the three node 2D finite element method possesses a linear shape function, for which only one partial derivative is possible (such shape functions have C^1 continuity). Thus, for this kind of shape functions another approach is required. So, in order to obtain the second partial derivative of the data it is necessary first to obtain the interpolated partial derivative of the data field. Thus, for each node $\boldsymbol{x}_J \in \boldsymbol{X}$ it will be defined its influence domain (or element) and then, for each node, the shape functions and the first partial derivatives of the shape functions are constructed. Then, it is possible to obtain the partial derivative field of the data field using the following relations,

$$\frac{\partial u(\boldsymbol{x}_J)}{\partial x} = \frac{\partial \boldsymbol{\varphi}(\boldsymbol{x}_J)}{\partial x}\boldsymbol{U} \tag{6.15}$$

$$\frac{\partial u(\boldsymbol{x}_J)}{\partial y} = \frac{\partial \boldsymbol{\varphi}(\boldsymbol{x}_J)}{\partial y}\boldsymbol{U} \tag{6.16}$$

In the end, two new vectors are obtained: $\boldsymbol{U}_x = \{\partial u(\boldsymbol{x}_1)/\partial x, \dots, \partial u(\boldsymbol{x}_N)/\partial x\}$ and $\boldsymbol{U}_y = \{\partial u(\boldsymbol{x}_1)/\partial y, \dots, \partial u(\boldsymbol{x}_N)/\partial y\}$, which are the partial derivative fields of the scattered data.

Now, using the same procedure presented first, it is possible to obtain the second order partial derivatives of the data,

$$\frac{\partial^2 u(\boldsymbol{x}_I)}{\partial x^2} = \frac{\partial \boldsymbol{\varphi}(\boldsymbol{x}_I)}{\partial x} \boldsymbol{U}_x \tag{6.17}$$

$$\frac{\partial^2 u(\boldsymbol{x}_I)}{\partial y^2} = \frac{\partial \boldsymbol{\varphi}(\boldsymbol{x}_I)}{\partial y} \boldsymbol{U}_y \tag{6.18}$$

This procedure induces accumulative numerical errors, however it is sufficiently accurate to be used in such application [12].

In the end, the remodelling equilibrium is achieved when the condition given by Equation (5.13) is achieved.

6.3.2 - Remodeling Procedure

In this work, a new biological model was proposed and the scheme of the algorithm implemented is presented in Figure 6.2.

The initial phase of this algorithm is very similar to the mechanical model previously explained. Thus, using the available medical images, the pre-processing phase includes the domain discretization and the construction of the integration mesh as well as the shape functions. But, since it is not considered any mechanical stimulus, no boundary condition is applied and the only material property considered is the apparent density. For this case, it is also needed to define the set of cell parameters, proposed by Komarova [96] and Ayatti [3].

Also, to initialize the remodeling process, it is needed to first impose the initial spatial distribution of osteoclasts, C_0, and osteoblasts, B_0. So, since osteoblasts can differentiate into osteocytes or bone lining cells, it was assumed that osteoblasts could be found anywhere in bone. However, since osteoclasts only attach to the bone surface during the resorption phase and then abandon this local, this model assumes that initially osteoclasts can only be found on the bone's surface.

Then, spatial partial derivatives of osteoclasts, osteoblasts and bone mass are calculated, following the procedure described in the previous section. This allows to then determine the new cell density of osteoclasts, osteoblasts and bone mass, using the Equations (6.7), (6.8) and (6.9), respectively. Consequently, the medium apparent density of the model is updated and the remodeling procedure finishes when the stopping criterion given by Equation (5.13) is met.

The results obtained are represented with isomaps, being the procedure to obtain these isomaps the same as the one described in Chapter 5.

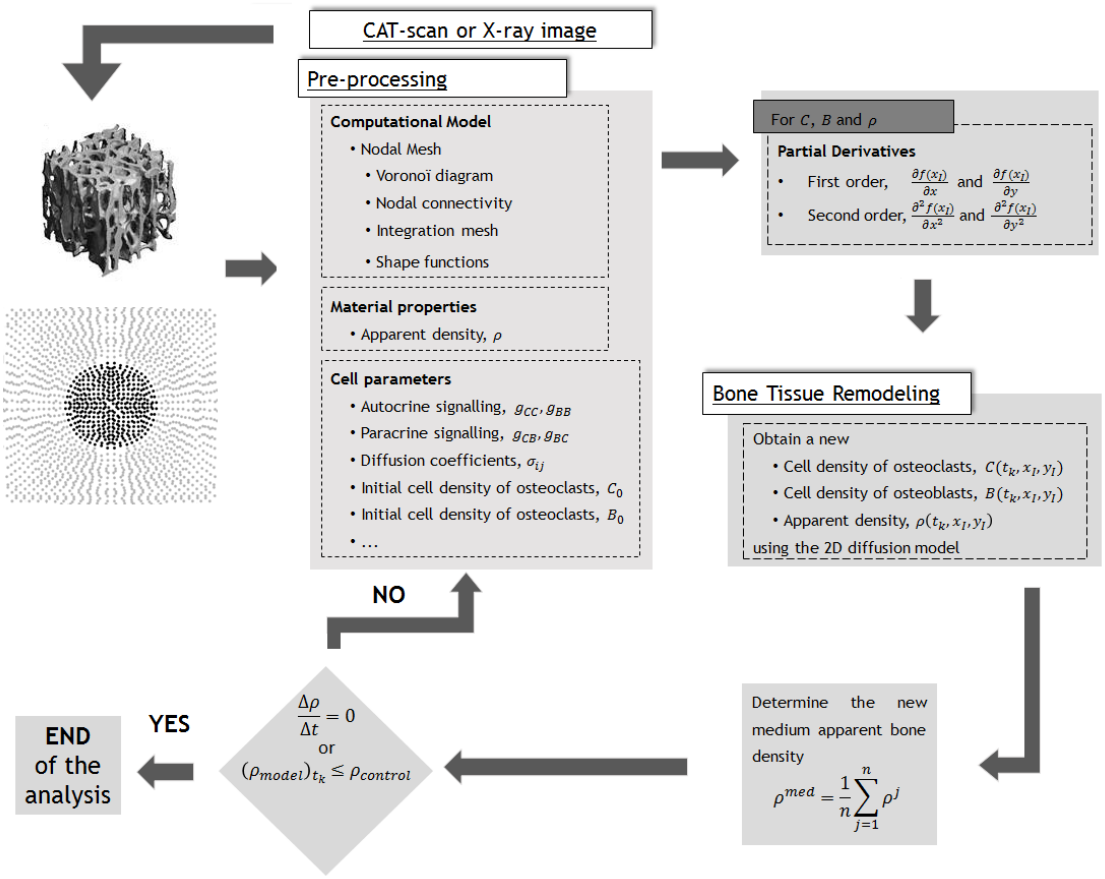

Figure 6.2 - Proposed bone remodeling algorithm for the biological model.

6.4 - 2D Bone Patch Analysis

6.4.1 - Initial Conditions

The proposed model in this work was validated by simulating one single cycle of bone remodeling. Using, again, a 2D bone patch, the initial mesh is illustrated in Figure 6.3a. For the analysis, the NNRPIM was the numerical method chosen, with the parameters indicated previously in Table 5.4. The use of the NNRPIM confers an advantage in the analysis, since the organically determination of the influence-domain, using the natural neighbour concept, approaches the natural behavior of cell. The initial spatial distribution of osteoclasts and osteoblasts is illustrated in Figure 6.3b and Figure 6.3c.

For this analysis, the bone cells' parameters have the values proposed by Komarova and Ayati for a single cycle of bone remodeling and are listed in Table 6.2. This data is based on histomorphometric studies [99].

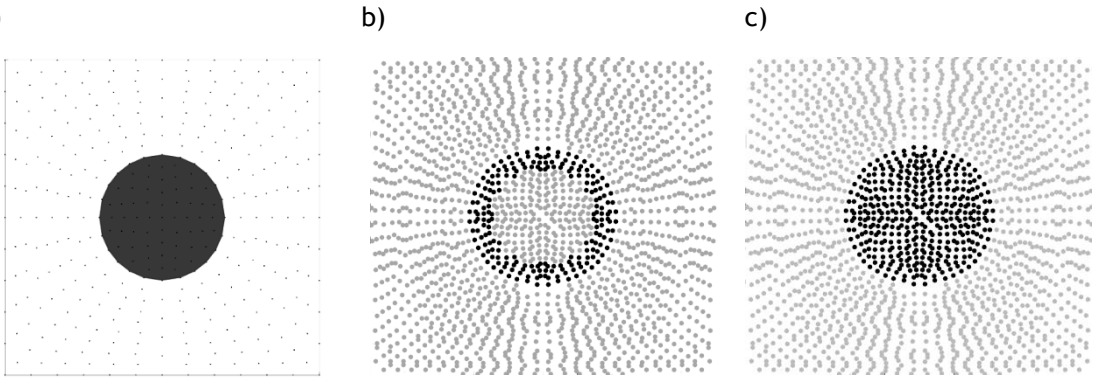

Figure 6.3 - (a) Mesh (383 nodes) used for the analysis, in which points inside the darker area are considered bone. (b) Initial distribution of osteoclasts indicated in black. (c) Initial distribution of osteoblasts indicated in black.

Table 6.2 - Parameters of the biological model.

C_0	$11.06\ cell$	k_C	$0.24\%\ cell^{-1}day^{-1}$
B_0	$212.13\ cell$	k_B	$0.0017\%\ cell^{-1}day^{-1}$
α_C	$3.0\ cell\ day^{-1}$	σ_{Cx}	$0.000001\ cell\ m^{-1}$
α_B	$4.0\ cell\ day^{-1}$	σ_{Cy}	$0.000001\ cell\ m^{-1}$
β_C	$0.2\ cell\ day^{-1}$	σ_{Bx}	$0.000001\ cell\ m^{-1}$
β_B	$0.02\ cell\ day^{-1}$	σ_{By}	$0.000001\ cell\ m^{-1}$
g_{CC}	0.5	$\sigma_{\rho x}$	$0.000001\ bone\ mass\ m^{-1}$
g_{CB}	1.0	$\sigma_{\rho y}$	$0.000001\ bone\ mass\ m^{-1}$
g_{BC}	-0.5	$\bar{C}$	$1.06\ cell$
g_{BB}	0.0	$\bar{B}$	$212.13\ cell$
Δt	$0.1\ day$		

6.4.2 - Results and Discussion

The bone remodeling process was successfully reproduced in 2D. In this example, a single event of bone remodeling was initiated by a momentary increase in the number of osteoclasts by 10 cells at time t=0.

In Figure 6.4 are represented the changes with time in the cell density of osteoclasts and osteoblasts for a certain point on the surface of bone. Their variation reveals that while density of osteoclasts was elevated, osteoclasts stimulated the slower process of osteoblast formation (through paracrine signaling), leading to an increase in the number of osteoblasts (Figure 6.4b). But, this increase only occurs after osteoclasts increase. Approximately 20 days after perturbation, osteoclast density returns to the steady state (Figure 6.4a). Osteoblasts also return slowly to basal level.

This described behavior are in very good agreement with the temporal pattern of changes observed in Komarova's and Ayati's models.

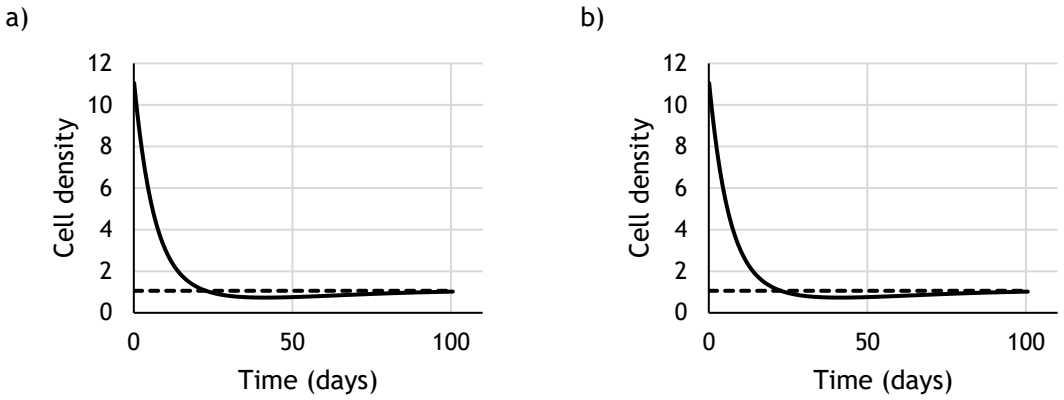

Figure 6.4 - Simulation of a bone remodeling cycle: (a) Changes with time in the cell density of osteoclasts and (b) osteoblasts. The dashed line represents the steady-state solution.

Consequent changes in bone mass, illustrated in Figure 6.5, demonstrate an initial phase of bone resorption, indicated by the drastic decrease of bone density. This is followed by a slower phase of bone formation, visible by the recovery of the initial bone density. These changes were calculated as a percentage of initial bone mass (100%). Comparing to literature, the variation of bone mass is more gradual, having a smoother profile. In this work, this aspect could be improved by reducing the time interval, given by the parameter Δt.

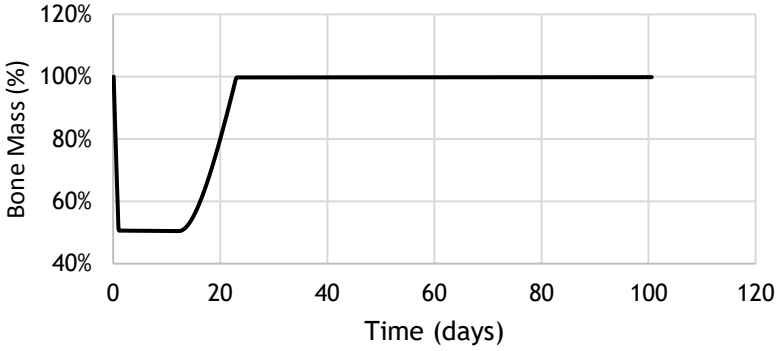

Figure 6.5 - Simulation of a bone remodeling cycle: Changes with time in bone mass.

Additionally, for the first time, with this work, the bone remodeling process was simulated in 2D. Thus, in Figure 6.6, it is visible the spatial variation of bone density at different time frames. Again, the variation profile of bone mass is as expected, occurring removal of bone only on the area where osteoclasts are present. Since osteoblasts are also present, bone mass recovers to its normal value and stabilizes.

Hence, results show that, with this biological model, it is possible to reproduce in 2D, the bone remodeling process as described in the literature.

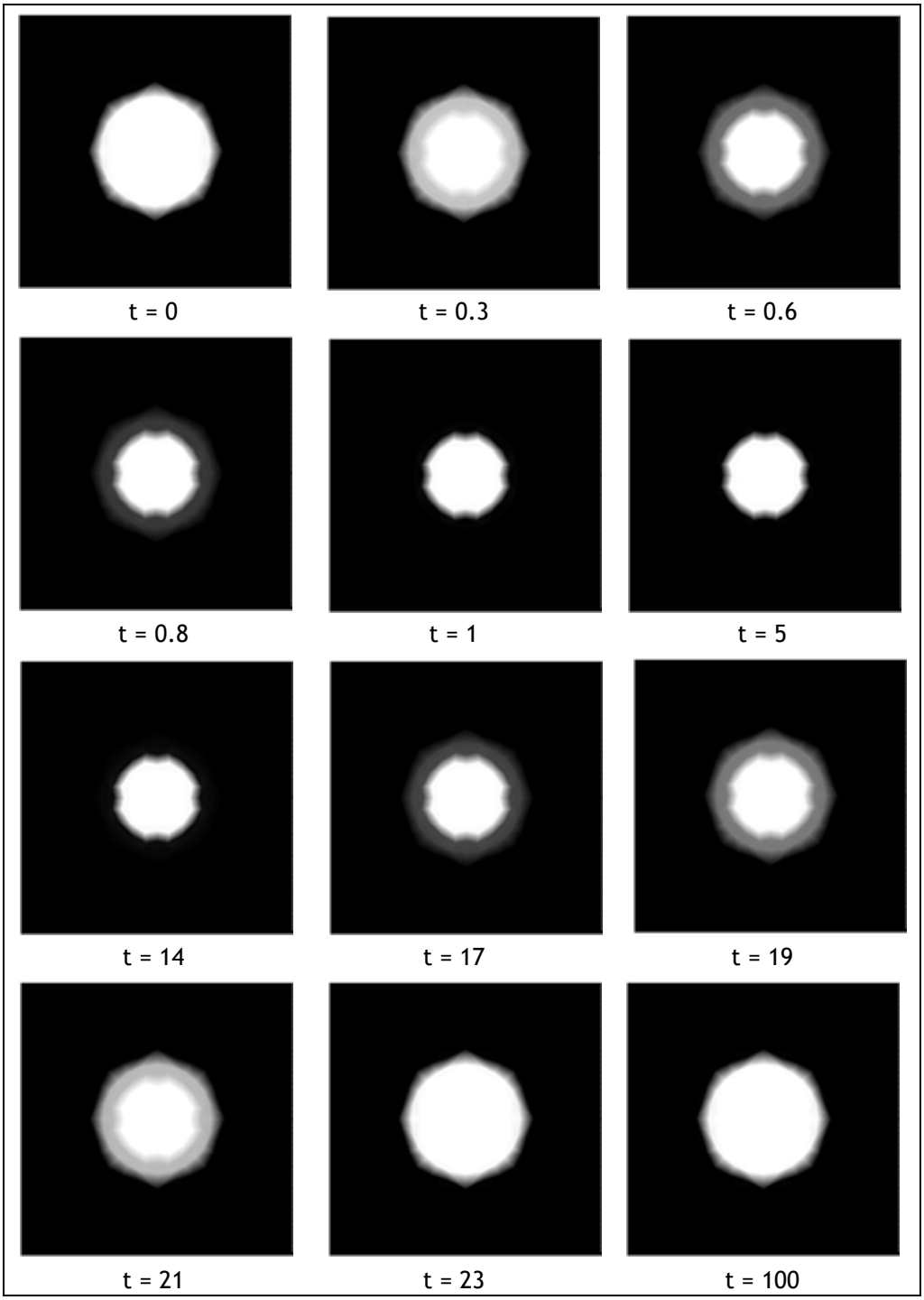

Figure 6.6 - Simulation of a bone remodeling cycle: spatial variation of bone mass along time (days).

Chapter 7

Mechanobiological Model

Despite first steps have already been taken, the field of mechanobiological models to simulate bone remodeling is still much unexplored. For instance, Hambli [100] developed a finite element model taking into account the bone material fatigue damage accumulation and mineralization, using the cellular behavior proposed by Komarova [96]. But, the model is not completely validated due to the lack of experimental data.

Therefore, in this work, a new approach is proposed. The relation between mechanical stimulus and biological response is described by a law based on experimental data. Thus, this chapter starts with a full description of the model proposed followed by validation through a 2D analysis using the NNRPIM.

7.1 - Proposed Model

7.1.1 - Model Description

Regarding the bone tissue remodeling, the nonlinear differential equation present in Equation (5.8) is again used to numerically describe the process, as well as the Equation (5.9) for the definition of the medium apparent density of the complete model domain.

The determination of the apparent density is obtained using the Equations (6.7), (6.8) and (6.9), introduced by the biological model, and a new equation that reflects the mechanical stimulus.

In fact, the aim of this model was to reproduce the interaction between bone cells under mechanical strain. So, since it is known that osteocytes are capable to convert mechanical stimulus into metabolic responses, an experimental law [101], represented in Figure 7.1a, that plotted cell density against shear stress, was used. In this study, it was proved and quantified the increase in cell density when cells were exposed to laminar flow.

Then, based on this law, a second order polynomial approximation was performed, as represented in Figure 7.1b, and the following expression was obtained

$$factor_{mech} = -109.45\bar{\sigma}^2 + 495.8\bar{\sigma} + 142.13 \tag{7.1}$$

in which $\bar{\sigma}$ defines the von Mises effective stress, expressed in Pa, and $factor_{mech}$ is expressed in percentage, being the variation in cell density in respect to the control population.

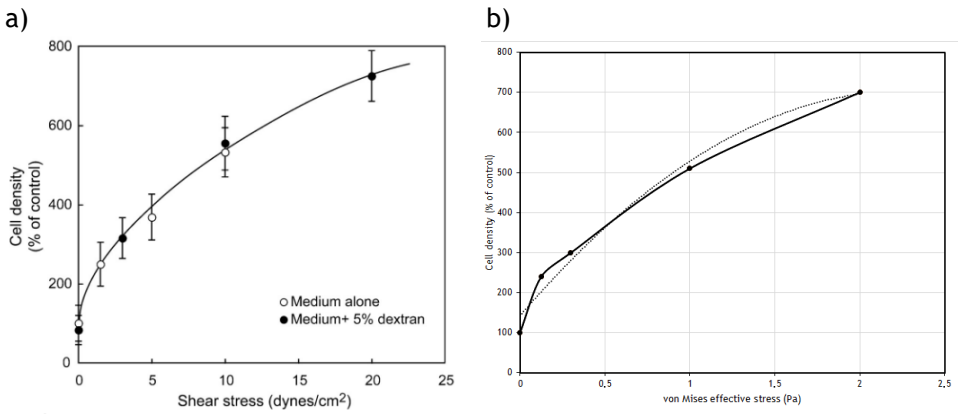

Figure 7.1 - (a) Experimental law [101]. (b) Second order polynomial approximation.

The value given by Equation (7.1) was interpreted as a mechanical factor that affects the cell density of osteoblasts determined with the biological model previously presented. Thus, from the equations given by the biological model, only osteoblasts density equation is affected as following

$$\boldsymbol{B(t_k, x_I, y_I) = B(t_{k-1}, x_I, y_I)_{biological} + B(t_{k-1}, x_I, y_I)_{biological} \times factor_{mech}} \tag{7.2}$$

being $B(t_k, x_I, y_I)_{biological}$ the density of osteoblasts obtained with the biological model. This expression was only applied in integration points considered bone. This identification is based on the value of their density, being bone if the following condition is valid: $0.1\ g/cm^3 < \rho < 2.1\ g/cm^3$.

However, the values of $\bar{\sigma}$ obtained during the simulation led to very high values of $factor_{mech}$. To solve this, the value of $\bar{\sigma}$ was normalized between $[0, 2]$.

Thus, in the end, the apparent density is not only affected by the equations proposed in the biological model, but also by the Equation (7.2), assuring the inclusion of both the biomechanical and the biochemical processes that occur during bone remodeling

As happens in the other models proposed in this work, the remodelling equilibrium is achieved when the condition given by Equation (5.13) is achieved.

7.1.2 - Remodeling Procedure

As described in the previous section, a new mechanobiological model was proposed taking into account the osteoblasts' response under mechanical strain. This algorithm was schematized and can be depicted in **Erro! A origem da referência não foi encontrada.**.

The algorithm starts with the pre-processing of the available medical images. This phase consists on the pre-processing of the nodal mesh and the imposition of the boundary conditions. Additionally, since it is a biomechanical model, both the mechanical properties and the cell parameters have to be introduced.

Then, the mechanical analysis proposed by the mechanical model and the biological analysis proposed in the biological model are simultaneously performed.

After this phase, the bone tissue remodeling process starts, taking into account both the biomechanical and the biochemical data obtained in the previously step. Regarding the biomechanical aspect of this analysis, the chosen approach was very similar to the one used in the mechanical model proposed. Thus, only some of the interest points $\boldsymbol{x}_I$ are chosen to remodel, optimizing the remodeling process in respect to the von Mises effective stress. So, only the interest points that belong to the interval $\bar{\sigma}(\boldsymbol{x}_I) > \bar{\sigma}_{control}$ are chosen. Then, a mechanical factor for each of those interest points is determined, according to the experimental law represented by Equation (7.1). In respect to the biochemical analysis of bone tissue remodeling, the approach is exactly the same as the one used in the biological model previously described.

In the end, the contribution of the two distinct analyses are taken into account with Equation (7.2), updating the cell density of osteoblasts. But, since this equation is only applied to points considered bone, in order to allow bone growth was necessary to update the cell density of osteoblasts to its neighbour points that were considered non-bone. This was achieved by applying to each node inside the influence cell of the bone node that is being analysed the following equation

$$B(t_k, x_I, y_I) = -\frac{B(t_k, x_b, y_b)}{r_2} \times r_{bI} + B(t_k, x_b, y_b) \tag{7.3}$$

being $B(t_k, x_I, y_I)$ the updated density of osteoblasts for each node inside the influence domain of the bone node, $B(t_k, x_b, y_b)$ the new density given by Equation (7.2) for the bone node with coordinates (x_b, y_b), r_{bI} the distance between the node considered bone and one of the nodes inside its influence domain and r_2 the distance from the node considered bone and its furthest node inside its influence domain. Thus, the bone growth is radial and only occurs in the vicinity of areas considered bone.

After establishing the new cell density of osteoclasts, osteoblasts and the new apparent density field, the medium apparent bone density, ρ^{med}, is determined. At this point, the algorithm can follow two distinct paths, depending on the Equation (5.13). It can move forward to the next iteration step or end. The final results obtained are represented with isomaps, being the procedure to obtain these isomaps the same as the one described in Chapter 5.

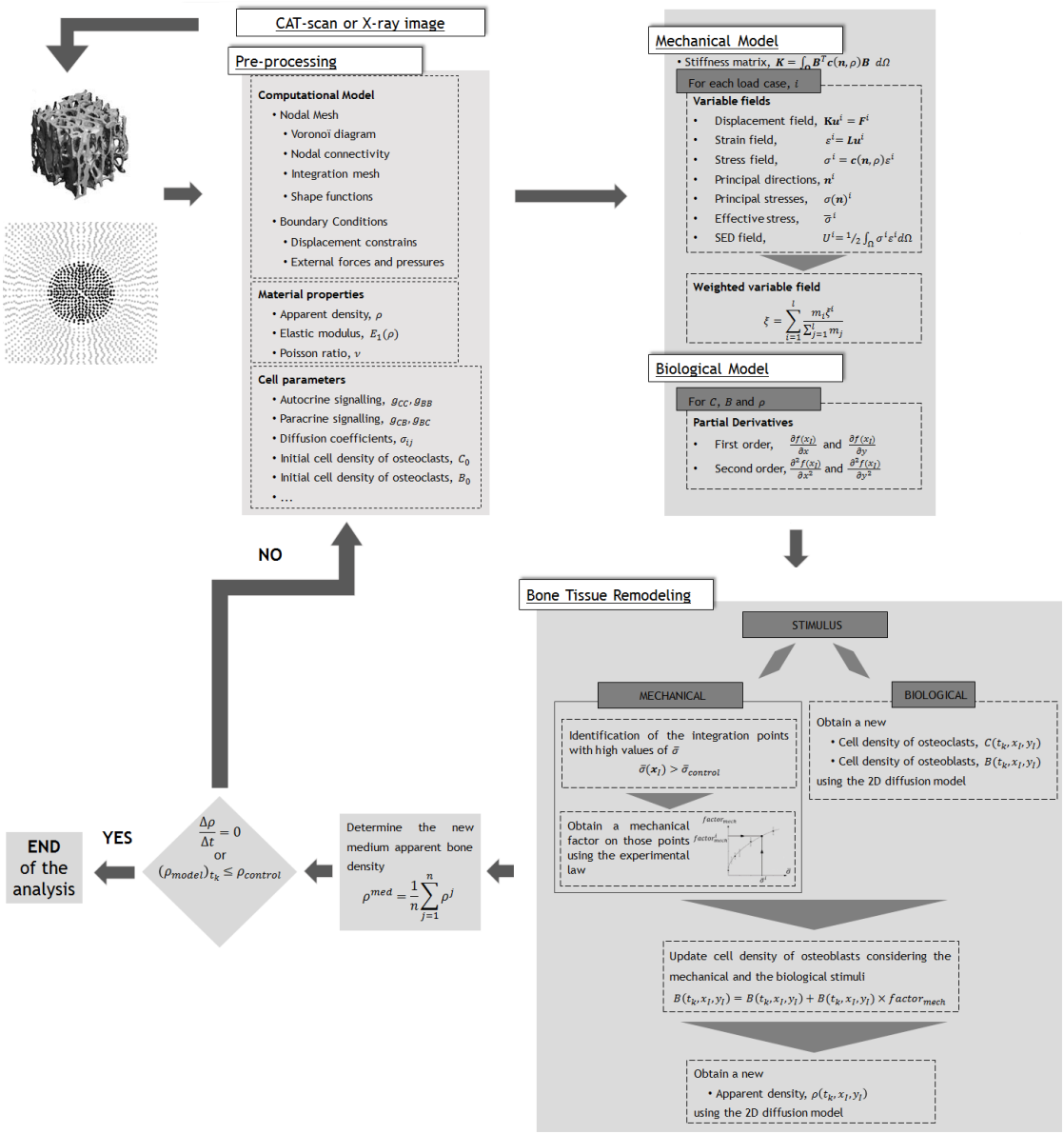

Figure 7.2 - Proposed bone remodeling algorithm for the mechanobiological model.

7.2 - 2D Bone Patch Analysis

7.2.1 - Initial Conditions

The initial mesh was the same as the one used in the biological model, as well as the initial spatial distribution of bone cells (Figure 6.3). To validate the algorithm, it was applied a constant compressive stress on the top and on the bottom of the mesh. The node displacement was constrained in the x direction along the line given by $0.3 < x < 0.7$. These boundary conditions are represent in Figure 7.3. The numerical method tested was the NNRPIM and the model's parameters were the ones proposed in the biological model (Table 6.2), except the initial density of osteoclasts. The value used was $C_0 = 1.06$. Also, the value of $\bar{\sigma}_{control}$ was $1.1Pa$.

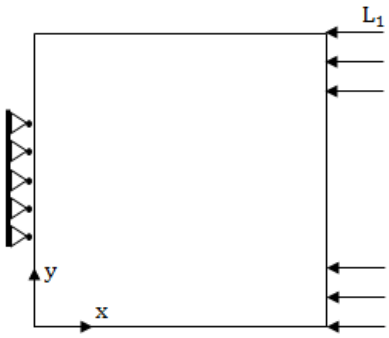

Figure 7.3 - Plate model geometry and essential and natural boundary conditions

7.2.2 - Results and Discussion

This simulation differed from the one ran in Chapter 6, since bone remodeling process was not induced by an increase on osteoclasts density. In fact, in this test, the purpose was to test if osteoblasts were capable to form bone according to the stress effective levels. As depicted in Figure 7.4, bone can adapt its morphology when stimulated mechanically, growing in accordance to the loads applied. However, this growth is too abrupt, suggesting that the area of neighbors affected by the $factor_{mech}$ is too broad.

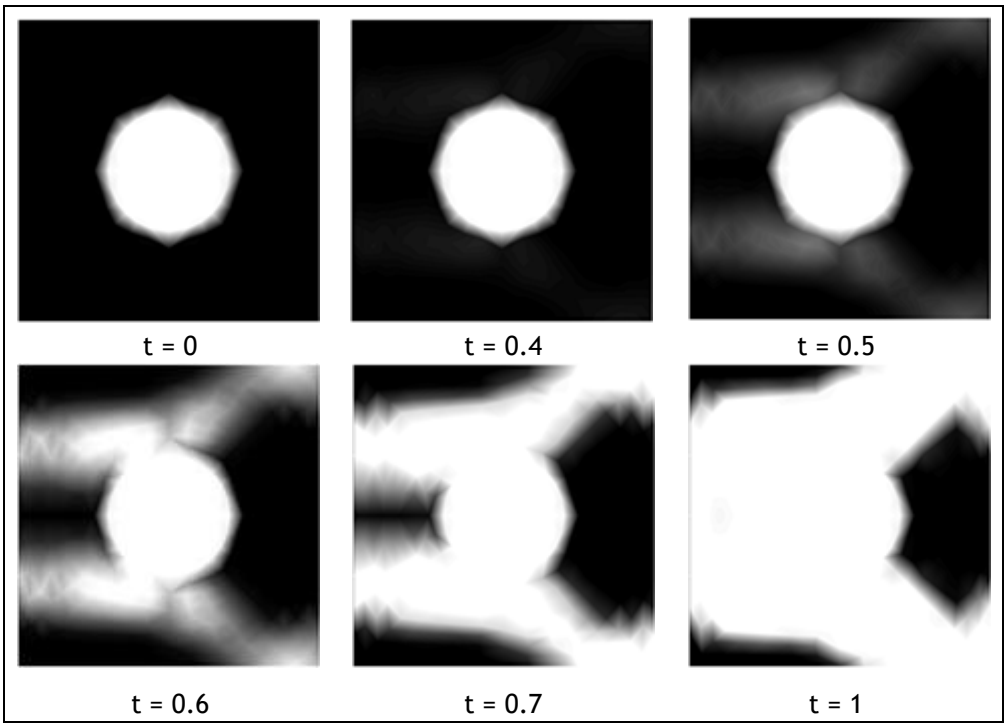

Figure 7.4 - Spatial variation of bone mass along time (days).

Although lots of improvements have to be done in this model, this algorithm has the potential to become an important tool that integrates both the biomechanical and the biochemical processes that occur during a bone remodeling process.

Chapter 8

Conclusions and Future Work

The seed that originated this work was the conceptual model proposed by Frost. But, instead of testing it using experimental models, mathematical modelling was the approach chosen. In bone biology, these types of models are slowly gaining more relevance and becoming an important tool to study bone phenomena. Therefore, focusing on the bone remodeling process, three models with different purposes were created.

Throughout the work, several breakthroughs were achieved. Regarding the mechanical model, the bone trabecular morphology was reproduced with success, using the RPIM for the first time in this type of simulations.

The following microscale bone remodeling simulations, using the biological model, showed results in very good agreement with the temporal pattern of changes stated in the literature. Additionally, it was the first time that the model proposed by Komarova was adapted to 2D, reproducing accurately the spatial behavior of bone cells. In respect to the mechanobiological model, bone was able to adapt its morphology, having osteoblasts forming bone where needed, according to the mechanical stimulus.

Thus, reviewing the objectives proposed initially, this work was able to accomplish with success all of them. Distinct models were created to consider separately the biomechanical and the biochemical aspects of bone remodeling. Both were validated with high accurate results and then integrated in a final mechanobiological model. This last model was only explored superficially, but results are promising. Therefore, although this project contributes with important data to the study of bone remodeling, it is possible to consider it as preliminary work, since numerous improvements can be pointed.

For the mechanical model, complementary studies should be performed with higher density meshes. Also, it would be interesting to test this algorithm with the other mechanical cases proposed by Beaupré and even test it on the remodeling process of other bones.

In respect to the biochemical model, the simulation should be ran with other numerical methods and test other types of dynamic behavior, such as cyclic bone remodeling or unstable behavior similar to pathological bone remodeling disorders. It would also be interesting to add the systemic regulation controlled by hormones.

Regarding the mechanobiological model, it would be interesting to test it with other control values of von Mises effective stress, $\bar{\sigma}_{control}$. It is important to integrate also the biomechanical response of osteoclasts, since low amounts of loading causes increased

osteoclastic resorption. Also, test it with distinct numerical methods would enrich the data. Then, it would be crucial to adapt this model in order to reproduce dysfunctional system behaviors and ultimately the effect of drugs in the system.

References

[1] C. Cooper, G. Campion, and L. J. Melton, “Hip fractures in the elderly: a world-wide projection.,” *Osteoporos. Int.*, vol. 2, no. 6, pp. 285–9, Nov. 1992.

[2] J. Belinha, R. M. Natal Jorge, and L. M. J. S. Dinis, “Bone tissue remodelling analysis considering a radial point interpolator meshless method,” *Eng. Anal. Bound. Elem.*, vol. 36, no. 11, pp. 1660–1670, 2012.

[3] B. P. Ayati, C. M. Edwards, G. F. Webb, and J. P. Wikswo, “A mathematical model of bone remodeling dynamics for normal bone cell populations and myeloma bone disease.,” *Biol. Direct*, vol. 5, p. 28, 2010.

[4] P. Pivonka and S. V Komarova, “Mathematical modeling in bone biology: from intracellular signaling to tissue mechanics.,” *Bone*, vol. 47, no. 2, pp. 181–9, 2010.

[5] J. B. Tyrovola and X. Odont, “The ‘Mechanostat Theory’ of Frost and the OPG/RANKL/RANK System,” *J. Cell. Biochem.*, vol. 116, no. 12, pp. 2724–2729, 2015.

[6] J. Wolff, *The Law of Bone Remodelling*. Berlin, Heidelberg: Springer Berlin Heidelberg, 1986.

[7] D. J. Hadjidakis and I. I. Androulakis, “Bone remodeling,” *Ann. N. Y. Acad. Sci.*, vol. 1092, pp. 385–96, Dec. 2006.

[8] J. Belinha, *Meshless Methods in Biomechanics*, vol. 16. Springer International Publishing, 2014.

[9] F. H. Netter, *Musculoskeletal system - Netter collection of medical illustrations*, 1st ed. Elsevier Saunders, 1994.

[10] S. L. Teitelbaum, “Bone resorption by osteoclasts.,” *Science*, vol. 289, no. 5484, pp. 1504–8, 2000.

[11] T. M. Post, S. C. L. M. Cremers, T. Kerbusch, and M. Danhof, “Bone Physiology, Disease and Treatment,” *Clin. Pharmacokinet.*, vol. 49, no. 2, pp. 89–118, 2010.

[12] J. Belinha, *Meshless Methods in Biomechanics - Bone Tissue Remodelling Analysis*, Vol.16 ed. Springer Netherlands, 2014.

[13] A. H. Nobbs, H. F. Jenkinson, and N. S. Jakubovics, “Critical Reviews in Oral Biology & Medicine,” *J Dent Res*, vol. 90, no. 11, pp. 1271–1278, 2011.

[14] L. G. Raisz, “Science in medicine Pathogenesis of osteoporosis : concepts , conflicts , and prospects,” vol. 115, no. 12, 2005.

[15] T. L. Burgess, Y. Qian, S. Kaufman, B. D. Ring, G. Van, C. Capparelli, M. Kelley, H. Hsu, W. J. Boyle, C. R. Dunstan, S. Hu, and D. L. Lacey, “The ligand for osteoprotegerin (OPGL) directly activates mature osteoclasts.,” *J. Cell Biol.*, vol. 145, no. 3, pp. 527–38, May 1999.

[16] K. Matsuzaki, N. Udagawa, N. Takahashi, K. Yamaguchi, H. Yasuda, N. Shima, T. Morinaga, Y. Toyama, Y. Yabe, K. Higashio, and T. Suda, “Osteoclast differentiation factor (ODF) induces osteoclast-like cell formation in human peripheral blood mononuclear cell cultures.,” *Biochem. Biophys. Res. Commun.*, vol. 246, no. 1, pp. 199–204, May 1998.

[17] J. M. Quinn, S. Neale, Y. Fujikawa, J. O. McGee, and N. A. Athanasou, “Human osteoclast formation from blood monocytes, peritoneal macrophages, and bone marrow cells.,” *Calcif. Tissue Int.*, vol. 62, no. 6, pp. 527–31, Jun. 1998.

[18] Y. Fujikawa, A. Sabokbar, S. D. Neale, I. Itonaga, T. Torisu, and N. A. Athanasou, “The effect of macrophage-colony stimulating factor and other humoral factors

(interleukin-1, -3, -6, and -11, tumor necrosis factor-alpha, and granulocyte macrophage-colony stimulating factor) on human osteoclast formation from circulating cells.," *Bone*, vol. 28, no. 3, pp. 261–7, Mar. 2001.

[19] W. J. Boyle, W. S. Simonet, and D. L. Lacey, "Osteoclast differentiation and activation.," *Nature*, vol. 423, no. 6937, pp. 337–42, May 2003.

[20] V. Kartsogiannis, H. Zhou, N. J. Horwood, R. J. Thomas, D. K. Hards, J. M. Quinn, P. Niforas, K. W. Ng, T. J. Martin, and M. T. Gillespie, "Localization of RANKL (receptor activator of NF kappa B ligand) mRNA and protein in skeletal and extraskeletal tissues.," *Bone*, vol. 25, no. 5, pp. 525–34, Nov. 1999.

[21] K. Tsukii, N. Shima, S. Mochizuki, K. Yamaguchi, M. Kinosaki, K. Yano, O. Shibata, N. Udagawa, H. Yasuda, T. Suda, and K. Higashio, "Osteoclast Differentiation Factor Mediates an Essential Signal for Bone Resorption Induced by 1α,25-Dihydroxyvitamin D3, Prostaglandin E2, or Parathyroid Hormone in the Microenvironment of Bone," *Biochem. Biophys. Res. Commun.*, vol. 246, no. 2, pp. 337–341, May 1998.

[22] D. L. Lacey, E. Timms, H. L. Tan, M. J. Kelley, C. R. Dunstan, T. Burgess, R. Elliott, A. Colombero, G. Elliott, S. Scully, H. Hsu, J. Sullivan, N. Hawkins, E. Davy, C. Capparelli, A. Eli, Y. X. Qian, S. Kaufman, I. Sarosi, V. Shalhoub, G. Senaldi, J. Guo, J. Delaney, and W. J. Boyle, "Osteoprotegerin ligand is a cytokine that regulates osteoclast differentiation and activation.," *Cell*, vol. 93, no. 2, pp. 165–76, Apr. 1998.

[23] A. E. Kearns, S. Khosla, and P. J. Kostenuik, "Receptor activator of nuclear factor kappaB ligand and osteoprotegerin regulation of bone remodeling in health and disease.," *Endocr. Rev.*, vol. 29, no. 2, pp. 155–92, Apr. 2008.

[24] U. H. Lerner, "Bone remodeling in post-menopausal osteoporosis.," *J. Dent. Res.*, vol. 85, no. 7, pp. 584–95, Jul. 2006.

[25] B. J. Seibel MJ, Robins SP, *Dynamics of Bone and Cartilage Metabolism: Principles and Clinical Applications*, 2nd ed. Academic Press, 2006.

[26] L. G. Raisz, "Physiology and pathophysiology of bone remodeling.," *Clin. Chem.*, vol. 45, no. 8 Pt 2, pp. 1353–8, Aug. 1999.

[27] S. L. Teitelbaum, "Bone resorption by osteoclasts.," *Science*, vol. 289, no. 5484, pp. 1504–8, Sep. 2000.

[28] M. Zaidi, H. C. Blair, B. S. Moonga, E. Abe, and C. L. H. Huang, "Osteoclastogenesis, bone resorption, and osteoclast-based therapeutics.," *J. Bone Miner. Res.*, vol. 18, no. 4, pp. 599–609, Apr. 2003.

[29] M. Schoppet, K. T. Preissner, and L. C. Hofbauer, "RANK ligand and osteoprotegerin: paracrine regulators of bone metabolism and vascular function.," *Arterioscler. Thromb. Vasc. Biol.*, vol. 22, no. 4, pp. 549–53, Apr. 2002.

[30] A. M. Sattler, M. Schoppet, J. R. Schaefer, and L. C. Hofbauer, "Novel aspects on RANK ligand and osteoprotegerin in osteoporosis and vascular disease.," *Calcif. Tissue Int.*, vol. 74, no. 1, pp. 103–6, Jan. 2004.

[31] S. Tanaka, I. Nakamura, J.-I. Inoue, H. Oda, and K. Nakamura, "Signal transduction pathways regulating osteoclast differentiation and function.," *J. Bone Miner. Metab.*, vol. 21, no. 3, pp. 123–33, Jan. 2003.

[32] R. Marcus, D. Feldman, D. W. Dempster, M. Luckey, and J. A. Cauley, *Osteoporosis*. Elsevier, 2008.

[33] L. F. Bonewald and S. L. Dallas, "Role of active and latent transforming growth factor beta in bone formation.," *J. Cell. Biochem.*, vol. 55, no. 3, pp. 350–7, Jul. 1994.

[34] G. D. Roodman, "Cell biology of the osteoclast.," *Exp. Hematol.*, vol. 27, no. 8, pp. 1229–41, Aug. 1999.

[35] D. J. Simmons and M. . Grynpas, "Mechanisms of bone formation in vivo," in *Hall, B.K. (Ed.), Bone, Vol. I, A Treatrise*, Boca Raton, FL, 1990.

[36] J. M. Hock, E. Canalis, and M. Centrella, "Transforming growth factor-beta stimulates bone matrix apposition and bone cell replication in cultured fetal rat calvariae.," *Endocrinology*, vol. 126, no. 1, pp. 421–6, Jan. 1990.

[37] C. Marcelli, A. J. Yates, and G. R. Mundy, "In vivo effects of human recombinant transforming growth factor beta on bone turnover in normal mice.," *J. Bone Miner. Res.*, vol. 5, no. 10, pp. 1087–96, Oct. 1990.

[38] D. Rosen, S. C. Miller, E. DeLeon, A. Y. Thompson, H. Bentz, M. Mathews, and S. Adams, "Systemic administration of recombinant transforming growth factor beta 2

(rTGF-beta 2) stimulates parameters of cancellous bone formation in juvenile and adult rats.," *Bone*, vol. 15, no. 3, pp. 355–9, Jan. 1994.

[39] E. F. Eriksen, "Cellular mechanisms of bone remodeling.," *Rev. Endocr. Metab. Disord.*, vol. 11, no. 4, pp. 219–27, Dec. 2010.

[40] T. Alliston, L. Choy, P. Ducy, G. Karsenty, and R. Derynck, "TGF-beta-induced repression of CBFA1 by Smad3 decreases cbfa1 and osteocalcin expression and inhibits osteoblast differentiation.," *EMBO J.*, vol. 20, no. 9, pp. 2254–72, May 2001.

[41] E. M. Greenfield, Y. Bi, and A. Miyauchi, "Regulation of osteoclast activity.," *Life Sci.*, vol. 65, no. 11, pp. 1087–102, Jan. 1999.

[42] M. J. Oursler, P. Osdoby, J. Pyfferoen, B. L. Riggs, and T. C. Spelsberg, "Avian osteoclasts as estrogen target cells.," *Proc. Natl. Acad. Sci. U. S. A.*, vol. 88, no. 15, pp. 6613–7, Aug. 1991.

[43] A. Taranta, M. Brama, A. Teti, V. De luca, R. Scandurra, G. Spera, D. Agnusdei, J. D. Termine, and S. Migliaccio, "The selective estrogen receptor modulator raloxifene regulates osteoclast and osteoblast activity in vitro.," *Bone*, vol. 30, no. 2, pp. 368–76, Feb. 2002.

[44] D. E. Hughes, A. Dai, J. C. Tiffee, H. H. Li, G. R. Mundy, and B. F. Boyce, "Estrogen promotes apoptosis of murine osteoclasts mediated by TGF-beta.," *Nat. Med.*, vol. 2, no. 10, pp. 1132–6, Oct. 1996.

[45] J.-R. Chen, L. I. Plotkin, J. I. Aguirre, L. Han, R. L. Jilka, S. Kousteni, T. Bellido, and S. C. Manolagas, "Transient versus sustained phosphorylation and nuclear accumulation of ERKs underlie anti-versus pro-apoptotic effects of estrogens.," *J. Biol. Chem.*, vol. 280, no. 6, pp. 4632–8, Feb. 2005.

[46] J. Chow, J. H. Tobias, K. W. Colston, and T. J. Chambers, "Estrogen maintains trabecular bone volume in rats not only by suppression of bone resorption but also by stimulation of bone formation.," *J. Clin. Invest.*, vol. 89, no. 1, pp. 74–8, Jan. 1992.

[47] Q. Qu, M. Perälä-Heape, A. Kapanen, J. Dahllund, J. Salo, H. K. Väänänen, and P. Härkönen, "Estrogen enhances differentiation of osteoblasts in mouse bone marrow culture.," *Bone*, vol. 22, no. 3, pp. 201–9, Mar. 1998.

[48] M. Ernst, J. K. Heath, and G. A. Rodan, "Estradiol effects on proliferation, messenger ribonucleic acid for collagen and insulin-like growth factor-I, and parathyroid hormone-stimulated adenylate cyclase activity in osteoblastic cells from calvariae and long bones.," *Endocrinology*, vol. 125, no. 2, pp. 825–33, Aug. 1989.

[49] L. C. Hofbauer, S. Khosla, C. R. Dunstan, D. L. Lacey, T. C. Spelsberg, and B. L. Riggs, "Estrogen stimulates gene expression and protein production of osteoprotegerin in human osteoblastic cells.," *Endocrinology*, vol. 140, no. 9, pp. 4367–70, Sep. 1999.

[50] U. Sarma, M. Edwards, K. Motoyoshi, and A. M. Flanagan, "Inhibition of bone resorption by 17beta-estradiol in human bone marrow cultures.," *J. Cell. Physiol.*, vol. 175, no. 1, pp. 99–108, Apr. 1998.

[51] C. K. Lea, U. Sarma, and A. M. Flanagan, "Macrophage colony stimulating-factor transcripts are differentially regulated in rat bone-marrow by gender hormones.," *Endocrinology*, vol. 140, no. 1, pp. 273–9, Jan. 1999.

[52] P. Lips, "Vitamin D deficiency and secondary hyperparathyroidism in the elderly: consequences for bone loss and fractures and therapeutic implications.," *Endocr. Rev.*, vol. 22, no. 4, pp. 477–501, Aug. 2001.

[53] J. E. Compston, "Sex steroids and bone.," *Physiol. Rev.*, vol. 81, no. 1, pp. 419–447, Jan. 2001.

[54] R. L. Jilka, "Biology of the basic multicellular unit and the pathophysiology of osteoporosis.," *Med. Pediatr. Oncol.*, vol. 41, no. 3, pp. 182–5, Sep. 2003.

[55] A. G. Robling, A. B. Castillo, and C. H. Turner, "Biomechanical and Molecular Regulation of Bone Remodeling," *Annu. Rev. Biomed. Eng.*, vol. 8, no. 1, pp. 455–498, 2006.

[56] L. C. Hofbauer, C. A. Kühne, and V. Viereck, "The OPG/RANKL/RANK system in metabolic bone diseases.," *J. Musculoskelet. Neuronal Interact.*, vol. 4, no. 3, pp. 268–75, Sep. 2004.

[57] P. S. Heckbert, "Introduction to Finite Element Methods," pp. 1–10, 1993.

[58] T. Y. Chao, W. K. Chow, and H. Kong, "A review on the applications of finite element method to heat transfer and fluid flow," vol. 3, no. 1, pp. 1–19, 2002.

[59] G. Strang and G. J. Fix, *An analysis of the finite element method*. Wellesley-Cambridge Press, 1988.
[60] E. Becker, G. Carey, and J. Oden, *Finite Elements, An Introduction: Volume I*. 1981.
[61] V. P. Nguyen, T. Rabczuk, S. Bordas, and M. Duflot, "Meshless methods: A review and computer implementation aspects," *Math. Comput. Simul.*, vol. 79, no. 3, pp. 763–813, 2008.
[62] T. Belytschko, Y. Krongauz, D. Organ, M. Fleming, and P. Krysl, "Meshless methods: An overview and recent developments," *Comput. Methods Appl. Mech. Eng.*, vol. 139, no. 1–4, pp. 3–47, 1996.
[63] J. Belinha, L. M. J. S. Dinis, and R. M. N. Jorge, "The Meshless Methods in the Bone Tissue Remodelling Analysis," *Procedia Eng.*, vol. 110, pp. 51–58, 2015.
[64] B. Nayroles, G. Touzot, and P. Villon, "Generalizing the finite element method: Diffuse approximation and diffuse elements," *Comput. Mech.*, vol. 10, no. 5, pp. 307–318, 1992.
[65] T. Belytschko, L. Gu, and Y. Y. Lu, "Fracture and crack growth by element free Galerkin methods," *Model. Simul. Mater. Sci. Eng.*, vol. 2, no. 3A, pp. 519–534, May 1994.
[66] G. R. Liu and Y. T. Gu, "A point interpolation method for two-dimensional solids," *Int. J. Numer. Methods Eng.*, vol. 50, no. 4, pp. 937–951, Feb. 2001.
[67] J. G. Wang and G. R. Liu, "A point interpolation meshless method based on radial basis functions," *Int. J. Numer. Methods Eng.*, vol. 54, no. 11, pp. 1623–1648, Aug. 2002.
[68] J. G. Wang and G. R. Liu, "On the optimal shape parameters of radial basis functions used for 2-D meshless methods," *Comput. Methods Appl. Mech. Eng.*, vol. 191, no. 23–24, pp. 2611–2630, Mar. 2002.
[69] L. Traversoni, "Natural neighbor finite elements," vol. 2, Jan. 1994.
[70] N. Sukumar, B. Moran, A. Y. Semenov, and V. V Belikov, "Natural neighbour Galerkin methods," *Int. J. Numer. Methods Eng.*, vol. 50, pp. 1–27, Jan. 2001.
[71] J. Braun and M. Sambridge, "A numerical method for solving partial differential equations on highly irregular evolving grids," *Nature*, vol. 376, no. 6542, pp. 655–660, Aug. 1995.
[72] N. Sukumar, B. Moran, and T. Belytschko, "The natural element method in solid mechanics," *Int. J. Numer. Methods Eng.*, vol. 43, no. 5, pp. 839–887, Nov. 1998.
[73] L. M. J. S. Dinis, R. M. Natal Jorge, and J. Belinha, "Analysis of 3D solids using the natural neighbour radial point interpolation method," *Comput. Methods Appl. Mech. Eng.*, vol. 196, no. 13–16, pp. 2009–2028, Mar. 2007.
[74] W. K. Liu, S. Jun, and Y. F. Zhang, "Reproducing kernel particle methods," *Int. J. Numer. Methods Fluids*, vol. 20, no. 8–9, pp. 1081–1106, Apr. 1995.
[75] S. N. Atluri and T. Zhu, "A new Meshless Local Petrov-Galerkin (MLPG) approach in computational mechanics," *Comput. Mech.*, vol. 22, no. 2, pp. 117–127, Aug. 1998.
[76] J. Belinha, L. M. J. S. Dinis, and R. M. Natal Jorge, "The analysis of the bone remodelling around femoral stems: A meshless approach," *Math. Comput. Simul.*, vol. 121, pp. 64–94, 2015.
[77] R. Sibson, "A vector identity for the Dirichlet tessellation," *Math. Proc. Camb. Phil. Soc*, vol. 87, 1980.
[78] L. M. J. S. Dinis, R. M. Natal Jorge, and J. Belinha, "Analysis of 3D solids using the natural neighbour radial point interpolation method," *Comput. Methods Appl. Mech. Eng.*, vol. 196, no. 13, pp. 2009–2028, 2007.
[79] R. L. Hardy, "Theory and applications of the multiquadric-biharmonic method 20 years of discovery 1968–1988," *Comput. Math. with Appl.*, vol. 19, no. 8–9, pp. 163–208, 1990.
[80] L. M. J. S. Dinis, R. M. Natal Jorge, and J. Belinha, "Analysis of plates and laminates using the natural neighbour radial point interpolation method," *Eng. Anal. Bound. Elem.*, vol. 32, no. 3, pp. 267–279, Mar. 2008.
[81] M. A. Golberg, C. S. Chen, and H. Bowman, "Some recent results and proposals for the use of radial basis functions in the BEM," *Eng. Anal. Bound. Elem.*, vol. 23, no. 4, pp. 285–296, Apr. 1999.
[82] Y. Fung, *Foundations of Solid Mechanics*. New Jersey, USA: Prentice-Hall, 1965.

[83] L. Malvern, *Introduction of the mechancis of a continuous medium*. New Jersey, USA: Prentice-Hall, 1969.

[84] B. L. Riggs and A. M. Parfitt, "Drugs used to treat osteoporosis: the critical need for a uniform nomenclature based on their action on bone remodeling.," *J. Bone Miner. Res.*, vol. 20, no. 2, pp. 177–84, Feb. 2005.

[85] H. E. Pettermann, T. J. Reiter, and F. G. Rammerstorfer, "Computational simulation of internal bone remodeling," *Arch. Comput. Methods Eng.*, vol. 4, no. 4, pp. 295–323, Dec. 1997.

[86] D. C. Wirtz, N. Schiffers, T. Pandorf, K. Radermacher, D. Weichert, and R. Forst, "Critical evaluation of known bone material properties to realize anisotropic FE-simulation of the proximal femur.," *J. Biomech.*, vol. 33, no. 10, pp. 1325–30, Oct. 2000.

[87] J. C. Lotz, T. N. Gerhart, and W. C. Hayes, "Mechanical properties of metaphyseal bone in the proximal femur.," *J. Biomech.*, vol. 24, no. 5, pp. 317–29, Jan. 1991.

[88] P. Zioupos, R. B. Cook, and J. R. Hutchinson, "Some basic relationships between density values in cancellous and cortical bone.," *J. Biomech.*, vol. 41, no. 9, pp. 1961–8, Jan. 2008.

[89] J. Belinha, R. M. N. Jorge, and L. M. J. S. Dinis, "A meshless microscale bone tissue trabecular remodelling analysis considering a new anisotropic bone tissue material law," *Comput. Methods Biomech. Biomed. Engin.*, no. August 2012, pp. 1–15, 2012.

[90] J. BELINHA, L. M. J. S. DINIS, and R. M. N. JORGE, "THE MANDIBLE REMODELING INDUCED BY DENTAL IMPLANTS: A MESHLESS APPROACH," *J. Mech. Med. Biol.*, vol. 15, no. 04, Aug. 2015.

[91] G. Chen, G. Pettet, M. Pearcy, and D. L. S. McElwain, "Comparison of two numerical approaches for bone remodelling.," *Med. Eng. Phys.*, vol. 29, no. 1, pp. 134–9, Jan. 2007.

[92] G. S. Beaupré, T. E. Orr, and D. R. Carter, "An approach for time-dependent bone modeling and remodeling--theoretical development.," *J. Orthop. Res.*, vol. 8, no. 5, pp. 651–61, Sep. 1990.

[93] G. S. Beaupré, T. E. Orr, and D. R. Carter, "An approach for time-dependent bone modeling and remodeling-application: a preliminary remodeling simulation.," *J. Orthop. Res.*, vol. 8, no. 5, pp. 662–70, Sep. 1990.

[94] C. R. Jacobs, J. C. Simo, G. S. Beaupre, and D. R. Carter, "Adaptive bone remodeling incorporating simultaneous density and anisotropy considerations," *J. Biomech.*, vol. 30, no. 6, pp. 603–613, Jun. 1997.

[95] M. Doblaré and J. M. García, "Anisotropic bone remodelling model based on a continuum damage-repair theory.," *J. Biomech.*, vol. 35, no. 1, pp. 1–17, Jan. 2002.

[96] S. V. Komarova, R. J. Smith, S. J. Dixon, S. M. Sims, and L. M. Wahl, "Mathematical model predicts a critical role for osteoclast autocrine regulation in the control of bone remodeling," *Bone*, vol. 33, no. 2, pp. 206–215, 2003.

[97] J. M. García-Aznar, T. Rueberg, and M. Doblare, "A bone remodelling model coupling microdamage growth and repair by 3D BMU-activity," *Biomech. Model. Mechanobiol.*, vol. 4, no. 2–3, pp. 147–167, 2005.

[98] M. A. Savageau, "Biochemical Systems Analysis. A Study of Function and Design in Molecular Biology," *Addison-Wesley Pub*, Massachusetts, USA, 1976.

[99] A. M. Parfitt, "Osteonal and hemi-osteonal remodeling: the spatial and temporal framework for signal traffic in adult human bone.," *J. Cell. Biochem.*, vol. 55, no. 3, pp. 273–86, Jul. 1994.

[100] R. Hambli, "Connecting mechanics and bone cell activities in the bone remodeling process: an integrated finite element modeling.," *Front. Bioeng. Biotechnol.*, vol. 2, no. April, p. 6, 2014.

[101] K. Yamamoto, T. Sokabe, T. Watabe, K. Miyazono, J. K. Yamashita, S. Obi, N. Ohura, A. Matsushita, A. Kamiya, and J. Ando, "Fluid shear stress induces differentiation of Flk-1-positive embryonic stem cells into vascular endothelial cells in vitro," *Am J Physiol Hear. circ physiol*, vol. 288, pp. 1915–1924, 2004.